

HYDRODYNAMICS, NUCLEOSYNTHESIS, AND MASS LOSS IN MASSIVE
STARS

by
Patrick Allen Young

A Dissertation Submitted to the Faculty of the
DEPARTMENT OF ASTRONOMY
In Partial Fulfillment of the Requirements
For the Degree of
DOCTOR OF PHILOSOPHY
In the Graduate College
THE UNIVERSITY OF ARIZONA

2004

UMI Number: 3132275

INFORMATION TO USERS

The quality of this reproduction is dependent upon the quality of the copy submitted. Broken or indistinct print, colored or poor quality illustrations and photographs, print bleed-through, substandard margins, and improper alignment can adversely affect reproduction.

In the unlikely event that the author did not send a complete manuscript and there are missing pages, these will be noted. Also, if unauthorized copyright material had to be removed, a note will indicate the deletion.

UMI[®]

UMI Microform 3132275

Copyright 2004 by ProQuest Information and Learning Company.

All rights reserved. This microform edition is protected against unauthorized copying under Title 17, United States Code.

ProQuest Information and Learning Company
300 North Zeeb Road
P.O. Box 1346
Ann Arbor, MI 48106-1346

The University of Arizona ®
Graduate College

As members of the Final Examination Committee, we certify that we have read the

dissertation prepared by Patrick Allen Young

entitled Hydrodynamics, Nucleosynthesis, and Mass Loss in Massive

Stars

and recommend that it be accepted as fulfilling the dissertation requirement for the

Degree of Doctor of Philosophy

David Arnett
David Arnett

6-1-04
date

James W. Liebert
James W. Liebert

6-1-04
date

Philip Pinto
Philip Pinto

6/2/04
date

Edward W. Olszewski
Edward Olszewski

6/2/04
date

Donald W. McCarthy Jr.
Donald W. McCarthy Jr.

6/2/04
date

Final approval and acceptance of this dissertation is contingent upon the candidate's submission of the final copies of the dissertation to the Graduate College.

I hereby certify that I have read this dissertation prepared under my direction and recommend that it be accepted as fulfilling the dissertation requirement.

David Arnett
Dissertation Director: David Arnett

6-1-04
date

STATEMENT BY AUTHOR

This dissertation has been submitted in partial fulfillment of requirements for an advanced degree at The University of Arizona and is deposited in the University Library to be made available to borrowers under rules of the Library.

Brief quotations from this dissertation are allowable without special permission, provided that accurate acknowledgment of source is made. Requests for permission for extended quotation from or reproduction of this manuscript in whole or in part may be granted by the head of the major department or the Dean of the Graduate College when in his or her judgment the proposed use of the material is in the interests of scholarship. In all other instances, however, permission must be obtained from the author.

SIGNED: 

ACKNOWLEDGMENTS

It seems unfair that such an essentially collaborative affair as a thesis has only one name on the cover. Many people have contributed to this thesis and all the work that surrounds and supports it. Jaime Highberger, Lucy Ziurys, Karen Knierman, and Jane Rigby have all contributed to the science presented here. Chris Fryer, Grant Bazan, Dave Dearborn, Kris Eriksen, and Dave Porter, among many others, have provided valuable insights. I am especially indebted to Eric Mamajek, Jim Liebert, and Phil Pinto for their advice and expertise in numerous areas.

There is one person without whom I never would have completed this project. Dave Arnett has time and again gone above and beyond the call of duty as an advisor. I cannot overstate my respect for Dave as a scientist. He has taught me a tremendous amount about astrophysics. Dave also has my utmost respect as a person. He has not limited his advice to astronomy, and has given me unstinting support and understanding during some very difficult times. I will always be honored to count Dave as a colleague and a friend.

Grad school is of course a much wider world than any thesis can convey, and so there are many people I would like to recognize who were not a part of the science presented here. First I would like to thank Don McCarthy for giving me the opportunity to share the wonders in astronomy with a wider audience. Don has also been an invaluable source of advice on things both astronomical and not. He has generously allowed me to participate in his educational and scientific activities.

Graduate school has been one of the richest and most fulfilling times in my life. External circumstances have also made it one of the most difficult. I thank my friends for making it such a great experience. In particular, I'd like to thank one of my two best friends here in Tucson. Jackie for listening, for great ideas and bizarre conversations, for many miles of trail, and for giving me a good smack upside the head when necessary (and sometimes when not).

Terry and Margaret, you have been closer to me than family. Thank you for your support during the hardest times, and your friendship all the time. Gregg, Peter, and Jon, you are each in your unique ways among the best friends I will ever have. I always look to your delight in the wonderful things the universe can do when I need to be reminded why I'm here.

There are two very special people I have saved for last. Aerhianna, thank you for always being there, and for showing me the kind of person I really wanted to be. You give me something to believe in. And thank you to Karen for sharing these last two years with me, for believing in me, and for loving me more than I probably deserve.

DEDICATION

Dedicated to all those who were lost during the journey...

Tao

Tsiriath

Tara

Trevor

Cleo

Dallas

Seleya

Ami

Samantha

Oliver

I will see you again.

TABLE OF CONTENTS

LIST OF FIGURES	8
LIST OF TABLES	10
ABSTRACT	11
1 INTRODUCTION	13
2 OBSERVATIONAL TESTS AND PREDICTIVE STELLAR EVOLUTION I: BASE- LINE STELLAR MODELS	20
2.1 Introduction	20
2.1.1 Choice of Binaries	21
2.1.2 The Mixing Length	24
2.1.3 The TYCHO Code	25
2.1.4 Related Investigations	29
2.2 Fitting Models to Binaries	31
2.2.1 Global Aspects of the Errors	34
2.2.2 Massive Binaries	39
2.2.3 Intermediate Mass Binaries	45
2.2.4 Is PV Cas Pre-Main Sequence?	48
2.2.5 Lower Mass Binaries	50
2.2.6 Roche Lobes	52
2.3 Apsidal Motion	55
2.4 Conclusions	61
3 STELLAR HYDRODYNAMICS IN RADIATIVE REGIONS	63
3.1 Introduction	63
3.2 Implications of Numerical Simulations	65
3.2.1 Convective forcing	66
3.2.2 Hydrodynamic response	68
3.2.3 g-modes	70
3.2.4 Dissipation of waves	72
3.2.5 Circulation and mixing	72
3.3 Implementation in stellar evolution	75
3.4 The Stellar Evolution Code TYCHO	76
3.5 Comparisons with Previous Work	78
3.6 Tests of the Theory	80
3.6.1 Li and Be in the Hyades and Pleiades	81
3.6.2 Comparison With Li Depletion Ages	83
3.6.3 Carbon Stars	84

TABLE OF CONTENTS — CONTINUED

3.7	Conclusions	86
4	OBSERVATIONAL TESTS AND PREDICTIVE STELLAR EVOLUTION II: NON-STANDARD MODELS	93
4.1	Introduction	93
4.2	The TYCHO Code	95
4.3	Solar Models	97
4.4	Eclipsing Binaries	103
4.4.1	Global Properties of the Errors	110
4.4.2	Individual Systems of Interest	114
4.5	Conclusions	121
5	A MODEL FOR THE FORMATION OF HIGH DENSITY CLUMPS IN PROTO-PLANETARY NEBULAE	125
5.1	Observational Motivation	125
5.2	Theory of Clumping	126
5.3	Models of Clumping	127
5.3.1	Physical Assumptions	127
5.3.2	Results	130
5.4	Discussion	135
6	CONCLUSION	139

LIST OF FIGURES

2.1	χ^2 for optimum models of selected binaries, versus mean mass of the binary.	32
2.2	Goodness of fit vectors for selected binaries, with observational error bars.	36
2.3	Luminosity differences between best fit models and observations. .	37
2.4	Radius differences between best fit models and observations.	38
2.5	Massive models	40
2.6	Intermediate mass models	46
2.7	Lower mass models	50
2.8	Apsidal constant integrand for EM Car primary.	58
2.9	Classical apsidal motion versus mean mass	60
3.1	Lagrangian (co-moving) fluid surfaces at boundary between convectively stable and unstable regions	69
3.2	Observed Li and Be abundances with model predictions	89
3.3	Observed Pleiades Li abundances with models	90
3.4	Observed luminosity and effective temperature for clusters with brown dwarf Li depletion ages with isochrones	91
3.5	Selected surface abundances for AGB model showing enhancement in C/O	92
4.1	Evolutionary tracks for 1 M_{\odot} stars with four variations on mixing physics	104
4.2	χ^2 values for optimum models of binaries, versus mean mass of the binary	111
4.3	Goodness of fit vectors with error bars	112
4.4	Classical apsidal motion versus mean mass	114
4.5	Evolutionary tracks ($z = 0.013$) and observed points with errors for ζ Phe	116

LIST OF FIGURES — CONTINUED

4.6	Evolutionary tracks ($z = 0.023$) and observed points with errors for AI Hya	117
4.7	Evolutionary tracks ($z = 0.019$) and observed points with errors for EK Cep	119
4.8	Evolutionary tracks ($z = 0.024$) and observed points with errors for TZ For	120
5.1	Density profile for fully developed clumping for the high resolu- tion simulation	132
5.2	Comparison of density profiles at similar shock radii for cases with and without cooling	133
5.3	Carbon mass fraction of the material	135
5.4	The planetary nebula IC 2149, imaged by the ARIES near-infrared imager and adaptive secondary on the 6.5m MMT	137
6.1	Abundance profiles for a $23 M_{\odot}$ star at the beginning of Si burning for models with and without realistic mixing physics	146

LIST OF TABLES

2.1	Observed parameters for selected binary systems. ^a	23
2.1	Observed parameters for selected binary systems. ^a	24
2.2	Parameters for selected binary systems.	33
2.2	Parameters for selected binary systems.	34
2.3	Predicted instantaneous mass loss rates.	43
2.4	Roche lobe parameters for selected binary systems.	54
2.4	Roche lobe parameters for selected binary systems.	55
2.5	Apsidal comparisons for selected binary systems.	59
2.5	Apsidal comparisons for selected binary systems.	60
4.1	Characteristics of Solar Models with Varied Mixing Physics	99
4.2	Neutrino Fluxes for Solar Models with Varied Mixing Physics	100
4.3	Observed parameters for selected binary systems. ^a	105
4.3	Observed parameters for selected binary systems. ^a	106
4.4	Results for selected binary systems.	108
4.4	Results for selected binary systems.	109
4.5	Apsidal comparisons for selected binary systems.	115

ABSTRACT

I test the predictive power of the stellar evolution code TYCHO. Systematic errors are present in the predictions for double-lined eclipsing binary stars when only standard physics common to the majority of stellar evolution codes is included. A mechanism for driving slow circulation and mixing in the radiative regions of stars is identified in numerical simulations of convection and a physical theory developed. Mixing is caused by dissipation of inertial waves driven by the interaction of convective fluid motions with the boundary of the convection zone. Evolutionary calculations incorporating this physics are tested in several observational regimes. Light element depletion in young clusters, turnoff ages of young clusters with brown dwarf Li depletion ages, and evolution of carbon stars on the asymptotic giant branch are all predicted satisfactorily. Tests of solar models yield good agreement with surface observables, chemical abundances, helioseismological data, and neutrino fluxes. The predictive accuracy of a non-calibrated, state-of-the-art stellar evolution code is $\sim 7\%$ for surface observables. The main sequence sun is relatively easy to model, so this gives an estimate of our minimum predictive error. The solar models also highlight problems with uniqueness of evolutionary tracks converging on a given point and the potential for avoiding the effects of missing physics by calibration. A reanalysis of the binary sample with the more complete physics shows a dramatic improvement in the accuracy of the models. The potential for avoiding the effects of missing physics by calibration is explored. A TYCHO model for a late AGB star is used for the boundary conditions on a hydrodynamic simulation of proto-planetary nebula evolution as an illustration of the unified technique. NaCl and NaCn are observed at large radii in the Egg Nebula. These molecules require high densities

to form, which are difficult to explain at large distances from the star. The 2-D simulation of a fast wind interacting with earlier mass loss produces clumps of material through a thermal instability with the necessary conditions for formation of the molecules. In conclusion, the effects of the more complete physics on the core size and abundance profiles of a massive star during core Si burning are examined as an example of future developments.

CHAPTER 1

INTRODUCTION

Ultimately it may be that the consistency of the findings in different branches of astrophysics will form a basis for a more general verification of physical laws than can be attained in the laboratory; but at present, terrestrial physics must be the groundwork of the study of stellar conditions.

Cecilia H. Payne (1925)

Stellar evolution has become a successful tool for elucidating the processes at work in individual stars. New instrumentation and a wealth of new data has resulted in increased emphasis in astronomy on the evolution of galaxies over cosmic history. Obviously the stellar content of a galaxy plays a central role in its evolution. In order to understand this process, we require theoretical stellar evolution to be predictive, in the sense of being able to accurately describe the contribution of luminosity, kinetic energy, and nucleosynthetic products from a star of a specific initial mass and composition at any and all points in its life.

To illustrate this point, consider the Sun. It is an observationally over-constrained system, so that unknowns and free parameters can be fixed precisely. Its helioseismological structure, neutrino production, luminosity, radius, and effective temperature can be fit to much better than 1% (Basu, Pinsonneault, & Bahcall, 2000). However, given only its initial mass and composition, we could *predict* its gross observables to an accuracy of perhaps 7%. For the sun, this uncertainty arises from (1) inadequacy in our description of convection, manifested by an uncertainty in the fictitious mixing length parameter, and (2) by uncertainties in

abundances. A solar mass star on the main sequence is probably the easiest type of star to model. It is largely unaffected by mass loss, mixing, and convection, which dominate the evolution of massive stars and the later stages of low and intermediate mass stars. Our predictions of these stars can vary by tens of percent, possibly as much as factors of two for the most massive stars. For the stars in OB associations this translates to errors in ages on the order of 50%. In the case of unstable massive stars like Luminous Blue Variables (LBVs) and Wolf-Rayets, our mass estimates can be off by as much as a factor of two. No models match starburst populations younger than a few million years to any reasonable level of accuracy (Rigby & Rieke, 2004). This can have a profound effect on calculations of nucleosynthetic or kinetic energy contributions from a population. If the mass of a star which contributes a particular abundance pattern is overestimated by 10%, then the total number of stars contributing that abundance pattern is underestimated by $\sim 25\%$ for a simple Salpeter initial mass function (IMF). In practice, we do not know the mass limits for different types of supernovae (SNII vs SNIb/c and various subgroups therein). Mass estimates of the progenitor of Cassiopeia A, one of the three best studied (and presumably understood) supernovae in the sky, range from $\sim 25M_{\odot}$ to $> 80M_{\odot}$.

The predictive evolution process must be able to be carried out self consistently for stars from the hydrogen burning limit to the highest possible masses, so that stellar outcomes can be reliably linked to an initial mass function (IMF). This is not possible with schemes which are adjusted to match astronomical observations. For example, young cluster ages can be fit well by assuming convective “overshooting” which mixes material an arbitrary fraction of a pressure scale height outside the convective core. This fraction is different, however, when fitting low mass and high mass stars. Without an underlying physical theory, the

calibration cannot be reliably extrapolated to regimes without extensive observational data. Also, multiple physical effects can contribute in opposite or orthogonal senses to the star's structure. As an example, determinations of metallicity of binaries are often made by fitting model tracks of varying composition to observed points and finding the best fit. However, an underestimate of the mixing tends to drive the models in the same direction as increased metallicity. So a model with incomplete mixing physics and solar composition could be as good a formal fit to the observations as a model with complete physics and supersolar metallicity.

The two primary areas which strongly affect the evolution and have uncertain physics are mixing and mass loss. The evolution is also sensitive to the opacity of the stellar material, but the opacities used in evolution codes are largely uniform, utilizing the OPAL values of Iglesias & Rogers (1996) for high temperatures and Alexander & Ferguson (1994) for low temperatures. The OPAL opacities are extensively tested in plasmas under astrophysical conditions by high energy density (HED) laser experiments, and are very reliable. The low temperature opacities are more likely to be incomplete at very low temperatures and high densities, where large numbers of molecular species, dust, and strong Coulomb effects are important. This primarily concerns very low mass stars, $< 0.5M_{\odot}$. The observational errors in determining stellar compositions are the major limitation on further testing contribution of opacities to stellar models. Even the metallicity of the sun varies from $z=0.019$ (Grevesse & Sauval, 1998) to $z=0.015$ (Lodders, 2003), depending upon the precise physical assumptions and dimensionality of the codes being used to fit the measured line profiles. Abundant elements which contribute strongly to stellar opacities, including O, C, and Fe are significantly affected. Most other test cases, such as most double-lined eclipsing binaries, have

no published metallicity determinations. Equations of state (EOS's) are not uniform across stellar evolution codes. While the effects of the EOS are perhaps more subtle, they can still be important, particularly for low mass stars and pre- and post-main sequence evolution.

Stellar lifetimes are very long compared to constraints on a numerical timestep, particularly for explicit hydro codes limited by the Courant condition on sound crossing times of computational zones. Further, the computer time required for the 3-D simulation scales as roughly the cube of that required for a similar 1-D calculation. This renders more realistic calculations of a full stellar lifetime intractable with any current or proposed computing facilities. For instance, simulations of full stars in 3-D by the Djehuty group at Lawrence Livermore National Laboratory run somewhat more slowly than the actual star would evolve. We are forced to resort to 1-D, spherically symmetric, implicit codes which necessarily include certain physical simplifications. Such codes treat the life of a star as a series of static states. Inherently dynamic processes cannot be calculated. These limitations can to some extent be overcome by using an approach which integrates a number of techniques. Numerical models and computing power have advanced to the point where stars can be examined in 3-D during brief snapshots of their lives, giving us a better understanding of the interior physics during long stages and allowing us to calculate directly rapid dynamic phases. The physical conditions of stellar plasmas can be directly probed by high energy density laboratory astrophysics experiments. Physical theories developed from the phenomenology observed in laboratory and numerical experiments can serve as a basis for making stellar evolution codes physically complete. Validation of the predictive accuracy of the code by a wide range of astronomical observations serves to test the newly identified physics and its implementation. This work

describes the development of this approach and its application to the stellar evolution and hydrodynamics code TYCHO.

In the first chapter, I present results from stellar models calculated using only physics common to current widely used stellar evolution codes. This provides us with baseline results which we can use to discuss prediction versus optimization by observational calibration as a strategy for pursuing stellar evolution. These models were tested against a subset of the Andersen (1991) double-lined eclipsing binaries. This set of observational tests reveals systematic inadequacies in the standard description of stellar evolution and identifies particular aspects of the physics which are deficient.

The second chapter (Young et al., 2003) discusses hydrodynamic mixing within the radiative regions of stars and presents several observational tests of the mechanism. Multi-D models of stellar convection exist for core (i.e. Meakin, 2004), envelope (i.e. Brummell, Clune, & Toomre, 2002), and burning shell convection (i.e. Asida & Arnett, 2000). All of these show common behavior at the boundary between convective and radiative regions. The impact of convective plumes upon this boundary drives inertial waves which, in dissipating, create vorticity and drive slow compositional mixing. Implementing this theory in TYCHO gives good results for light element depletion in young clusters, cluster ages compared to brown dwarf Li depletion ages, and production of carbon stars on the asymptotic giant branch (AGB). All of these results are achieved without observational calibration.

The third chapter presents a reanalysis of the eclipsing binary sample of Chapter 2 and solar models with more realistic mixing physics, as well as additional minor improvements to the code. A summary of the current state of the code is given. The radius, effective temperature, luminosity, convective zone size, sound

speeds, and neutrino fluxes are compared to standard solar models and found to be in good agreement. The predictive accuracy of a state-of-the-art stellar evolution code using only the observational constraints which would be available for a star other than the sun are estimated to be $\sim 7\%$. The reanalysis of the eclipsing binary sample shows considerable improvement with the more complete physics. Systematic errors in convective core sizes disappear with the improved mixing treatment. The lack of abundance determinations for many of the binary systems is now the primary limitation on our accuracy, as the code cannot be tested more stringently without this data. Systematic inadequacies in pre-main sequence (pre-MS) models and clues from numerical simulations indicate the presence of additional physics in stars with low surface gravities.

The fourth chapter gives an example of the integrated stellar evolution plus hydrodynamics approach. Radio observations of the Egg Nebula indicate the formation of NaCl at large radii from the star. Conventional 1-D shock models cannot produce the necessary densities for the formation of this molecule (Highberger et al., 2003). A mass loss history and stellar observables calculated using TYCHO are used as inner boundary conditions for a 2-D hydro simulation with PROMETHEUS. A fast wind expanding into slower-moving AGB ejecta drives a thermal instability which results in clumping of material at the wind interface. These clumps have the necessary physical conditions for the formation of NaCl and occur at appropriate timescales and radii from the star.

To conclude, I discuss the implications of this approach for other astrophysical problems. In particular, I examine the abundance profiles of a $20 M_{\odot}$ star during core silicon burning with and without the realistic mixing physics. Stars of $10\text{--}20 M_{\odot}$ are the progenitors of most of the supernovae in the current universe. The final core size and abundance profile of the star is sensitive to this mixing.

This sensitivity has far-reaching ramifications, ranging from the physics of the supernova explosion to the chemical evolution of galaxies.

CHAPTER 2

OBSERVATIONAL TESTS AND PREDICTIVE STELLAR EVOLUTION I: BASELINE STELLAR MODELS

2.1 Introduction

Prior to any rigorous investigation of thermonuclear yields, mixing, rotation, mass loss, and other complex phenomena in the evolution of stars, it is necessary to ensure that the methodology used can reproduce observations at the current state of the art. Detached, double-lined eclipsing binaries provide the most accurate source of information on stellar masses and radii, and as such provide a crucial test for models of stellar evolution (Andersen, 1991).

The predictive power of such simulations depends upon the extent to which the validity of their oversimplifications can be tested. Phenomenology is particularly pernicious in that good tests, which could give rise to falsification of the models and thus to progress, can be nullified by parameter adjustment (“calibration”). Similarly, the inclusion of new processes in the simulations is often contentious in that there may be several candidates put forward as the cause of the puzzling data. The treatment of the boundaries of convection zones (“overshooting”) is ripe for re-examination in terms of the underlying hydrodynamics (Asida & Arnett, 2000). To aid this development, we wish to understand just how well a standard convective treatment can do (i.e., we turn overshooting off). A more physically sound procedure will be presented subsequently. Parameterized overshooting has been widely discussed (see Maeder (1975) for an early discussion, and Schröder et al. (1997) and Schaller et al. (1992); Bressan et al. (1993);

Dominguez et al. (1999) for a recent ones with extensive references). Rotation also may cause mixing (Meynet & Maeder, 2000). Within the context of a plasma, rotation and convection may generate magnetic fields, which by their buoyancy and angular momentum transport may provide additional causes for mixing.

This paper represents a first step toward testing our extensively revised stellar evolution and hydrodynamics code, TYCHO. Our goals are (1) understanding the predictive capability of stellar evolution theory by the critical re-evaluation of its assumptions, and of its underlying basis in observations and in laboratory data, (2) the examination of the tricky problem of mixing in stars to help design experiments (Remington et al., 1999) and numerical tests (Asida & Arnett, 2000), and (3) the development of an open source, publicly available stellar evolution code with modern capabilities for community use.

2.1.1 Choice of Binaries

The most comprehensive list of binary systems with accurately measured masses and radii is given in the review by Andersen (1991). A subset of the original binaries was chosen for this exploratory effort. The systems with the smallest uncertainties were picked such that the range of masses from 23 to $1.1 M_{\odot}$ was well sampled. The upper mass limit is the largest mass present in the data, while the lower limit is safely above the point at which the equation of state used in the modeling becomes inaccurate. This is primarily due to approximate treatment of Coulomb contributions to the pressure; we use only the weak screening limit for the plasma. The Coulomb interaction leads to a negative pressure correction of $\sim 8\%$ in the outer part of the convection region and $\sim 1\%$ in the core for a star of $1 M_{\odot}$ (Däppen & Nayfonov, 2000), and is less important for more massive stars. We obtain a comparable correction to the central pressure for a solar model (-1.7%).

Aside from the exclusion of stars of still lower mass, no bias was applied in the

selection process. For stars of $1 M_{\odot}$ or less, the issue of possible overshooting in the convective core is moot because their cores are radiative. Also, because they rotate rapidly only for a brief part of their lives, rotational mixing is expected to be less than for our selected stars. The binaries used in the study along with their fundamental parameters are presented in Table 2.1. Ribas et al. (2000) have revised the Andersen (1991) temperature estimates, and revised estimates for the masses of EM Car (Stickland, Lloyd, & Corcoran, 1994) and CW Cep (Stickland, Koch & Pfeiffer, 1992) have been presented. Latham et al. (1996) have revised the parameters for DM Vir. All these changes are incorporated into Table 2.1.

Table 2.1. Observed parameters for selected binary systems.^a

System	P(d)	Star	Spect.	Mass/ M_{\odot}	Radius/ R_{\odot}	$\log g(\text{cm/s}^2)$	$\log T_e(\text{K})$	$\log L/L_{\odot}$
EM Car	3.41	A	O8V	22.3 ± 0.3^b	9.34 ± 0.17	3.864 ± 0.017^b	4.531 ± 0.026	5.02 ± 0.10
HD97484	...	B	O8V	20.3 ± 0.3^b	8.33 ± 0.14	3.905 ± 0.016^b	4.531 ± 0.026	4.92 ± 0.10
V478 Cyg	2.88	A	O9.5V	16.67 ± 0.45	7.423 ± 0.079	3.919 ± 0.015	4.484 ± 0.015	4.63 ± 0.06
HD193611	...	B	O9.5V	16.31 ± 0.35	7.423 ± 0.079	3.909 ± 0.013	4.485 ± 0.015	4.63 ± 0.06
CW Cep	2.73	A	B0.5V	12.9 ± 0.1^c	5.685 ± 0.130	4.039 ± 0.024^c	4.449 ± 0.011^d	4.26 ± 0.06^c
HD218066	...	B	B0.5V	11.9 ± 0.1^c	5.177 ± 0.129	4.086 ± 0.024^c	4.439 ± 0.011^d	4.14 ± 0.07^c
QX Car	4.48	A	B2V	9.267 ± 0.122	4.289 ± 0.091	4.140 ± 0.020	4.395 ± 0.009^d	3.80 ± 0.04^c
HD86118	...	B	B2V	8.480 ± 0.122	4.051 ± 0.091	4.151 ± 0.021	4.376 ± 0.010^d	3.67 ± 0.04^c
CV Vel	6.89	A	B2.5V	6.100 ± 0.044	4.087 ± 0.036	4.000 ± 0.008	4.254 ± 0.012^d	3.19 ± 0.05
HD77464	...	B	B2.5V	5.996 ± 0.035	3.948 ± 0.036	4.023 ± 0.008	4.251 ± 0.012^d	3.15 ± 0.05
U Oph	1.68	A	B5V	5.198 ± 0.113	3.438 ± 0.044	4.081 ± 0.015	4.211 ± 0.015^d	2.87 ± 0.08^c
HD156247	...	B	B6V	4.683 ± 0.090	3.005 ± 0.055	4.153 ± 0.018	4.188 ± 0.015^d	2.66 ± 0.08^c
ζ Phe	1.67	A	B6V	3.930 ± 0.045	2.851 ± 0.015	4.122 ± 0.009	4.149 ± 0.010^d	2.46 ± 0.04^c
HD6882	...	B	B8V	2.551 ± 0.026	1.853 ± 0.023	4.309 ± 0.012	4.072 ± 0.007^d	1.78 ± 0.04^c
IQ Per	1.74	A	B8V	3.521 ± 0.067	2.446 ± 0.026	4.208 ± 0.019	4.111 ± 0.008^d	2.17 ± 0.03^c
HD24909	...	B	A6V	1.737 ± 0.031	1.503 ± 0.017	4.323 ± 0.013	3.906 ± 0.008^d	0.93 ± 0.04^c
PV Cas	1.75	A	B9.5V	2.815 ± 0.050^d	2.297 ± 0.035^d	4.165 ± 0.016^d	4.032 ± 0.010^d	1.80 ± 0.04^c
HD240208	...	B	B9.5V	2.756 ± 0.054^d	2.257 ± 0.035^d	4.171 ± 0.016^d	4.027 ± 0.010^d	1.77 ± 0.04^c
AI Hya	8.29	A	F2m	2.145 ± 0.038	3.914 ± 0.031	3.584 ± 0.011	3.851 ± 0.009^d	1.54 ± 0.02^c
+0° 2259	...	B	F0V	1.978 ± 0.036	2.766 ± 0.017	3.850 ± 0.010	3.869 ± 0.009^d	1.31 ± 0.02^c
VV Pyx	4.60	A	A1V	2.101 ± 0.022	2.167 ± 0.020	4.089 ± 0.009	3.979 ± 0.009^d	1.54 ± 0.04
HD71581	...	B	A1V	2.099 ± 0.019	2.167 ± 0.020	4.088 ± 0.009	3.979 ± 0.009^d	1.54 ± 0.04
RS Cha	1.67	A	A8V	1.858 ± 0.016	2.137 ± 0.055	4.047 ± 0.023	3.883 ± 0.010^d	1.14 ± 0.05^c
HD75747	...	B	A8V	1.821 ± 0.018	2.338 ± 0.055	3.961 ± 0.021	3.859 ± 0.010^d	1.13 ± 0.05^c
EK Cep	4.43	A	A1.5V	2.029 ± 0.023	1.579 ± 0.007	4.349 ± 0.010	3.954 ± 0.010	1.17 ± 0.04
HD206821	...	B	G5Vp	1.124 ± 0.012	1.320 ± 0.015	4.25 ± 0.010	3.756 ± 0.015	0.19 ± 0.07
MY Cyg	4.01	A	F0m	1.811 ± 0.030	2.193 ± 0.050	4.007 ± 0.021	3.850 ± 0.010^d	1.03 ± 0.04^c
HD193637	...	B	F0m	1.786 ± 0.025	2.193 ± 0.050	4.014 ± 0.021	3.846 ± 0.010^d	1.02 ± 0.04^c

Table 2.1—Continued

System	P(d)	Star	Spect.	Mass/ M_{\odot}	Radius/ R_{\odot}	$\log g(\text{cm/s}^2)$	$\log T_e(\text{K})$	$\log L/L_{\odot}$
PV Pup	1.66	A	A8V	1.565 ± 0.011	1.542 ± 0.018	4.257 ± 0.010	3.840 ± 0.019	0.69 ± 0.08
HD62863	...	B	A8V	1.554 ± 0.013	1.499 ± 0.018	4.278 ± 0.011	3.841 ± 0.019	0.67 ± 0.08
DM Vir ^f	4.67	A	F7V	1.454 ± 0.008	1.763 ± 0.017	4.108 ± 0.009	3.813 ± 0.007	0.70 ± 0.03
HD123423 ^f	...	B	F7V	1.448 ± 0.008	1.763 ± 0.017	4.106 ± 0.009	3.813 ± 0.020	0.70 ± 0.03
V1143 Cyg	7.64	A	F5V	1.391 ± 0.016	1.346 ± 0.023	4.323 ± 0.016	$3.820 \pm 0.007^{\text{d}}$	$0.49 \pm 0.03^{\text{c}}$
HD185912	...	B	F5V	1.347 ± 0.013	1.323 ± 0.023	4.324 ± 0.016	$3.816 \pm 0.007^{\text{d}}$	$0.46 \pm 0.03^{\text{c}}$
UX Men	4.18	A	F8V	1.238 ± 0.006	1.347 ± 0.013	4.272 ± 0.009	$3.785 \pm 0.007^{\text{d}}$	$0.35 \pm 0.03^{\text{c}}$
HD37513	...	B	F8V	1.198 ± 0.007	1.274 ± 0.013	4.306 ± 0.009	$3.781 \pm 0.007^{\text{d}}$	$0.29 \pm 0.03^{\text{c}}$

^aDetailed references and discussion may be found in (Andersen, 1991).

^bStickland, Lloyd, & Corcoran (1994).

^cStickland, Koch & Pfeiffer (1992).

^dRibas et al. (2000).

^eAdjusted here.

^fLatham et al. (1996).

2.1.2 The Mixing Length

If the purpose of a stellar evolution code is to make testable predictions of the behavior of stars, then the adjustment of the mixing length by fitting stellar data is repugnant. Alternatives are to constrain it by experiment or by simulation. At present we know of no definitive experimental results which determine the mixing length appropriate to stars, although a variety of experiments do test other aspects of stellar hydrodynamics and the codes used to simulate them (Remington et al., 1999). However, it is becoming possible to simulate turbulent, compressible convection with sufficient realism to constrain the range allowed for the mixing

length (Rosenthal et al., 1999; Porter & Woodward, 1994, 2000; Elliott, Miesch, & Toomre, 2000; Asida, 1998). Porter & Woodward (2000) find a mixing length $\alpha_{ML} = 2.68$ in units of pressure scale height; this is based upon simulations having mesh resolutions as high as $512 \times 512 \times 256$ and corresponding Rayleigh numbers as high as 3.3×10^{12} . Rosenthal et al. (1999) based their work on resolutions up to $253 \times 253 \times 163$, but with a more realistic treatment of radiative transfer and ionization. They were able to synthesize the line profile of FeII $\lambda 5414$ which compared well with that observed. Their results agreed with standard 1-D models, although they suggest that this might be “the right result for the wrong reason.” Standard models use $\alpha_{ML} = 1.5$ to 2, which is significantly smaller than the value of Porter & Woodward (2000). For a red giant, Asida (1998) inferred $\alpha_{ML} = 1.6$, based upon 2-D simulations but with fairly realistic microphysics.

Canuto & Mazzitelli (1991, 1992) have proposed a serious model to replace mixing length theory; this has had the salutary effect of shifting the debate to the physics of convection and away from the best choice of mixing length. Finally, Asida & Arnett (2000) have shown from 2-D simulations that the underlying physical picture for stellar convection is incomplete, even in the deep interior where the complication of radiative transfer is minor.

We simply choose $\alpha_{ML} = 1.6$, and look forward to the convergence of these efforts to provide a convection algorithm which is independent of stellar evolutionary calibrations.

2.1.3 The TYCHO Code

The evolutionary sequences were produced with the TYCHO stellar evolution code. The code was originally developed for one dimensional (1D) hydrodynamics of the late stages of stellar evolution and core collapse (Arnett, 1996). It is being completely rewritten as a general purpose, open source code for stellar evolution

and hydrodynamics. The present version is written in structured FORTRAN77 and is targeted for Linux machines. It has been successfully ported to SunOS and SGI IRIX operating systems. It has extensive online graphics using PGPLOT, an open source package written by T. J. Pearson (tip@astro.caltech.edu). A library of analysis programs is being built (modules for apsidal motion, pulsational instability, reaction network links, and history of mass loss are now available). The code is being put under source code control to allow versioning (this will allow particular versions of the code—for example the one used in this paper, to be resurrected accurately at later times), and to improve the reproducibility of results.

Knowledge of the radiative opacity of plasma at stellar conditions has changed qualitatively in the past decade. Historically, solar and stellar atmospheres provided much of the empirical data on hot plasmas. For example, Kurucz (1991) tabulates a range of effective temperatures from 2,000 to 200,000 K. These temperatures and the corresponding (low) densities characterized what was directly observable. Higher temperatures could be found at lower densities (in non-LTE) or indirectly inferred by use of theoretical models. Terrestrial tests involved explosions which were difficult to quantify with adequate precision to determine opacity. Measurements of opacity in a well characterized, hot, dense, laser-produced plasma have become possible (Perry et al., 1991; Springer et al., 1992; Mostovych et al., 1995; Davidson et al., 2000). The first experiments to simultaneously quantify temperature and density with good precision (Perry et al., 1991; Springer et al., 1992) involved temperatures $T \approx 7 \times 10^5$ K and densities $\rho \approx 2 \times 10^{-2}$ g cm⁻³, which are directly relevant to stellar evolution and to apsidal motion. The range of conditions which are experimentally accessible is expanding with the development of new instruments and techniques. Not only can direct measurements be made, but complex and sophisticated theories of the physical state of the plasma

can be tested, giving more reliable extrapolations into conditions not yet experimentally accessible (Perry et al., 1996; Davidson et al., 2000). The conditions just quoted are encountered in stars of about $1M_{\odot}$, and are important for stellar evolution (see Ch. 7, Arnett (1996)).

The opacities used here are from Iglesias & Rogers (1996) and Kurucz (1991), for a solar abundance pattern (Anders & Grevesse, 1989). The Iglesias & Rogers (1996) opacities were computed with 21 elemental species; Iglesias et al. (1995) have shown that the remaining elements are so rare as to have only a marginal effect on the Rosseland mean opacities (for solar relative abundances of the heavier elements). While the OPAL opacities were constructed for astrophysical use, the underlying experiments and theoretical models are determined by the inertial confinement fusion (ICF) community, reducing the danger of unconscious bias from astronomical puzzles leaking back into the construction of opacities. Extension of the opacity library to lower temperatures and lower entropies is planned.

TYCHO is designed to use an adaptable set of reaction networks; for these calculations, two networks were used. At higher temperatures ($T \geq 10^7$ K), an 80 element reaction network was solved. The reaction rates were from F. K. Thielemann (private communication); see also (Thielemann, Arnould, & Truran, 1988). For lower temperatures this was replaced by a 15 element network which was designed for deuterium, lithium, beryllium, and boron depletion. The reaction rates were from Caughlan & Fowler (1988). The match at the temperature boundary was sufficiently good as to require no smoothing. More recent compilations of nuclear rates are available (Rauscher & Thielemann, 2000; Angulo et al., 1999), but were not used here to simplify the comparison with previous work.

The outer boundary condition was determined by use of the Eddington ap-

proximation to a grey, plane parallel atmosphere, integrated in hydrostatic equilibrium inward to a fitting point for the interior. For the most extended model considered here, the ratio of mean free path to radius was $\lambda/R \sim 5 \times 10^{-3}$, so that spherical effects are negligible. The most vigorous mass loss considered was so mild that the ram pressure ρv_{loss}^2 at the photosphere was 10^{-6} of the total thermal pressure, which is consistent with the hydrostatic assumption. Such integrations were used to define the pressure and temperature at the fitting points, $T_f(L, R)$ and $P_f(L, R)$, for the stellar luminosity L and radius R . Their derivatives with respect to stellar luminosity and radius were approximated by finite differences constructed between three such integrations (at L, R , $L + \delta L, R$, and $L, R + \delta R$). Typically, of order 200 to 400 steps were used in the envelope integration.

We used Schwarzschild convection as formulated by Kippenhahn & Weigert (1990), and our treatment of convective overshooting was turned off.

Mass loss was included and based on the theory of Kudritzki et al. (1989) for $T_{eff} \geq 7.5 \times 10^3$ K and the empirical approach of de Jager, Nieuwenhuijzen, & van der Hucht (1988) for lower effective temperatures. R. Kudritzki kindly provided appropriate subroutines for the hotter regime. Even for EM Car, the most massive system in the list, the effects of mass loss were modest (0.6 to 0.7 M_\odot).

The equation of state was that discussed in Timmes & Arnett (1999), augmented by the solution of the ionization equilibrium equations for H, He, and a set of heavier elements scaled from the solar abundance pattern. Both the equation of state and the thermonuclear reaction rates are affected by coulomb properties of the plasma. Only weak screening was necessary here. Extension to include both weak and strong screening consistently in the equation of state and thermonuclear reaction rates is planned; previous versions of the code included strong screening as well.

Models were run for each mass, starting with a fully convective initial model on the Hayashi track and ending well beyond hydrogen depletion in the core. A more realistic approach would have been to form the stars by accretion (A. G. W. Cameron, private communication; Norberg & Maeder (2000)). We justify our choice by its simplicity, and by noting that only the last stages of the pre-main sequence are relevant here, for which the two cases give similar results.

Zoning in the interior typically ranged from 200 to 500 zones. All runs had solar heavy element abundance (Anders & Grevesse, 1989) and used a ratio of mixing length to scale height of $\alpha = 1.6$ for convection. This choice gave a reasonably good solar model when compared to Bahcall & Pinsonneault (1998) and Christensen-Dalsgaard (2000); inclusion of element settling by diffusion and adjustment of the helium abundance would give improved consistency for the present-day sun, but diffusion would have less time to operate in the more massive stars considered here. Rotational mixing was turned off.

2.1.4 Related Investigations

The stars are all at or near the main sequence, so that the possible list of citations is enormous; the efforts of the Padua group (Bressan et al., 1993), the Geneva group (Schaller et al., 1992), and the FRANEC group (Dominguez et al., 1999) have comparable input physics and form a useful context. We focus discussion on Pols et al. (1997b) and Ribas et al. (2000), who consider many of the same binaries, and Claret & Giménez (1993) who examined the apsidal motion test.

The largest differences in microphysics between Pols et al. (1997b) and this paper are our use of Iglesias & Rogers (1996) rather than Rogers & Iglesias (1992) opacities, a more realistic nuclear network, and a different approach to the equation of state, but none of this seems to be particularly significant for the issues here. We do include mass loss, but these effects are not large. Pols et al. (1997b)

do not calculate the pre-main sequence evolution (which is relevant to several of our binaries). They define an overshooting parameter which is fixed by previous work on ζ Aurigae binaries (Schröder et al., 1997). They construct a grid of models in mass (0.5 to 40 M_{\odot}) and heavy element abundance ($Z = 0.01, 0.02$ and 0.03), assuming $X = 0.76 - 3.0Z$ and $Y = 0.24 + 2.0Z$ for the abundances of hydrogen and helium. They minimize a χ^2 error estimator in four parameters: the masses M_A and M_B , the age t of the binary, and Z , the heavy element abundance.

As a test of consistency for later evolution, we have reproduced the 4 and 8 M_{\odot} sequences of Pols et al. (1997a), which did not use overshooting. The notoriously sensitive blue loops were reproduced to graphical accuracy (their Figure 4) for the same input physics. The codes seem highly consistent.

Ribas et al. (2000) used the models of Claret (1995, 1997b) and Claret & Giménez (1995, 1998), which use Rogers & Iglesias (1992) opacities and a 14 isotope network and include overshooting and mass loss. They too interpolated in a grid, minimizing a χ^2 error estimator. This procedure was more complex than that used by Pols et al. (1997b), and need not be described here. Both heavy element abundance and helium abundance were freely varied.

Our strategy differs from both Pols et al. (1997b) and Ribas et al. (2000), which may provide a useful contrast. Here we are interested in isolating the possible inadequacy of the standard formulation of stellar evolution, so we avoid optimization of parameters as much as possible. By using (1) solar abundances and (2) the measured masses, we reduce the degrees of freedom, and hopefully make the possible flaws in our stellar evolution prescriptions easier to see. By the same token, our models should fit the data less well because we have not optimized abundances or masses. Mathematically, optimization will almost always improve the fit, but not necessarily for the correct reasons. However, the

actual abundances may be different from our assumptions, and the masses do have error bars.

Claret & Giménez (1993) used Rogers & Iglesias (1992) opacities, solar abundances, a mixing length ratio $\alpha_{ML} = 1.5$, and overshooting of $\alpha_{OV} = 0.2$ pressure scale heights (that is, essentially the same physics as the models used by Ribas et al. (2000)), and computed structure constants for apsidal motion for seven of the binaries we consider (EM Car, CW Cep, QX Car, U Oph, ζ Phe, IQ Per, and PV Cas).

Detailed comparisons will appear in the discussion below.

2.2 Fitting Models to Binaries

The first step in comparing the binary data with the computations is the choice of the best models. This was done by examining a χ^2 quantity for each binary pair, defined by

$$\begin{aligned}\chi^2 &= ((\log L(m_A, t) - \log L_A)/\sigma_{LA})^2 \\ &+ ((\log L(m_B, t) - \log L_B)/\sigma_{LB})^2 \\ &+ ((\log R(m_A, t) - \log R_A)/\sigma_{RA})^2 \\ &+ ((\log R(m_B, t) - \log R_B)/\sigma_{RB})^2,\end{aligned}\tag{2.1}$$

where A and B denote the primary and the secondary star, respectively. Here L_A and R_A are the observationally determined luminosity and radius of the primary, with σ_{LA} and σ_{RA} being the observational errors in $\log L_A$ and in $\log R_A$. We convert the observational data for the radii to logarithmic form for consistency. Correspondingly, $L(m_A, t)$ and $R(m_A, t)$ are the luminosity and radius of the model. This χ^2 was evaluated by computing two evolutionary sequences, one for a star of mass m_A and one for m_B , and storing selected results from each time

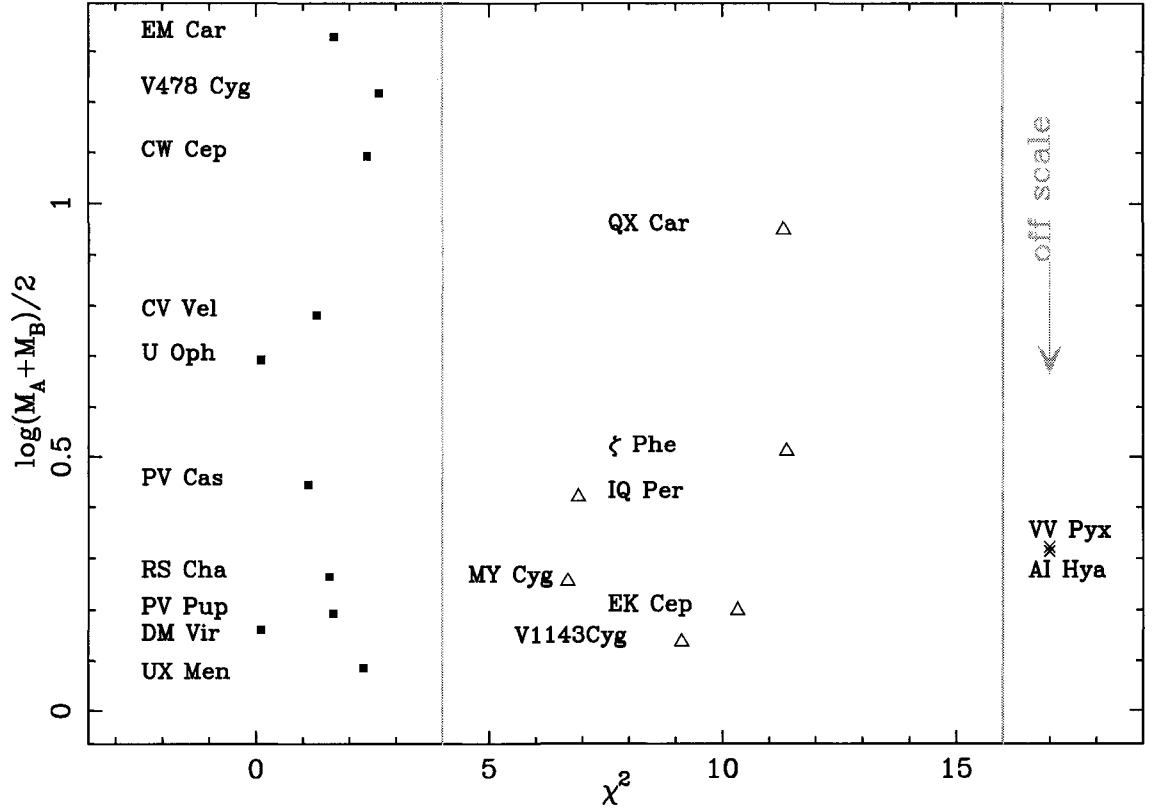


Figure 2.1: χ^2 for optimum models of selected binaries, versus mean mass of the binary.

step. Then these files were marched through, calculating χ^2 at consistent times ($t_A = t_B$ to a fraction of a time step, which was a relative error of a few percent at worst). The smallest χ^2 value determined which pair of models was optimum for that binary. Note that if the trajectories of both A and B graze the error boxes at the same time, $\chi^2 \approx 4$. These error parameters along with the corresponding uncertainties from the observations are presented in Table 2.2.

Table 2.2. Parameters for selected binary systems.

System	Star	Mass	$\log R/R_{\odot}$	$\log T_e$	$\log L$	$\log \text{Age (yr)}$	χ^2
EM Car	A	22.89	0.972	4.509	4.933	6.666	1.67
HD97484	B	21.43	0.937	4.504	4.843	6.668	
V478 Cyg	A	16.67	0.879	4.464	4.566	6.807	2.67
HD193611	B	16.31	0.866	4.462	4.530	6.808	
CW Cep	A	13.52	0.766	4.440	4.245	6.788	2.39
HD218066	B	12.08	0.720	4.421	4.075	6.798	
QX Car	A	9.267	0.649	4.362	3.698	6.986	11.3
HD86118	B	8.480	0.611	4.343	3.544	7.000	
CV Vel	A	6.100	0.614	4.231	3.103	7.604	1.30
HD77464	B	5.996	0.603	4.228	3.070	7.607	
U Oph	A	5.198	0.538	4.198	2.820	7.687	0.43
HD156247	B	4.683	0.480	4.177	2.623	7.699	
ζ Phe	A	3.930	0.457	4.136	2.409	7.831	11.4
HD6882	B	2.551	0.283	4.028	1.633	7.836	
IQ Per	A	3.521	0.380	4.119	2.189	7.656	6.92
HD24909	B	1.737	0.195	3.891	0.906	7.688	
PV Cas	A	2.827	0.362	4.015	1.736	6.576	1.12
HD240208	B	2.768	0.351	4.011	1.698	6.577	
AI Hya	A	2.145	0.539	3.866	1.494	9.023	21.4
+0° 2259	B	1.978	0.395	3.865	1.204	9.025	
VV Pyx	A	2.101	0.349	3.920	1.331	6.850	32.2
HD71581	B	2.099	0.350	3.920	1.330	6.850	
RS Cha	A	1.858	0.324	3.893	1.174	6.925	1.57
HD75747	B	1.821	0.363	3.876	1.183	6.928	
EK Cep	A	2.029	0.228	3.952	1.217	7.429	10.3
HD206821	B	1.124	0.086	3.761	0.166	7.432	
MY Cyg	A	1.811	0.347	3.851	1.052	9.117	6.69
HD193637	B	1.786	0.329	3.853	1.025	9.121	

Table 2.2—Continued

System	Star	Mass	$\log R/R_{\odot}$	$\log T_e$	$\log L$	$\log \text{Age (yr)}$	χ^2
PV Pup	A	1.565	0.183	3.858	0.750	7.980	1.66
HD62863	B	1.554	0.182	3.855	0.738	8.101	
DM Vir	A	1.460	0.241	3.802	0.639	7.177	0.15
HD123423	B	1.454	0.240	3.800	0.633	7.180	
V1143 Cyg	A	1.391	0.169	3.789	0.447	7.323	9.13
HD185912	B	1.347	0.151	3.783	0.388	7.327	
UX Men	A	1.238	0.140	3.781	0.356	9.266	2.31
HD37513	B	1.198	0.119	3.773	0.283	9.303	

Figure 2.1 displays the resulting χ^2 for each binary pair, in order of descending mean mass. The binaries fall into three separate groups: ten have excellent fits ($\chi^2 < 4$; EM Car, V478 Cyg, CW Cep, CV Vel, U Oph, PV Cas, RS Cha, PV Pup, DM Vir and UX Men), six are marginal ($16 \leq \chi^2 \leq 4$; QX Car, ζ Phe, IQ Per, MY Cyg, EK Cep, and V1143 Cyg), and two are poor fits ($\chi^2 > 16$, denoted *offscale* in Figure 2.1; VV Pyx and AI Hya). The boundaries between these groups are indicated by vertical lines.

2.2.1 Global Aspects of the Errors

The weakness of a χ^2 measure is that it is most meaningful if the errors have a gaussian distribution around the mean (Press et al., (1992), chapters 14 and 15), which does not seem to be the case here. In particular, systematic shifts in the empirical data, due to new analyses, can give significant shifts in the error estimation. Ribas et al. (2000) have re-estimated the effective temperatures of 13 of the 18 binaries we have examined. Five (QX Car, U Oph, PV Cas, AI Hya, and RS Cha) were changed by more than twice the error estimates of either Ribas et al. (2000) or Andersen (1991). Further, Stickland, Koch & Pfeiffer (1992) and Stick-

land, Lloyd, & Corcoran (1994) have analyzed additional data (from IUE) and find masses of CW Cep and EM Car which lie beyond twice the error estimates. This is to be expected if the errors are dominated by systematic effects, and warns us to distrust all but our most robust inferences.

Because the fractional errors in mass and in radius are much more restrictive, it strongly supports the need for renewed efforts to pin down the effective temperatures of these stars. The choice of L and R rather than L and T_{eff} in our definition of χ^2 is significant: the smaller errors for R make the χ^2 more discriminating. Pols et al. (1997b) use R and T_{eff} which has the slight advantage here of involving less propagation of observational errors, but because R is much more precise than T_{eff} , the effect is small for the present data.

We have chosen to update the original data of Andersen (1991), incorporating the changes made by the Ribas et al. (2000) effective temperatures and the Stickland, Koch & Pfeiffer (1992) and Stickland, Lloyd, & Corcoran (1994) masses. We have used the new data for DM Vir (Latham et al., 1996). Our general conclusions are unaffected by which of these sets of data we use.

The comparison of observed and computed stars may be presented as an goodness of fit vector, which has the advantage of being directly representable in the HR diagram for the stars. The observed points with error bars are plotted along with an arrow indicating the distance and direction to the best model point. The way in which the models differ from the observations can then be taken in at a glance. Figure 2.2 shows the goodness of fit vectors, from the observed points (shown with error bars) to the best model star (chosen as described above). The largest discrepancy is the secondary of VV Pyx. Of the eight binaries (QX Car, ζ Phe, IQ Per, VV Pyx, AI Hya, EK Cep, MY Cyg, V1143) which have mediocre or poor fits, seven (QX Car is the exception) have at least one component lying in

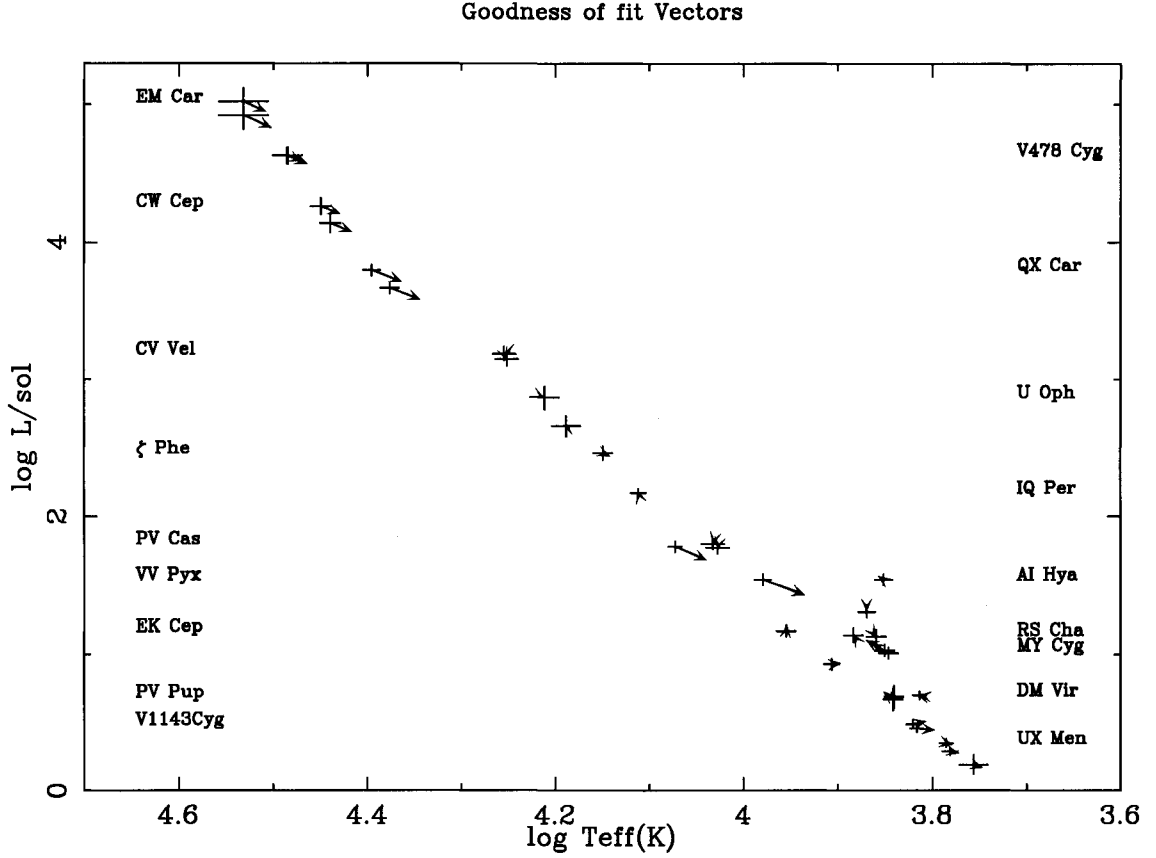


Figure 2.2: Goodness of fit vectors for selected binaries, with observational error bars.

the range $1.7 < M/M_{\odot} < 2.6$. Andersen, Nordström, & Clausen (1990) noticed similar behavior.

Figure 2.3 shows the luminosity differences between the models and the stars. The vertical axis is mass in solar units; binary components are connected by a line. The two binaries with $\chi^2 > 16$ (VV Pyx and AI Hya) are denoted by crosses; they are poor fits and should be given little weight. Considering the best fits, $\chi^2 < 4$ (solid squares), there is a dramatic trend: the highest mass models (for example, EM Car) are underluminous relative to the actual binaries, while the lower mass models are not.

Given the indications that the errors may be dominated by systematic effects,

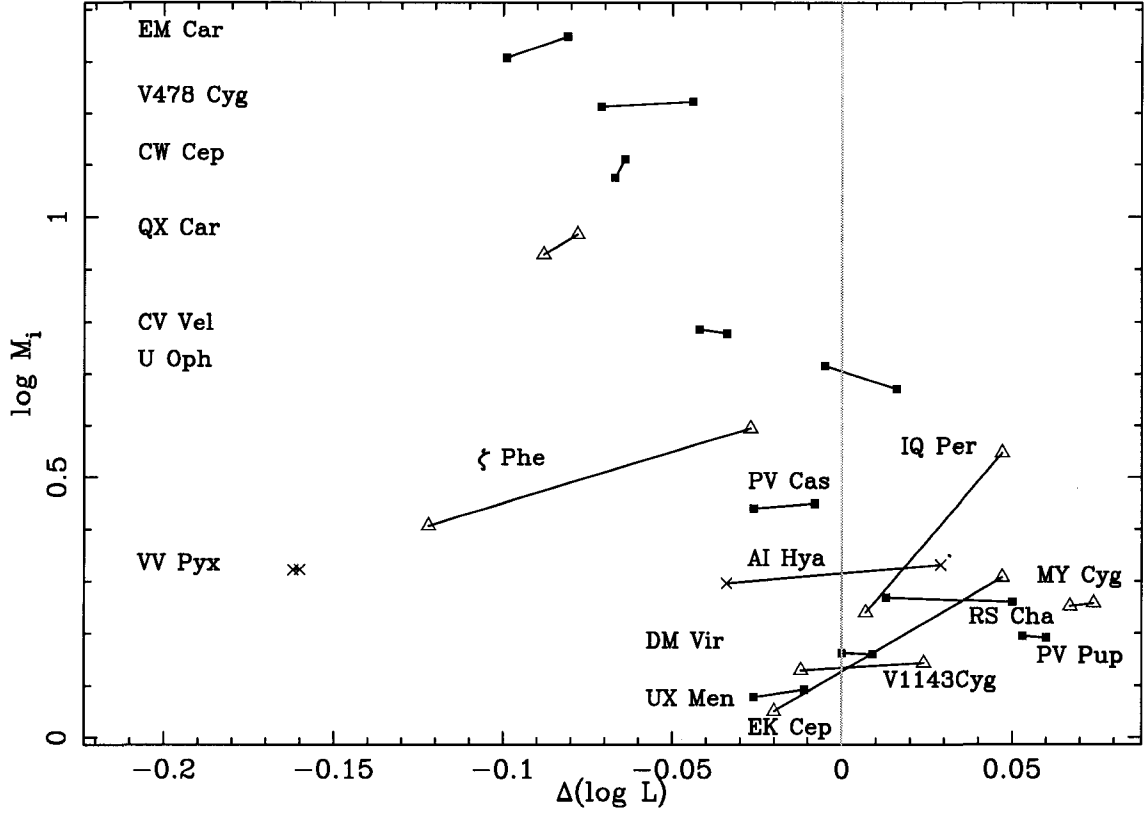


Figure 2.3: Luminosity differences between best fit models and observations.

we approach a statistical discussion with caution. The two binaries which have $\chi^2 > 16$ are eliminated from this statistical discussion on the basis that these fits are too poor to be meaningful. In principle, the mean errors could show a systematic shift in the models relative to the data, but because we choose an optimum pair of models, the choice masks any absolute shift. The error should reappear as a larger RMS difference. For luminosity, the first moment of the difference between model and stellar logarithmic luminosity is just the mean of this difference, which is -0.017 in the base ten logarithm (the models are too dim by this amount). The shift is smaller than the RMS error of the observational data, which is 0.056 . If there were a bad global mismatch, the RMS difference in "model minus star" would be much larger than the average error in the observations. However,

the RMS difference between the models and stars is 0.054, which is almost the same as the observational error. The luminosity is basically a measure of the leakage time for radiation, which is dominated by the value of the opacity in the radiative regions. It samples the whole star, including the deep interior. In a global sense, our mean leakage rate seems correct to the level of the statistical and observational error.

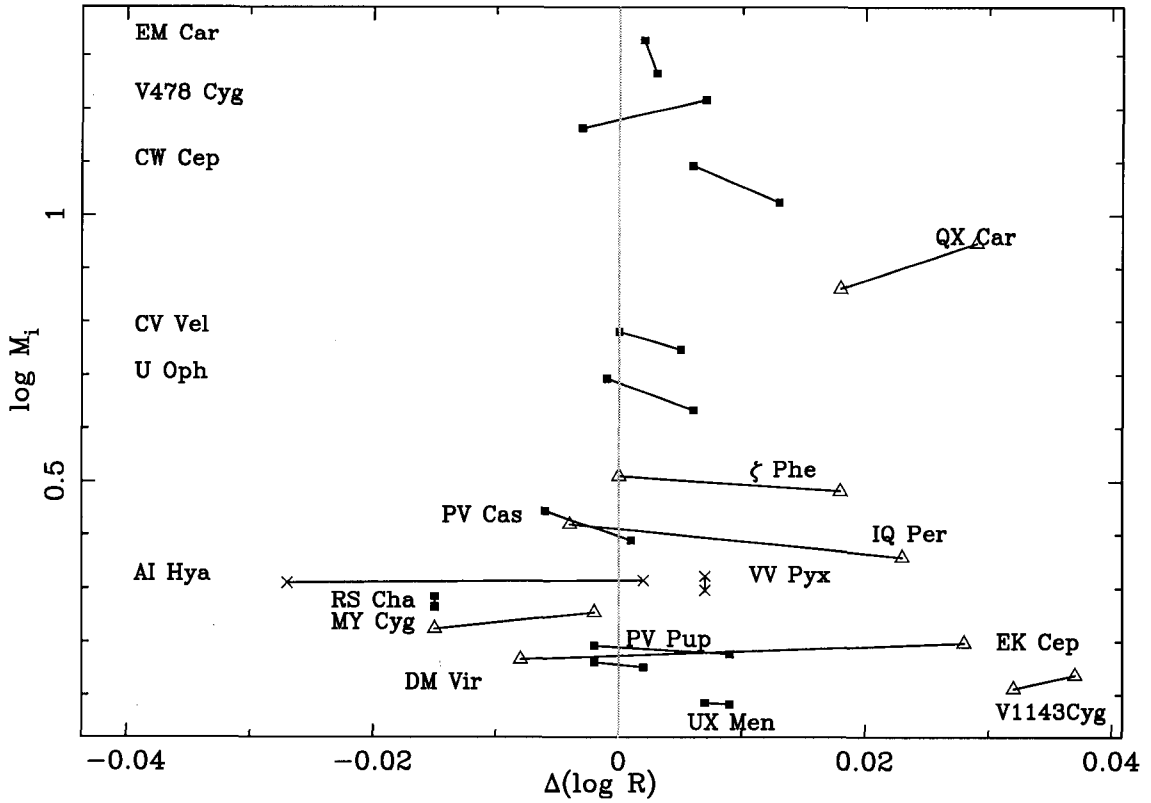


Figure 2.4: Radius differences between best fit models and observations.

The shifts in radius between the models and the stars are shown in Figure 2.4. The vertical axis and the symbols are the same as in the previous figure. The mean shift is 0.0053 in the logarithm (the models are too large by this small amount); the corresponding standard error of the Andersen data for which the fits are acceptable is 0.016, to be compared with an RMS difference between models and

stars of 0.014. Except for a few outlying cases, the distribution is fairly uniformly distributed around zero. If only the best fits (squares) are considered, a subtle trend might be inferred: 9 of 12 of the models above $4M_{\odot}$ have radii which are too large.

The corresponding mean shift in $\log T_{eff}$ is -0.007 (the models are too cool by this amount). Again, this is small in comparison to the standard error of the observations (0.014). The corresponding RMS difference between models and stars is 0.017. The effective temperature is a surface quantity, and is more sensitive to the outer layers which contain little of the stellar mass.

These numbers suggest that standard stellar evolutionary sequences of these stages should be able to produce luminosities, radii, and effective temperatures within 11, 3 and 4 percent, respectively, of good observational data. Otherwise, new physics is indicated. Because the standard stellar evolutionary models do this well, small “improvements” may contain no information. We will emphasize systematic trends, and those implications which emerge from several independent tests.

2.2.2 Massive Binaries

Figure 2.5 shows the evolution of the model stars in log luminosity and log radius, for EM Car, V478 Cyg, CW Cep, QX Car, CV Vel, and U Oph, corresponding to a mass range from 23 to $4.6 M_{\odot}$. Except for QX Car ($\chi^2 = 11.3$), models of these binaries have $\chi^2 < 4$, and so represent good fits. The error bars are centered on the observed stars; the arrows point from them to the optimum models. Notice the the fits can be multivalued because the trajectories may pass through the error boxes multiple times. This is shown occurring first as the model descends from the pre-main sequence (pre-MS), and again during main sequence hydrogen burning. If the stellar masses are significantly different, this ambigu-

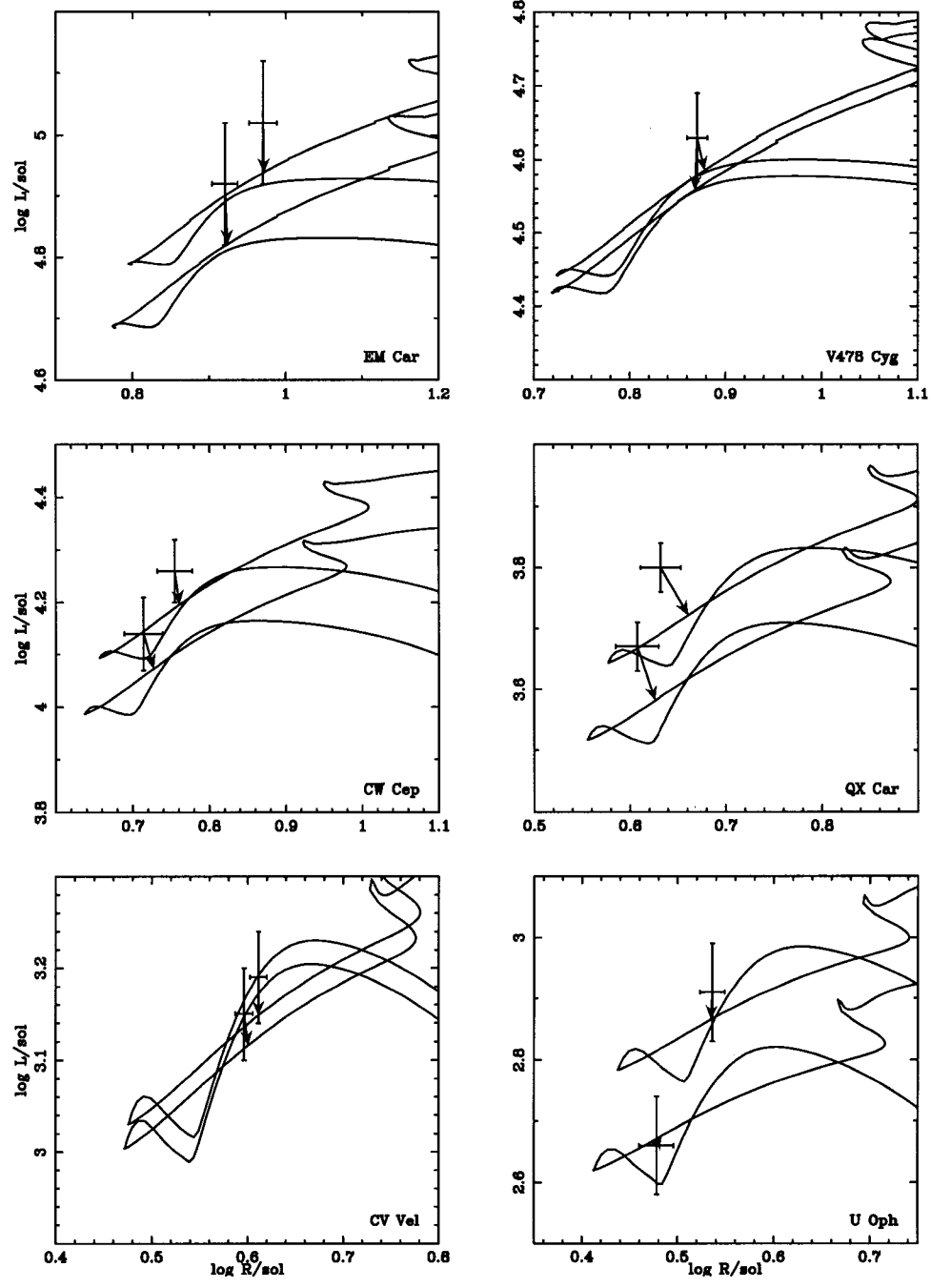


Figure 2.5: Massive models: EM Car, V478 Cyg, CW Cep, QX Car, CV Vel and U Oph. The masses range from 23 to $4.6 M_{\odot}$.

ity is removed by the condition that both components have the same age. All the model stars are too dim (all the arrows point downward), a signal that the standard stellar evolution prescription is systematically wrong.

EM Car, being the most massive system, also has the most significant mass loss. The model evolutionary sequences are set by the choice of initial mass, but the observational constraint on mass is applied after the best fitting model is determined. This is an implicit function of the choice of initial mass, and iteration is required. Initial masses of 22.91 and 20.91 produce masses at fit of 22.25 and 20.12 M_{\odot} , respectively. This mass ratio of 0.904 is consistent with the observational value of 0.910 ± 0.011 (Stickland, Lloyd, & Corcoran, 1994), and the masses agree with observation to within the estimated errors ($\pm 0.3 M_{\odot}$).

However, even this loss is still small. A loss of $0.7 M_{\odot}$ is about twice the uncertainty in mass determination, $\pm 0.32 M_{\odot}$. Such a change in mass, since $L \propto M^4$, corresponds to a shift in luminosity of $\Delta \log L \approx 0.05$, to be compared to the observational error in luminosity of $\Delta \log L = 0.1$, which is still larger. This is due to the fact that effective temperature is less well determined than the radius. A concentrated effort to refine the effective temperature determinations for EM Car, V478 Cyg, CW Cep, QX Car, CV Vel, and U Oph would translate directly into much sharper constraints on massive star evolution. Ribas et al. (2000) have revised the effective temperature for QX Car (upward) by twice the quoted error, so that the inferred luminosity increases. Prior to this revision, the fit to QX Car was good ($\chi^2 < 4$). This larger discrepancy for QX Car is in the same sense as noted for the other massive systems; the models are dimmer than the stars. Taking the larger masses from Andersen (1991), with or without mass loss, still gives good fits, and the models are still dimmer than the stars. The result seems robust.

Pachoulakis et al. (1996) have used high resolution spectral images obtained

with the International Ultraviolet Explorer (IUE) to study the winds from CW Cephei (HD 218066). They place upper limits on the mass-loss rates of $1.0 \times 10^{-8} M_{\odot} \text{ yr}^{-1}$ for the primary and $0.32 \times 10^{-8} M_{\odot} \text{ yr}^{-1}$ for the secondary. The model masses start at 12.9 and 11.9 and decrease only to 12.8 and 11.88 respectively, to be compared to 12.9 ± 0.1 and $11.9 \pm 0.1 M_{\odot}$ (Stickland, Koch & Pfeiffer, 1992). The mass loss predicted by the Kudritzki et al. (1989) theory for our models at the point of minimum error is $0.66 \times 10^{-8} M_{\odot} \text{ yr}^{-1}$ for the primary, and $0.43 \times 10^{-8} M_{\odot} \text{ yr}^{-1}$ for the secondary. If the upper limits were detections, this could be considered good agreement, considering the complexity of the problem of interpreting the system (Pachoulakis et al., 1996). The net loss of mass up to this point is no larger than the error in mass determination, $\pm 0.1 M_{\odot}$. Because the mass loss rate is restricted by these observations to be at or below the value we use, the mass loss process should have no larger effect than we compute. Hence, the remaining discrepancy must come from some other effect.

Table 2.3 gives the instantaneous mass loss rates from the models, at the point of optimum fit, for the most massive binary systems. At lower masses, the mass loss rates are smaller still. Additional observational data on mass loss for these systems could prove crucial in clarifying the role of mass loss in stellar evolution.

Ribas et al. (2000) estimate ages for EM Car and CW Cep. Their procedure not only gives ages, but also error estimates for those ages. Our ages agree with theirs to within these errors, even though we use no overshooting and they do. It may be that the convective region in high mass stars is sufficiently large that the gross evolutionary properties of stars on the main sequence are not greatly affected by the overshooting correction. The understanding of the physics of overshooting is still too preliminary to do more than speculate on this issue.

Pols et al. (1997b) find acceptable fits for EM Car, V478 Cyg, CW Cep, QX

Table 2.3. Predicted instantaneous mass loss rates.

System	Star	Mass	Mass Loss Rate ^a
EM Car	A	22.35	1.82×10^{-7}
	B	20.51	1.17×10^{-7}
V478 Cyg	A	16.78	2.50×10^{-8}
	B	16.47	2.28×10^{-8}
CW Cep ^b	A	12.87	0.66×10^{-8}
	B	11.88	0.43×10^{-8}
QX Car	A	9.257	1.31×10^{-9}
	B	8.479	6.32×10^{-11}

^aPredicted instantaneous mass loss rate in M_{\odot}/yr .

^bFor IUE upper limit, see Pachoulakis et al. (1996).

Car, and U Oph (it is probable that QX Car would not have been a good fit with the revised effective temperatures), but with increasingly lower heavy element abundances with increasing mass. EM Car and V478 Cyg have fits at the limit of the heavy element abundance range. Ribas et al. (2000) find a similar effect: the heavy element abundances of their massive binaries are marginally smaller than those of the less massive ones. Their effect is not quite as obvious as in Pols et al. (1997b), perhaps because Ribas et al. (2000) do not force the helium abundance to correlate with heavy element abundance, and it fluctuates for these systems. The added degree of freedom may allow the fitting procedure to obscure the trend.

This behavior could be interpreted as a galactic evolutionary effect, which would be extremely interesting, but there is another possibility. The problem with the massive models (see Figure 2.2 and Figure 2.3) is that they are too dim. Lower heavy element abundance gives higher luminosity because of reduced opacity. The fitting algorithms, having little freedom for mass variation (thanks to the high quality of the data), must find lower heavy element abundance preferable, whether or not the heavy element abundances are actually smaller. More effective mixing, giving larger cores, also results in higher luminosities even if the abundances are unchanged. *It is crucial to obtain spectroscopic information to decide the issue.* Guinan et al. (2000) have recently examined V380 Cyg, which is a binary of disparate masses ($11.1 \pm 0.5 M_{\odot}$ and $6.95 \pm 0.25 M_{\odot}$) and evolutionary state. They conclude that more mixing is needed ($\alpha_{OV} = 0.6 \pm 0.1$). However, this system is complicated. Guinan et al. estimate that the system is approximately ten thousand years from Roche lobe overflow by the primary. Thus, conclusions based on this system should be made with caution.

The overshoot parameter α_{OV} may be a function of mass (at least). Similar behavior can also be seen in Claret & Giménez (1991), which finds different val-

ues of the best fit overshoot parameter for five different masses. Alternatively, rotational mixing might be increasingly effective for larger masses. Phenomenological prescriptions are valuable if they capture the essential physics of the phenomena; if fitted parameters turn out to be variable, a new formulation is needed. We have at least three causes for one effect; sorting this out is an interesting theoretical and observational challenge.

2.2.3 Intermediate Mass Binaries

Figure 2.6 shows ζ Phe, IQ Per, PV Cas, AI Hya, VV Pyx, and RS Cha, the group which has some of the most challenging binaries. The masses range from 3.9 to $1.1 M_{\odot}$.

Both ζ Phe and IQ Per have a mass ratio significantly different from one: 0.65 and 0.49 respectively. Because the more massive components will evolve more rapidly, common age is a stringent constraint. In both cases, the error is dominated by the less massive component. For ζ Phe, the $2.55 M_{\odot}$ secondary is brighter than the model; Pols et al. (1997a) have the same problem. Ribas et al. (2000) avoid it by using a lower heavy element abundance (0.013) and a higher helium abundance (0.29). The heavy element abundance might be tested by high resolution spectroscopy. For IQ Per, the $1.74 M_{\odot}$ secondary is too blue; its evolutionary track never gets so hot. Pols et al. (1997b) attribute the difficulty in fitting ζ Phe and IQ Per to problems in determining T_{eff} of the secondary (Andersen, 1991), which is much dimmer because of the large mass ratios of the components.

For ζ Phe and IQ Per, it is clear that much of our “difficulty” is due to the relatively small error bars; see Figure 2.2. Consequently, small changes may improve the χ^2 significantly, even if they do not correspond to the physics of the system. In the case of IQ Per, use of the Ribas et al. (2000) value of effective temperature improves the fit, compared to Pols et al. (1997a), as does adjustment of

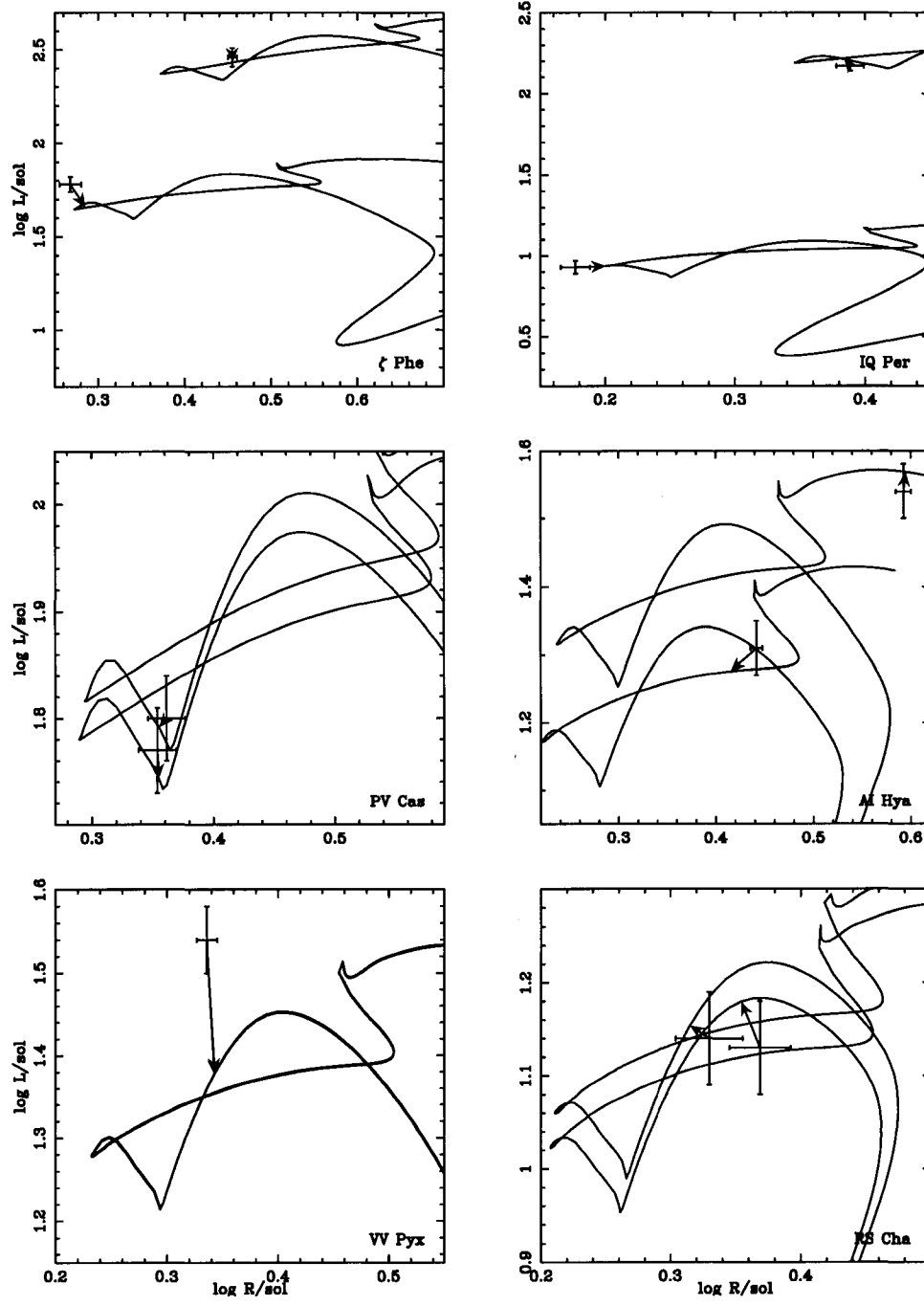


Figure 2.6: Intermediate mass models: ζ Phe, IQ Per, PV Cas, AI Hya, VV Pyx and RS Cha. The masses range from 3.93 to 1.74 M_{\odot} .

the abundances.

AI Hydrae is particularly interesting because the primary is fitted by a model which is swiftly evolving, so that catching it in such a stage is unlikely. Overshoot from the convective core would broaden the main sequence band and increase the age of the fast evolving primary, allowing the possibility of a fit with a more probable, slower evolutionary stage. This is consistent with the conclusions of Pols et al. (1997b), who find that AI Hya is the only binary for which the overshooting models give a greatly improved fit.

Some of the AI Hya behavior can be attributed to heavy element abundance effects. Both members are classified as peculiar metal line stars. The heavy element abundance of this system (from multi-color photometry) is 0.07 (Ribas et al., 2000), which is 3.5 times the value used in the models. The true interior composition cannot be this metal rich. We have examined a sequence which had a heavy element abundance of 0.03 rather than 0.02. This modest change gave a dramatic shift toward lower luminosity ($\Delta \log L \approx 0.06$, which is three times the observational error) and cooler effective temperatures ($\Delta \log T_e \approx 0.027$, which is also three times the observational error). However, if the heavy element abundance were high only near the surface of the star, the opacity effects would produce a shift to the red in the evolutionary tracks, which would bring the models much more in line with the observations.

VV Pyx has almost identical components, so that their coeval origin has almost no effect on the fit. They track the same path at essentially the same time. The fit is simply the point that the observational error box is most closely approached, and should be viewed with caution, especially as the models give a poor fit.

Only PV Cas and RS Cha have good fits ($\chi^2 < 4$), and they are pre-main

sequence (pre-MS). RS Cha has previously been suggested to be in a pre-main sequence stage (Mamajek, Lawson & Feigelson, 1999). The pre-MS identification would have important theoretical implications. If true, it implies that the error in the models occurs after the core convection has been established in these stars. In any case, convection is an interesting possible cause for the problem; these binaries have at least one component with convective core burning. PV Cas has sufficiently different masses to require us to examine the pre-MS fit seriously.

2.2.4 Is PV Cas Pre-Main Sequence?

Questions have been raised about the evolutionary status of PV Cas since Popper (1987). Previous attempts to fit the system to main sequence models (Pols et al., 1997a) have been unsatisfactory, mainly due to a large and irreconcilable age discrepancy between the members. Fitting both components to pre-MS models, however, produces excellent agreement.

To test the case for PV Cas being pre-MS, we looked for other observation clues. The double-lined eclipsing binary system RS Cha was recently found by Mamajek, Lawson & Feigelson (1999, 2000) to be pre-MS. Not only were pre-MS tracks for RS Cha a better fit than post-MS tracks, but two other observations strengthened the argument: (1) RS Cha had several nearby *ROSAT* All-Sky Survey X-ray sources nearby which were found to be very young, low-mass, weak-lined T Tauri stars, and (2) RS Cha's proper motion matched that of the T Tauri stars, suggesting a genetic tie. PV Cas is at a distance of 660 pc (Popper, 1987), and a young stellar aggregate or membership within an OB association could have been previously overlooked.

Searching the Hipparcos and Tycho-2 catalogs, as well as examining PV Cas on the Digitized Sky Survey, we found no evidence for PV Cas being a member of a known OB Association. More massive members of a putative association would

be included in the Hipparcos catalog with proper motions similar to that given in the Tycho-2 entry for PV Cas, but none were found. We searched for known groups of young stars with VizieR at CDS: the compilations of OB Associations by Ruprecht, Balazs, & White (1982), Melnick & Efremov (1995), and de Zeeuw et al. (1999), and open clusters by Ruprecht, Balazs, & White (1983) and Lyngå (1987). The only possible known associations that PV Cas could belong to are Cep OB3 ($d=840$ pc, $\Delta\theta = 4.0^\circ$, $v_R = -23$ km/s) and Cep OB2 ($d=615$ pc, $\Delta\theta = 9.5^\circ$, $v_R = -21$ km/s), however their projected separations from PV Cas are large (600 pc and 100 pc, respectively), and their average radial velocities are far from Popper's value for PV Cas ($v_R = -3$ km/s). Hence, PV Cas does not appear to be connected to any known OB Associations or clusters which help us to infer its nature.

The *ROSAT* All-Sky Survey (RASS) Bright Source Catalog (BSC; Voges et al. (1999)) and Faint Source Catalog (FSC; Voges et al. (2000)) were searched to see whether there was any evidence for a clustering of X-ray-emitting T Tauri stars in the vicinity of PV Cas. No concentration of sources near PV Cas was detected, although the sensitivity of RASS at 660 pc is about $L_x \simeq 10^{31}$ erg s $^{-1}$, corresponding to the very high end of the X-ray luminosity function for T Tauri stars (Feigelson & Montmerle, 1999). Only one RASS-BSC source was within $30'$ (~ 6 pc projected) of PV Cas, but its f_X/f_V ratio was 2 magnitudes too high to be a plausible T Tauri star candidate. The only RASS-FSC source within $30'$ of PV Cas appeared to be related to a galaxy cluster on the Digitized Sky Survey.

We conclude that we currently have no evidence for a pre-MS aggregate around PV Cas which could strengthen the argument for its pre-MS status. However, the Taurus clouds also are forming low mass pre-MS stars without high mass cluster counterparts.

2.2.5 Lower Mass Binaries

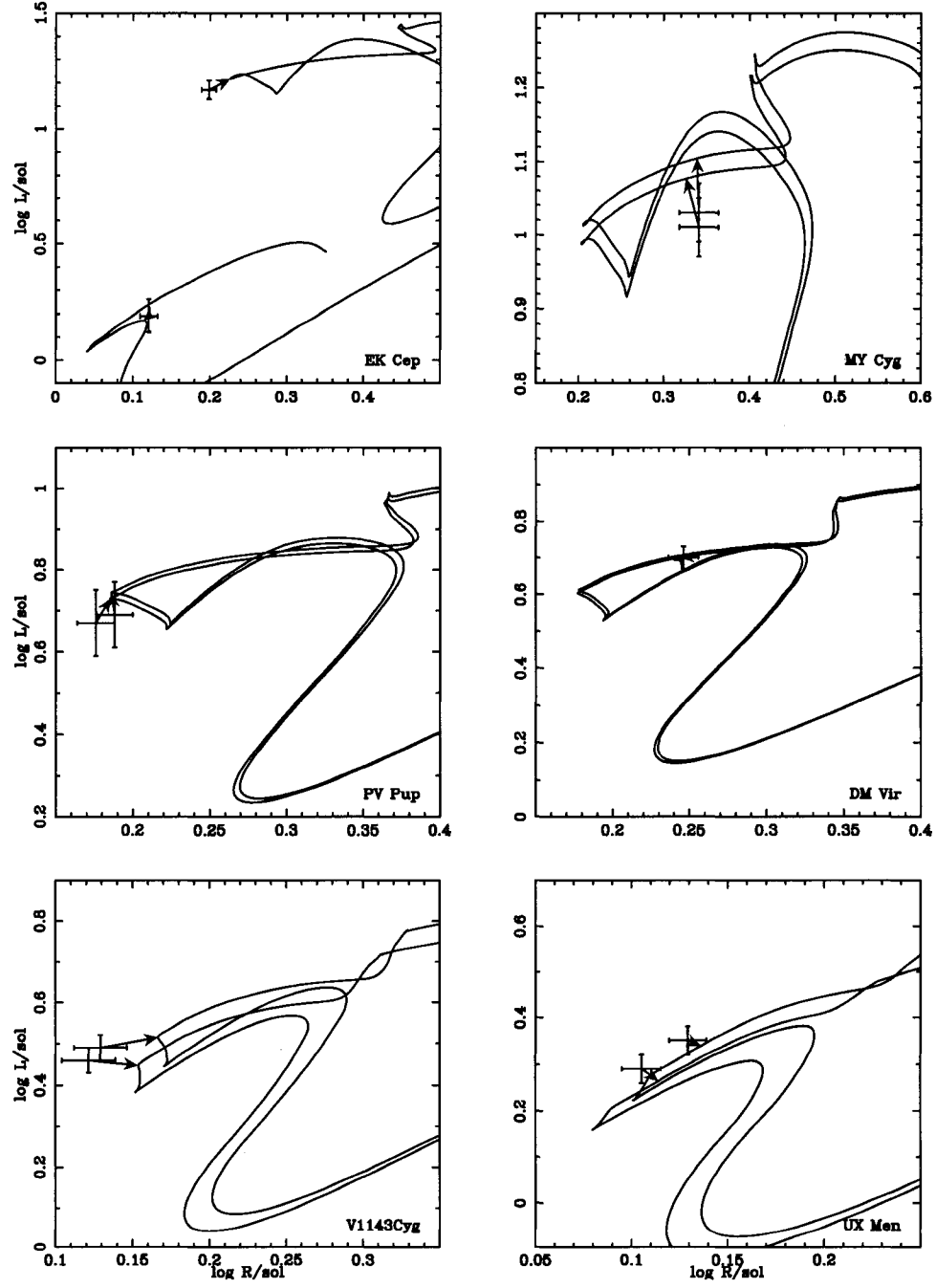


Figure 2.7: Lower mass models: EK Cep, MY Cyg, PV Pup, DM Vir, V1143 Cyg, and UX Men. The masses range from 2.03 to $1.12 M_{\odot}$.

Figure 2.7 shows EK Cep, MY Cyg, PV Pup, DM Vir, V1143 Cyg, and UX Men, whose masses range from 2.03 to 1.12 M_{\odot} . The Ribas et al. (2000) effective temperatures improve the fit for UX Men.

EK Cep has a large mass ratio. The optimum fit occurs as EK Cep B is still on the pre-MS track, in agreement with Martin & Rebolo (1993) and Claret, Giménez, & Martin (1995). We find that the surface abundance of Li^6 is depleted to about 10^{-4} of its initial value, while Li^7 is depleted from 1.47×10^{-9} to 0.393×10^{-9} . This corresponds to a depletion of elemental lithium of about 0.57 dex (base 10 logarithm). This is somewhat larger than found by Martin & Rebolo (1993) (0.1 dex), but may be due to differences in the nuclear reaction rates used. In this range, the depletions are almost linear in the net cross section for Li^7 destruction. A careful analysis with a variety of rates is warranted: Martin & Rebolo (1993) suggest that the observations are in conflict with pre-MS models giving a Li depletion greater than 0.3 dex.

Although EK Cep has a large χ^2 ($\chi^2 = 10.3$) if the radii are used in determining the fitting function, the situation is different for $\log L$ - $\log T_{\text{eff}}$, the conventional HR plane. The observational errors are now larger, and the corresponding χ^2 approaches 4. This confirms the importance of using the radii directly as a discriminant (Andersen, 1991).

MY Cyg and UX Men are found to be well into main sequence hydrogen burning. MY Cyg is underluminous relative to the models. A higher heavy element abundance would remove the discrepancy; observational tests of this are needed. Pols et al. (1997b) found $Z = 0.024$ and Ribas et al. (2000) found $Z = 0.039$, which are consistent with this suggestion.

PV Pup and V1143 Cyg are on the pre-MS/MS boundary. The fitting procedure chooses the cusp at which the star settles down to main sequence burning.

This cusp shifts with small changes in abundance, so these fits would benefit from independent measurement of the abundances in these binaries.

DM Vir has been updated for Latham et al. (1996). Although the changes were small, the new fit is in the middle of main sequence hydrogen burning instead of pre-MS contraction. The track lies well within the error bars; the previous data also had $\chi^2 < 4$, although a much younger age estimate. Because the masses are almost equal, the coeval birth requirement has little effect, and the ages have a corresponding uncertainty.

2.2.6 Roche Lobes

Observational selection favors binaries with a small separation. In order to determine the true usefulness of these systems as tests of models of single star evolution it is necessary to know to what extent these systems are detached (noninteracting), and how far into the past and the future this condition is satisfied.

In order to answer this question to first order for the systems in our sample, the average Roche lobe radius for each star was calculated using

$$R_{Roche} = \frac{0.49a}{0.6 + q^{-2/3} \ln(1 + q^{1/3})}$$

where a is the binary separation and q is the mass ratio with the star in question in the numerator (Lewin, van Paradijs, & van den Heuvel, 1995). This average radius was then compared to the model radii to estimate when each star overflows its Roche lobe. Dynamical evolution of the orbits was not taken into account. None of the models indicated significant mass transfer prior to the ages of the models closest to the observed points since early in the pre-Main Sequence evolution.

Four of the binaries in the sample have at least one member which, according to the model radii, will overflow their Roche lobes when they are between 1.3 and

2 times older than their current age. The results of the Roche lobe comparisons are given in Table 2.4. All stars labeled “Post” do not exceed their Roche Lobe radius until well into their post-main sequence evolution. Two stars are in contact early in the pre-main sequence evolution (EK Cep B and MY Cyg A). The times given for these stars correspond to when they contract below the critical radius and mass transfer ends. These numbers should be taken as a rough guideline at best, since the dynamical evolution of protostars is undoubtedly more complex than the simple algorithm used here. The models corresponding to the primaries EM Car and V478 Cyg exceed their Roche lobe radii in less than 3×10^6 years.

Table 2.4. Roche lobe parameters for selected binary systems.

System	Star	Mass	a/R_{\odot}	e	R/R_{\odot}	R_{roche}/R_{\odot}	log Age (yr)	log Age(over)
EM Car	A	22.89	33.75	0.0120 ± 5	9.34	12.9	6.666	6.795
	B	21.43			8.33	12.6	6.668	6.832
V478 Cyg	A	16.67	27.31	0.019 ± 2	7.42	10.5	6.807	6.949
	B	16.31			7.42	10.2	6.808	6.965
CW Cep	A	13.52	24.22	0.0293 ± 6	5.68	9.33	6.788	7.085
	B	12.08			5.18	8.91	6.798	7.168
QX Car	A	9.267	29.82	0.0278 ± 3	4.29	11.5	6.986	Post
	B	8.480			4.05	11.0	7.000	Post
CV Vel	A	6.100	34.97	$< 4 \times 10^{-3}$	4.09	17.0	7.604	Post
	B	5.996			3.95	13.2	7.607	Post
U Oph	A	5.198	12.76	0.0031 ± 2	3.44	4.90	7.687	7.910
	B	4.683			3.01	4.68	7.689	8.030
ζ Phe	A	3.930	11.04	0.0113 ± 20	2.85	4.57	7.831	8.276
	B	2.551			1.85	3.80	7.836	8.797
IQ Per	A	3.521	10.58	0.076 ± 4	2.45	4.68	7.656	8.405
	B	1.737			1.50	3.39	7.688	Post
PV Cas	A	2.827	10.85	0.032 ± 1	2.30	4.07	6.576	8.669
	B	2.768			2.26	4.07	6.577	8.697
AI Hya	A	2.145	27.63	0.230 ± 2	3.91	10.7	9.023	Post
	B	1.978			2.77	10.2	9.025	Post
VV Pyx	A	2.101	18.77	0.0956 ± 9	2.17	7.08	6.850	9.066
	B	2.099			2.17	7.08	6.850	Post
RS Cha	A	1.858	9.14	0.030 ± 15	2.14	3.47	6.925	Post
	B	1.821			2.34	3.47	6.928	Post
EK Cep	A	2.029	16.64	0.190 ± 3	1.58	7.08	7.429	Post
	B	1.124			1.32	5.50	7.432	5.669
MY Cyg	A	1.811	16.27		2.19	6.17	9.117	5.646
	B	1.786			2.19	6.17	9.121	Post
PV Pup	A	1.565	8.62	0.050 ± 1	1.54	6.17	7.980	Post
	B	1.554			1.50	6.17	8.101	Post
DM Vir	A	1.460	16.79	$< 10^{-4}$	1.73	6.31	7.177	Post
	B	1.454			1.73	6.31	7.180	Post

Table 2.4—Continued

System	Star	Mass	a/R_\odot	e	R/R_\odot	R_{roche}/R_\odot	log Age (yr)	log Age(over)
V1143 Cyg	A	1.391	22.83	0.540 ± 5	1.35	8.71	7.323	Post
	B	1.347			1.32	8.51	7.327	Post
UX Men	A	1.238	14.69	0.015 ± 17	1.35	5.62	9.266	Post
	B	1.198			1.27	5.50	9.303	Post

These values are approximate in that dynamical evolution is not taken into account, the model radii do not match exactly the observed radii, and an approximate Roche lobe geometry was used to facilitate comparison to the spherically symmetric models.

2.3 Apsidal Motion

Apsidal motion in binaries allows us to infer constraints on the internal mass distributions (Schwarzschild, 1957). Apsidal motion, that is, rotation of the orientation of the orbital ellipse relative to an inertial frame, does not occur for binary orbits of point particles interacting by Newtonian gravity. Levi-Civita (1937) showed that the general relativistic expression for the periastron shift of a double star is the same as for the perihelion shift of Mercury. Following Weinberg (1972) (see pages 194-7), the shift is

$$(P/U)_{GR} = 3G(M_A + M_B)P/a(1 - e^2)c^2, \quad (2.2)$$

where c is the speed of light and G the gravitational constant. Using units of solar masses and radii, and with the period P in days, this dimensionless number becomes

$$(P/U)_{GR} = 6.36 \times 10^{-6}(M_A + M_B)P/a(1 - e^2), \quad (2.3)$$

apsidal orbits per orbit. Tests of general relativity have reached high precision (Will, 1998); the perihelion shift has now been tested to about 3×10^{-3} . There has been some controversy as to a possible breakdown of general relativity because of a discrepancy between observations and predictions of the apsidal motion of some systems. This has been clarified by Claret (see Claret (1997, 1998) for a recent discussion), who pointed out errors in theoretical models and difficulties in observations, especially for systems whose apsidal periods are too long for much to be measured with modern equipment. We adopt the point of view that general relativity is better tested than subtleties in the evolution of binary stars, and ascribe errors to other causes (tidal effects not included, rotational effects, and systematic errors in observational interpretation, for example).

Tides induced by each companion give an additional interaction which is not purely inverse square in the separation and cause apsidal motion. Quataert, Kumar & On (1996) have discussed the validity of the classical formula, which we use,

$$(P/U)_{CL} = (15/a^5)[k_1 R_1^5 M_2/M_1 + k_2 R_2^5 M_1/M_2]f(e), \quad (2.4)$$

where P is the period of the orbit, U the period of apsidal motion, M_i the mass and R_i the radius of the star i , and

$$f(e) = (1 + \frac{3}{2}e^2 + \frac{1}{8}e^4)/(1 - e^2)^5, \quad (2.5)$$

where e is the eccentricity of the orbit. The separation of the pair in solar radii is

$$a = 4.207 P^{\frac{2}{3}} (M_1 + M_2)^{\frac{1}{3}}, \quad (2.6)$$

if the period P is measured in days and the masses in solar units. The classical apsidal motion formula gives accurate results when the periods of the low-order quadrupole g , f and p -modes are smaller than the periastron passage time by a

factor of about 10 or more (Quataert, Kumar & On, 1996). For EM Car, the lowest order pulsational mode of the primary has a period of 0.324 days compared with the orbital period of 3.414 days and an eccentricity of 0.0120 ± 5 , so that this condition is just satisfied.

If we assume that the observed apsidal motion is due only to these two effects, classical simple tides and general relativity, we have

$$(P/U)_{OBS} - (P/U)_{GR} = (P/U)_{CL}. \quad (2.7)$$

We use the products $k_i R_i^5$ directly for greater precision, but quote the apsidal constants k_i for comparison. Petrova (1995) has pointed out that accuracy problems may exist because the relevant parameter is $k_i R^5$, where k_i is the apsidal constant and R is the stellar radius, not just k_i alone.

Figure 2.8 shows the integrand of the apsidal constant, which approaches an asymptotic value as the integration exceeds about 0.7 of the radius. Inner regions contribute little because of their small radii; outer regions have little mass. The change from the interior (Henye) integration to envelope integration occurs around $r/R = 0.5$, and is visible in the change in the density of points. At the join, the temperature is about $T \approx 6 \times 10^6$ K, and the density $\rho \approx 2.0 \times 10^{-2}$ gcm⁻³. This temperature is about ten times the value attained in the early opacity experiments (Perry et al., 1991, 1996) on the NOVA laser, and is about half the goal for the National Ignition Facility (NIF). For such main sequence (and pre-main sequence) stars, the apsidal constants are most sensitive to the range of density and temperature which is directly accessed by high energy density laser experiments (see Remington et al. (1999) and discussion above). In this range, the new opacities show significant deviation from those previously used in astrophysics (Rogers & Iglesias, 1992; Iglesias & Rogers, 1996).

The Petrova & Orlov (1999) catalog contains orbital elements for 128 binaries,

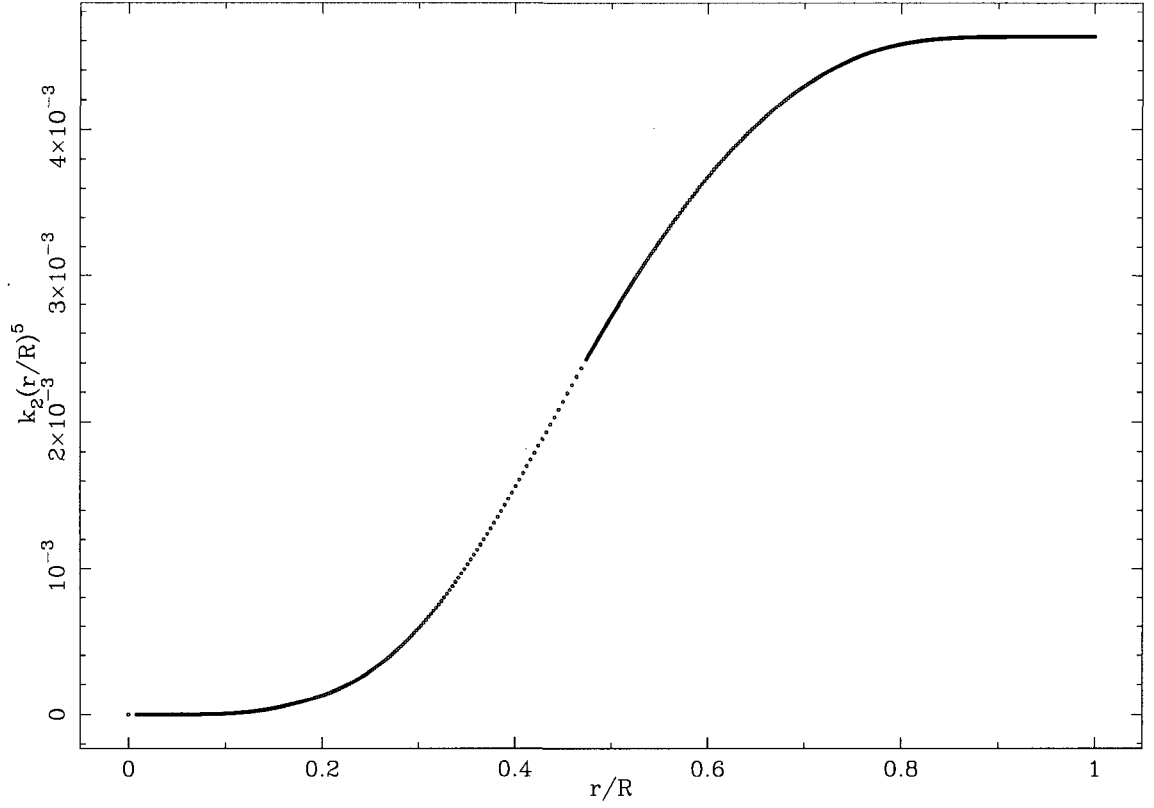


Figure 2.8: Apsidal constant integrand for EM Car primary.

including most (11 of 18) of the binaries in our list. Table 2.5 gives apsidal constants k_i , as well as the observed and predicted ratios of P/U . Given the significant improvement in the opacities, a critical re-examination of these data seems warranted.

Table 2.5. Apsidal comparisons for selected binary systems.

System	Star	Mass	$-\log k_i$	$(k_2 R^5)^a$	P/U_{CL}^b	P/U_{GR}^b	P/U_{CL+GR}^b	P/U_{OBS}^b
EM Car	A	22.35	2.240	437.9	2.46	0.275	2.74	2.2 ± 0.3
	B	20.51	2.180	290.8				
V478 Cyg	A	16.78	2.185	169.8	3.21	0.223	3.43	3.0 ± 0.3
	B	16.47	2.175	154.7				
CW Cep	A	12.87	2.106	52.86	1.61	0.178	1.79	1.640 ± 0.014
	B	11.88	2.090	37.23				
QX Car	A	9.257	2.122	16.20	0.171	0.170	0.341	0.340 ± 0.006
	B	8.479	2.117	10.96				
U Oph	A	5.198	2.266	2.721	1.85	0.0827	1.93	2.2 ± 0.3
	B	4.683	2.256	1.549				
ζ Phe	A	3.930	2.308	0.9756	0.765	0.0624	0.827	1.03 ± 0.15
	B	2.551	2.333	0.1315				
IQ Per	A	3.521	2.278	0.4619	0.363	0.0553	0.418	0.40 ± 0.03
	B	1.737	2.416	0.0401				
PV Cas	A	2.815	2.321	0.2647	0.538	0.0572	0.597	0.510 ± 0.011
	B	2.756	2.323	0.2705				
VV Pyx	A	2.101	2.488	0.1578	0.0215	0.0661	0.0876	0.0039 ± 0.0012
	B	2.099	2.488	0.1572				
EK Cep	A	2.029	2.377	0.05895	0.0153	0.0575	0.0728	0.0030 ± 0.0009
	B	1.246	1.867	0.04084				
V1143 Cyg	A	1.391	2.351	0.02735	0.0106	0.0823	0.0929	0.00195 ± 0.00011
	B	1.347	2.288	0.02657				

Table 2.5—Continued

System	Star	Mass	$-\log k_i$	$(k_2 R^5)^a$	P/U_{CL}^b	P/U_{GR}^b	P/U_{CL+GR}^b	P/U_{OBS}^b
--------	------	------	-------------	---------------	--------------	--------------	-----------------	---------------

^aRadii R in solar units.

^bMultiply tabular value by 10^{-4} .

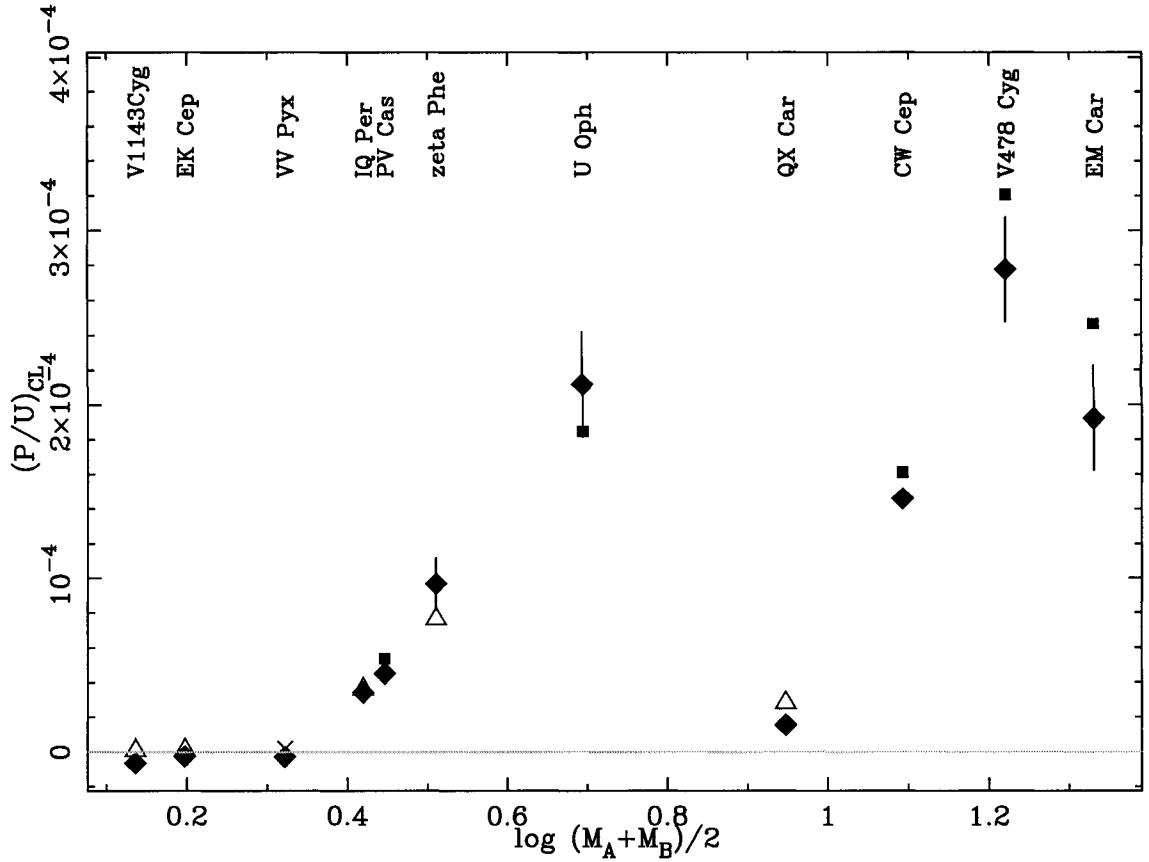


Figure 2.9: Classical apsidal motion versus mean mass, for our binaries with measured apsidal motion. $(P/U)_{CL} = (P/U)_{OBS} - (P/U)_{GR}$ is assumed.

Figure 2.9 shows the dimensionless rate of apsidal motion, $(P/U)_{CL} = (P/U)_{OBS} - (P/U)_{GR}$, which would be due to classical apsidal motion, plotted versus log of half the total binary mass. P is the orbital period and U the apsidal period. The

observational data (corrected for general relativity) are shown as diamonds, with vertical error bars. The model predictions are shown as solid squares ($\chi^2 < 4$) for the best fits, open triangles for $4 < \chi^2 < 16$, and crosses for $\chi^2 > 16$. The massive binaries with good fits (EM Car, V478 Cyg, and CW Cep; $(M_A + M_B)/2 > 10M_\odot$) have predicted apsidal motion in excess of that observed, and QX Car also follows that trend. These models are not as centrally condensed as the stars. This may be related to the underluminosity of these models found above. Additional mixing would give more massive, convective cores, which would result in both greater luminosity and more centrally condensed structure.

Of the lower mass binaries with measured apsidal motion, only PV Cas has a good fit model. Its predicted apsidal motion is also larger than that observed (the stars are more centrally condensed). The other binaries need better fitting models before the tests can be convincing. Note that at the lowest tick mark in Figure 2.9, the apsidal period is measured in centuries.

Claret & Giménez (1993) have shown that inclusion of (a) overshooting, (b) variation in heavy element abundance, and (c) rotation can produce models consistent with the apsidal data; see also (Claret, 1999). This represents good progress toward establishing the apsidal motion data as a useful test of stellar evolution. Our results, while not based upon identical assumptions, are consistent. The challenge is that of correctly determining the relative importance of the several different small effects which can give consistency with the observations.

2.4 Conclusions

Standard stellar evolution, without embellishments such as overshooting and rotation, does fairly well on these quantitative tests. While clear discrepancies exist, they are relatively subtle. This makes it difficult to uniquely identify exactly

which additional physics is needed. We find a detailed consistency with similar calculations by Pols et al. (1997b) and Ribas et al. (2000). It is important to test observationally the abundance variations implied by χ^2 optimization, as such procedures may hide missing physics in parameter variation. Laser experiments now explore the regions of temperature and density which are relevant not only to conventional stellar evolution, but also to apsidal motion tests.

Massive stars require more mixing than given by standard stellar evolution, and probably more than the prescriptions for overshooting used by Pols et al. (1997b) and Ribas et al. (2000). Rotational mixing, overshooting which is mass dependent, or something else is needed. Our mass loss prescription is near the observational upper limit, so that additional mass loss is an unlikely solution.

Lower mass stars with convective cores are not well fit by standard stellar evolution. Again, additional mixing is a promising answer. Several of these binaries seem to be pre-main sequence; this will allow some interesting tests of depletion of light nuclei and the mixing processes.

We find two serious challenges: (1) disentangling conflicting solutions of the relatively subtle discrepancies, and (2) controlling shifts in the observational “target areas” due to systematic errors, which seem to be larger than the statistical errors. Improved determinations of effective temperature, and of heavy element abundances (e.g., $[\text{Fe}/\text{H}]$), would greatly improve these tests.

CHAPTER 3

STELLAR HYDRODYNAMICS IN RADIATIVE REGIONS

3.1 Introduction

The nature of mixing in stars is a perpetual problem in stellar evolution. The standard mixing length theory of convection (Kippenhahn & Weigert, 1990) is remarkably effective for a one-dimensional, ensemble average of convective energy transport. However, observations seem to indicate that more mixing occurs in stars than is expected. For example, measurements of the apsidal motion of binary star orbits give a measure of the density structure of the components. Comparisons with mixing-length models indicate that real stars have larger convective cores than predicted by theory (Young, Mamajek, Arnett, & Liebert, 2001). Models of double-lined, eclipsing binaries with well determined masses and radii also require additional mixing to match observations (Young, Mamajek, Arnett, & Liebert, 2001; Pols et al., 1997b; Ribas et al., 2000). Determinations of young cluster ages independent of isochrone fits to the main sequence using the lithium depletion edge in brown dwarfs give substantially older ages which can also be reconciled by increased mixing (Stauffer et al., 1998).

Parameterized descriptions of mixing can tell us a great deal, but only in well populated regions of the H-R diagram where high-quality observational constraints are numerous. Light element depletion on the pre-main sequence (pre-MS) and convective core sizes, and thus lifetimes and luminosities, on the main sequence are affected (Piau & Turck-Chièze, 2002; Young, Mamajek, Arnett, & Liebert, 2001). For low and intermediate mass stars s-process nucleosynthesis on

the AGB, ISM enrichment, and white dwarf sizes and compositions are strongly influenced (Wallerstein & Knapp, 1998). In massive stars the size of the heavy element core and mixing in the high-temperature burning shells may substantially impact supernova nucleosynthesis and explosion mechanisms (BA98,AA00).

It has long been known (Spiegel, 1972) that mixing-length theory, by approximating derivatives poorly, must have problems at the interface between convective and nonconvective regions, posing an embarrassment for stellar evolution. Saslaw & Schwarzschild (1965) discussed the problem using laminar hydrodynamic theory in the convection zone, which ignores the strongly turbulent nature of stellar convection. Shaviv & Salpeter (1973) examined the ballistics of a convective blob; this particle approach does not impose continuity (mass conservation) on the dynamics. These two approaches are well represented in the extensive literature on the subject. Most modern stellar evolution codes seem to use either mixing length theory (Kippenhahn & Weigert, 1990; Clayton, 1983) or the full spectrum theory (Canuto & Mazzitelli, 1991) in the turbulent regions and assume other regions are static.

We note that the correct equations for describing stellar *nonconvective* regions are hydrodynamic, not static (Cox, 1980). If symmetry is broken, as by perturbations from a convective region, these motions are also three-dimensional. We examine the hydrodynamics induced in radiative regions, due to the fact that the convective/nonconvective interface is neither static nor spherical. The problem becomes one of driven, non-radial, non-adiabatic pulsations (Hansen & Kawaler, 1994). Numerical simulations (especially Bazàn & Arnett (1998) BA98, and Asida & Arnett (2000) AA00) lead us to the possibility that large wavelength modes, specifically plumes, are dominant in the coupling at this interface. We suggest how this coupling works, and how it necessarily implies a slow mixing into the

radiative region. We show how a simple version of this picture may be implemented in a stellar evolutionary code. Our theory is complementary to theories of the turbulent convective region, such as the standard mixing length theory (Kippenhahn & Weigert, 1990) or the full spectrum theory (Canuto & Mazzitelli, 1991).

In this paper we focus on the simplest case, and provide a lower limit on “extra” mixing — which is above that obtained with conventional stellar evolution theory. We argue that our theory is a necessary part of a complete solution, but believe that other aspects of hydrodynamics (such as rotation (Maeder & Meynet, 1989; Kumar & Quataert, 1997; Schatzman, 1999; Charbonnel & Talon, 1999; Pinsonneault et al., 2002; Talon, Kumar, & Zahn, 2002)) are also important, and may be synthesized into a more complete theory. We present several tests of our approach by comparison with observations.

3.2 Implications of Numerical Simulations

We begin by examining multidimensional numerical simulations, which are non-local and fully nonlinear. We have been most influenced by BA98 and AA00, but have also studied Porter et al. (2001) and Brummell, Clune, & Toomre (2002) in some detail. These simulations give us a glimpse of the hydrodynamic behavior of the interface of the convection zone, from which we can begin to construct a theoretical picture. These simulations are not entirely accurate descriptions of the star due to the limited range of resolution. Turbulent structure is expected to span all size scales down to the local diffusion scale, which is much smaller than the resolution element of any simulation which captures the large scale structure. Further impact of sub-resolution scale physics is discussed in Canuto (2000). The maximum Reynolds number of the simulations (in 3D) is $R \sim 10^8$, whereas in

stars R may be as high as 10^{14} . Turbulence may become completely chaotic at $R \gg R_0$, a regime which is not amenable to exploration numerically or experimentally (Dimotakis, 2001). While microscopic mixing is not well treated because it is dominated by processes with length scales smaller than the resolution of the simulations, energy and bulk transport are dominated by processes with large length scales, and may be modeled better. It is necessary to develop a theoretical understanding of the processes involved, rather than relying entirely upon numerical results.

These simulations presented us with two puzzles:

- Large density perturbations appear at the interface between convective and nonconvective regions (BA98).
- Slow vortex motion appears outside the formally convective region, giving a slow mixing (AA00).

How can this be understood?

3.2.1 Convective forcing

Inside a stellar convection zone, the velocity field has significant vorticity; outside the velocity is assumed negligible. Hydrodynamically, this interface corresponds to a *surface of separation* between rotational ($\nabla \times \mathbf{v} \neq 0$) and irrotational flow ($\nabla \times \mathbf{v} = 0$) (Landau & Lifshitz, 1959), see §34.

To be specific we consider the outer edge of a convective oxygen burning shell (BA98,AA00). This is a simple case in that it avoids the added complexity of a photospheric boundary condition (as opposed to simulations of the solar convection zone, for example Christensen-Dalsgaard (2002); Freytag, Ludwig, & Stefan (1996)) and can be evolved numerically on the evolutionary timescale, since the nuclear and sound-travel timescales are commensurate. The convection does

work on the interface between laminar and turbulent regions, with a total power (luminosity)

$$L_{conv} = A\delta P v = APv_s(\delta P/P)(v/v_s), \quad (3.1)$$

where $A = 4\pi r^2$ is the spherical area, v_s is the sound speed, v the transport velocity by convection, and δP the pressure fluctuation. Inserting numerical values from the simulations we find

$$(\delta P/P)(v/v_s) = 10^{-4} \quad (3.2)$$

and since $(\delta P/P) \simeq (v/v_s)$, we have a Mach number of

$$(v/v_s) = 10^{-2}. \quad (3.3)$$

This estimate uses mathematical relations in the spirit of mixing length theory, and gives an average velocity. Examination of the numerical results shows that the actual velocity is concentrated in plumes which occupy a smaller cross-sectional area, but have higher speeds (Hurlburt, Toomre, & Massaguer, 1996). There are significant density perturbations at the boundary between laminar and turbulent flow. This is sufficient to drive a nontrivial acoustic flux and cause significant non-radial density perturbations $\delta\rho/\rho$ of a few percent (see BA98, figure 3 and figure 7 and AA00, figure 8).

For earlier and less vigorous burning stages, the Mach number is smaller, so that neglect of acoustic flux may not be so atrocious. However, these stages are also longer, so that the accumulated effect of the waves may still be significant. These enhanced density variations at the interface are a robust feature in simulations; three-dimensional calculations of the solar convective zone and red giant stars have displayed similar pumping of gravity waves (Brummell, Clune, & Toomre, 2002; Porter et al., 2001).

In the stellar interior, convective luminosity may be estimated without any detailed theory of convection. The hydrodynamic motion is nearly adiabatic, so the radiative flux is close to that for radiative diffusion for an adiabatic temperature gradient. The total luminosity is determined from the conservation of energy, so that the convective luminosity is the difference $L_{conv} = L_{total} - L_{rad}$ (Kippenhahn & Weigert, 1990). At the edge of the convective region, we identify this with the energy flux available to drive waves by the deceleration of plumes. The precise fraction of the luminosity that goes into driving depends upon the detailed physics of the convective interface (Goldreich, Murray, & Kumar, 1994); our simulations suggest the kinetic part is comparable to the thermal part of the convective flux (BA98, figure 3).

3.2.2 Hydrodynamic response

What does this do to the radiative region? The natural modes for nearly laminar flow are irrotational, and in general will be incommensurate with the rotational flows of the convective zone. There will be a mismatch at the boundary, so that the boundary matter will be driven, exciting waves. Because the motion of the plumes is generally subsonic, the coupling will be biased toward g-modes, which have longer periods. Asida & Arnett (2000) find a combination of waves, having both g-mode and p-mode character (Cowling, 1941). The waves exhibit an exponential fall-off moving away from the interface into the radiative region, but also significant compressible effects (density fluctuations). See AA00, figures 8, 11-14 for detail.

Figure 3.1 shows a schematic of the behavior of the interface of the convective region. Three dimensional simulations of convection also show up-down asymmetry (Porter et al., 2001; Brummell, Clune, & Toomre, 2002). For the solar convective envelope, with driving caused by the entropy decrease from radia-

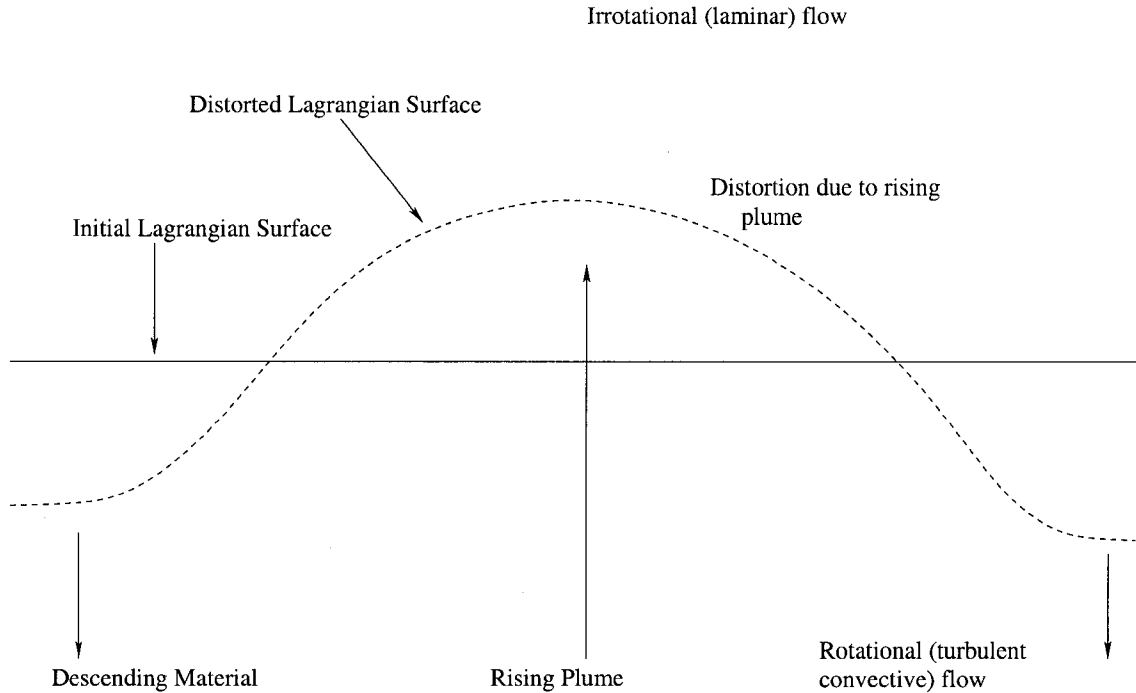


Figure 3.1: Lagrangian (co-moving) fluid surfaces at boundary between convectively stable and unstable regions. The distortion due to a rising plume and a downdraft are shown. The original spherical boundary is distorted as interface material bobs up and down, generating gravity waves. Contrary to the usual assumption in stellar evolution simulations, the convective boundary is neither spherical nor static. Dissipation of the gravity waves actually causes slow circulation in the nominally laminar region outside the convective zone.

tive loss near the photosphere, plumes tend to move downward from the photospheric surface. For oxygen shell burning, plumes tend to move upward from the burning shell, in which nuclear energy release causes an entropy increase. Neutrino cooling tends to cause plumes that are directed downward (BA98).

As a plume encounters a boundary, it pushes the over(under)lying material, distorting the boundary. Part of the plume's kinetic energy goes into raising the potential energy of the displaced region. When the plume stalls, this potential

energy is converted into motion in the opposite direction of the plume's velocity. Gravity waves are generated. Contrary to the usual assumption in stellar simulations, the convective boundary is neither spherical nor static. This resolves a paradox of mixing length theory, in which the convective velocity has a discontinuity at the convective boundary, going from a finite value to zero.

The surface of separation is a nonspherical comoving (Lagrangian) boundary, which moves relative to the spherical (Eulerian) boundaries of a stellar evolution code. The spherical shells do move on average with the matter, in that they may contain a fixed amount of mass, but it need not be the same matter. While the interface moves across a spherical shell, it may later move back. Motion does not necessarily give mixing. Note that this goes beyond the usual notion of spherical Lagrangian shells in a stellar evolutionary code; hydrodynamic motion is faster than slow secular evolution, so that the spherical shells seem relatively fixed in space (that is, Eulerian); see Cox (1980).

3.2.3 g-modes

To the extent that the time scale for heating and cooling the radiative region is longer than that for hydrodynamic motion, Kelvin's circulation theorem holds (Landau & Lifshitz, 1959). Further, if the hydrodynamic motion is slow (strongly subsonic), it is described by a velocity potential, $\mathbf{v} = \nabla\phi$, where ϕ satisfies Laplace's equation $\nabla^2\phi = 0$. If we take a Cartesian coordinate system (x,y,z) with z positive along the radial direction \mathbf{r} , $z = 0$ at the interface between convection and nonconvection, and assume the waveform transverse to z is periodic, then

$$\phi = f(z)e^{i(k_x x + k_y y - \omega t)}, \quad (3.4)$$

so

$$\nabla^2\phi = \phi(-(k_x^2 + k_y^2) + \frac{1}{f}\frac{\partial^2 f}{\partial z^2}) = 0, \quad (3.5)$$

giving $f = e^{\pm kz}$, where k is the transverse wave number, defined by $k^2 = k_x^2 + k_y^2$. The sign choice comes from the boundary condition, so that the function decreases exponentially away from the boundary $z = 0$. Waves of longer wavelength (small k) extend farther from the boundary. While this is a useful guide, the actual waves (AA00) are not strictly incompressible ($\nabla \cdot \mathbf{v} = 0$; density variations occur, and are important for damping the waves).

We relate the wave number to the frequency by equating the acceleration in the z direction to the corresponding force per unit mass. For an incompressible liquid it gives $\omega^2 = kg$, while the compressible case results in the Brunt-Väisälä frequency

$$N^2 = \frac{g\delta}{H_P}(\nabla_{ad} - \nabla + \frac{\varphi}{\delta}\nabla_{\mu}), \quad (3.6)$$

from Kippenhahn & Weigert (1990), eq. 6.18, where the symbols have their usual meaning, or Hansen & Kawaler (1994), eq. 5.35 and 10.92. Our system is finite, so only a discrete spectrum of waves is possible. Notice that the quantity in parenthesis is the Ledoux condition for convective instability, and has implications for regions with compositional gradients, which we do not pursue here.

The longest wavelengths penetrate further, and will be most effective for mixing. The maximum wavelength generated will depend upon the details of the convective driving.

With a complete theory of turbulent convection we could simply determine a transfer function for the excitation of waves in the radiative region (Goldreich, Murray, & Kumar, 1994). Mixing length theory is the simplest; it maintains that only one dominant wavelength need be considered — the mixing length. The Canuto-Mazzitelli theory gives a broader spectrum of modes but they peak in the same place (see (Canuto & Mazzitelli, 1991), Figure 1). For simplicity we take the appropriate wavelength to be equal to the length scale we would derive from

the size of the plumes seen in simulations.

3.2.4 Dissipation of waves

The driving of the waves must be balanced by their dissipation for a steady state to result. In the stellar plasma this will usually be due to thermal diffusion of radiation. Such dissipation will be faster at the shorter wavelengths; for a given amplitude they have the largest gradients. For a given wave, we could integrate the wave equation (Cox, 1980) for a precise result. The precision would be illusory in that the range of relevant wavelengths would depend upon our ignorance of the properties of the convective driving. Instead we give a simpler example to illustrate the physics and make a preliminary estimate of the importance of the process.

The canonical picture of damping of gravity waves is by viscosity (Landau & Lifshitz (1959), §25). Using the viscosity of a plasma in the absence of magnetic fields (Spitzer (1962), §5.5), we find a damping time of many gigayears for stellar conditions, so this is not the relevant damping. The compressible effects give rise to temperature fluctuations; this gives a pressure perturbation which resists the wave motion, analogous to damping of stellar pulsations (Cox, 1980). Following Kumar & Quataert (1997), the local radiative dissipation of gravity waves is

$$\gamma \approx \frac{2F_r k_r^2 H_T}{5P}, \quad (3.7)$$

where F_r is the radiative flux at radius r from the center of the star, $k_r \approx N[l(l+1)]^{1/2}/[r\omega]$ is the wave's radial wave number for frequency ω , P is the pressure, and H_T is the temperature scale height.

3.2.5 Circulation and mixing

A difficult step is the connection between the multidimensional flow and the microscopic mixing. We argue that dissipation drives circulation, which is likely to

be turbulent. For the purposes of a stellar evolution code we identify this with a diffusive velocity $u_k(\Delta r)$, even though the physical identity is not exact. The characteristic scale is l_{turb} , and is determined from simulations.

As we saw above, the coupling of convective plumes with the region of laminar flow outside the convective region generates significant density anisotropies and waves at the boundary. These low Mach number waves can be described approximately as potential flow which we assume to be dissipated over a distance determined by the hydrodynamics. This damping is an entropy-generating process, causing vorticity which allows for microscopic mixing of the material and slow circulation of the mixed material well beyond the convectively neutral boundary. Qualitatively, this is like breaking of wave crests on a sea.

For didactic purposes we will derive the generation of vorticity by damping of the potential flow in a simple plane parallel case. Following Landau & Lifshitz (1959), §9,

$$\frac{d\mathbf{v}}{dt} + \mathbf{v} \cdot \nabla \mathbf{v} = \nabla \mathbf{w} - T \nabla S \quad (3.8)$$

Discarding $\mathbf{v} \cdot \nabla \mathbf{v}$ as small,

$$\nabla \times \frac{d\mathbf{v}}{dt} = \nabla \times \nabla \mathbf{w} - \nabla \times (T \nabla S) \quad (3.9)$$

The term $\nabla \times \nabla \mathbf{w} \rightarrow 0$, giving

$$\frac{d\nabla \times \mathbf{v}}{dt} = -T(\nabla \times \nabla S) + \nabla S \times \nabla T \quad (3.10)$$

Discarding $-T(\nabla \times \nabla S) \rightarrow 0$ gives the final form for the generation of vorticity,

$$\frac{d\nabla \times \mathbf{v}}{dt} = \nabla S \times \nabla T \quad (3.11)$$

In a perfectly spherically symmetric star $\nabla S \times \nabla T$ would go to zero in the laminar regions. When we introduce perturbations from the damping of the waves,

however, we gain a cross term which makes the time derivative of the vorticity non-zero. We employ a standard style of perturbation analysis *a la* Landau & Lifshitz (1959) or Hansen & Kawaler (1994), discarding terms of higher than first order, and examine the contribution from

$$\frac{d\nabla \times \mathbf{v}}{dt} = \nabla S' \times \nabla T_0 \quad (3.12)$$

where X' denotes a perturbation and X_0 denotes the unperturbed value of a variable. Henceforth we will change notation to $X = X_0$ for simplicity. In the simplified plane parallel case and ignoring unnecessary constants,

$$\frac{d\nabla \times \mathbf{v}}{dt} = \frac{\partial S'}{\partial x} \times \frac{\partial T}{\partial z} \quad (3.13)$$

From the standard equations of stellar structure (Kippenhahn & Weigert, 1990) we take

$$\frac{\partial T_0}{\partial z} = -\frac{3\kappa\rho L}{16\pi a c r^2 T^3} \hat{z} \quad (3.14)$$

and from thermodynamics (Reif, 1965)

$$\frac{\partial S'}{\partial x} = \frac{1}{T+T'} (4aT^3 \frac{\partial T'}{\partial x} + \frac{P}{\rho^2} \frac{\partial \rho'}{\partial x}) \hat{x} \quad (3.15)$$

We will assume an adiabatic case, such that $\rho^{\gamma-1}T = \text{const}$ and

$$\frac{\partial \rho'}{\partial x} = \frac{1}{\gamma-1} T'^{(\frac{2-\gamma}{\gamma-1})} \frac{\partial T'}{\partial x} \quad (3.16)$$

After some algebraic manipulation,

$$\begin{aligned} \frac{d\nabla \times \mathbf{v}}{dt} &= \frac{\partial S'}{\partial x} \times \frac{\partial T}{\partial z} = \\ &= -\frac{3\kappa\rho L}{16\pi a c r^2 T^3} \frac{1}{T+T'} (4a c T^3 + \frac{1}{\gamma-1} T'^{(\frac{2-\gamma}{\gamma-1})} \frac{P}{\rho^2}) \frac{\partial T'}{\partial x} \end{aligned} \quad (3.17)$$

Integrating over dt with the damping described in §2.4 and a reasonable approximation to the wavefunction gives an estimate of the vorticity. Further using the curl theorem and integrating the vorticity over the path of a fluid element gives an estimate of the diffusion velocity at a given radius.

3.3 Implementation in stellar evolution

To implement this mixing in TYCHO, we treat the mixing as a diffusion process with a diffusion coefficient

$$D = \frac{u_k(\Delta r)l_{turb}}{3} \quad (3.18)$$

constructed from the terms discussed in the previous section. This treatment leaves one free parameter, $\frac{l_{turb}}{H_p}$, the dominant scale length of the turbulence near impact of the plumes with the boundary. This quantity is directly related to the dominant wavelength of the gravity waves driving the mixing. There is power at all scales in the convective region. The power is flat or slightly rising from the largest scales to the value we choose for our treatment and then follows a power law consistent with Kolmogorov turbulence down to the smallest resolved scales (Porter et al., 2001). We estimate $\frac{l_{turb}}{H_p} \sim 0.1 - 0.15$ using three-dimensional numerical simulations (Porter et al., 2001). Traditionally, model fits have been improved by introducing free parameters such as the alpha prescription for overshooting (Maeder & Meynet, 1989). Clearly, we should not have infinite freedom to introduce parameters. While the parameterized approach has yielded extremely important results in terms of understanding the extent of the extra mixing observed in stars, it gives us little insight into the underlying physics and has limited predictive power. By fixing this quantity using results from multi-dimensional hydro calculations, we are attempting to construct a physical picture of the mixing in the radiative region with minimal variability in parameters. We prefer to constrain our theory by terrestrial simulations and experiment rather than astronomical observation. This should increase the predictive power of the theory. Additional simulations are needed to explore the behavior of this scaling in a wider variety of conditions appropriate to stellar astrophysics. Cases where the pressure scale height is divergent or much larger than the convective scale, for example in the

small convective core of the ZAMS sun are of particular interest.

A desirable property falls naturally out of this treatment. Three-dimensional hydro simulations indicate that boundaries with shallow changes in the adiabatic gradient should be able to mix over wider ranges in radii (Brummell, Clune, & Toomre, 2002). This should result in more mixing for higher mass stars, and more mixing in convective cores than in envelopes, which seems to be supported by parametrized overshooting in previous work (Pols et al., 1998; Maeder & Meynet, 1989). This treatment preserves this behavior, since the region over which the gravity waves are dissipated is larger in the more isentropic environment of core convection. Also, the higher convective velocities in H burning cores than envelopes result in a higher gravity wave flux and larger mixing region, and similarly more mixing in He cores than H. The extra mixing occurs over a significant fraction of a pressure scale height in core convection (compare with values of $0.4\text{--}0.6H_p$ in parametrized overshooting) and $< 0.05\text{--}0.1H_p$ for envelope convection.

3.4 The Stellar Evolution Code TYCHO

All stellar evolution calculations presented below were performed using the TYCHO 1-D stellar evolution code discussed by Young, Mamajek, Arnett, & Liebert (2001) but with substantial improvements in several areas. The equation of state (EOS) has been updated to use a modified version of the Timmes & Swesty (2000) tabular electron-positron EOS. It has been further modified to have appropriate coulomb corrections for the weak screening case and a Debye interpolation for strongly coupled plasmas. This agrees to within 2% (and usually to less than 0.1%) with the EOS tested empirically by the OPAL project's high energy density laser experiments (Iglesias & Rogers, 1996). There are significant deviations from our EOS only where the OPAL models do not account for contributions from

electron degeneracy pressure. The size of the reaction network was increased to 175 nuclei, and is well populated all the way up to the iron peak. The low temperature opacities have been completely revised to use tables from Alexander & Ferguson (1994), and are interpolated to serve for any metallicity between zero and five times solar. The mass loss at low T_{eff} has been updated to use the modified Reimers formulation presented in Blöcker (1995), which results in much higher mass loss rates on the AGB. Alternatively, low temperature mass loss may be switched off entirely to examine purely episodic mass loss on the AGB. An ADI operator split has been implemented in the mixing algorithm so that nuclear reaction calculations will be informed about the change in composition, and the thermodynamic variables used in the EOS and mixing routines will properly take into account energy input by burning and neutrino cooling. The mixing is also now time-limited rather than instantaneous. Additional refinements improving the numerical convergence of the code and its convergence at small timesteps have also been incorporated. Experiments have been performed which include heavy element diffusion, and give unsurprising results, consistent with solar models from Bahcall, Pinsonneault, & Basu (2001). The version of the code used in this study (TYCHO 6.11) does not incorporate heavy element diffusion, as such an examination is beyond the scope of the current discussion. It is also useful to separate the effect of settling out from the phenomenon being examined. The timescale for settling is sufficiently long that for ages much less than that of the Sun, the effect should be negligible. The two quantitative cases presented herein both have ages less than 10^9 yr, and should not be affected.

3.5 Comparisons with Previous Work

Remedies to the problem of mixing have until recently largely been phenomenological. The mixing beyond the standard model is parametrized and labeled as “overshooting” in convective cores and “undershooting” in convective envelopes, or more generically as overshooting in both cases. The term has been taken by various groups to encompass both penetrative convection beyond the formal boundary of convective stability and slow compositional mixing. The most common overshooting prescription is “alpha-overshoot”, where compositional mixing is arbitrarily extended some fraction of a pressure scale height beyond the boundary of the formally convective region (Maeder & Meynet, 1989). More recently, Pols et al. (1998) have devised a parameterization based upon the superadiabatic excess of the boundary, which has the advantage of being tied to the structure of the star. Parameter fitting of this sort is valuable in constraining the extent of the extra mixing by astronomical observation, but gives us little insight into the physical nature of the process. Overshooting based on rotational mixing has also been proposed. It has been particularly useful in solving the problem of the lithium gap in F stars. The blue side of the dip is reasonably well modelled by rotation-driven meridional circulation (Deliyannis et al., 1998; Boesgaard & King, 2002; Piau & Turck-Chièze, 2002; Pinsonneault et al., 2002). Recent work describing angular momentum transport by gravity waves has shown considerable success in matching the red side of the dip (Charbonnel & Talon, 1999; Talon, Kumar, & Zahn, 2002). Rotation looks likely to be an important contributor to the solution of the mixing problem, but is probably not the whole of the story (Maeder & Meynet, 1989; Pinsonneault et al., 2002). It is our intention to avoid the use of the term “overshooting” entirely so as to be free of its associated connotations.

In this paper we discuss non-rotational hydrodynamic contributions to the mixing from gravity waves generated at the surface of separation between the convective and laminar regions of a star. García López & Spruit (1991) attempt to assess the contribution to mixing of gravity waves at the convective boundary in the particular context of lithium depletion in F type stars in young clusters. They conclude that the mechanism produces the proper mixing behavior, but requires a gravity wave flux a factor of fifteen larger than given by simple estimates. This problem is not insurmountable. They themselves point out that the efficiency of converting kinetic energy of convective fluid elements increases significantly if the downflows driving the waves are concentrated into narrow plumes. Simulations show the filling factors of these plumes are a few percent (Porter et al., 2001; Brummell, Clune, & Toomre, 2002). In addition, Canuto (2002) argues that turbulent mixing in a stellar context is likely to persist for a larger range of conditions. In García López & Spruit (1991), the extent of mixing was limited by comparing an unperturbed stellar model to a laminar stability model. The critical Richardson number $Ri(cr)$ for which turbulence may persist once established is a factor of four larger than $Ri^l(cr)$ for the breakdown of an established laminar flow. In addition, radiative losses weaken stable stratification and the gravity waves themselves act as an energy source for turbulence. Thus $Ri^{tot}(cr)$ may be substantially larger than $Ri^l(cr)$. This allows the spatial extent of turbulence and associated mixing for a given gravity wave flux to be larger by about the same factor (Canuto, 2002). A combination of these effects could easily allow the gravity wave mechanism of García López & Spruit (1991) to account for the mixing in this case. By examining the dissipation from an energetic standpoint and using a length scale calibrated by fully non-linear hydro codes with energy sources and sinks, we hope to avoid this particular difficulty. The García López & Spruit

(1991) treatment has certain advantages. Gravity wave spectra may be dominated by frequencies which are weakly damped or resonant with characteristic length scales in the star. We do not initially take this into account. Such a treatment is necessary for treating angular momentum transport by gravity waves (Charbonnel & Talon, 1999; Talon, Kumar, & Zahn, 2002), and is likely to be important in the non-rotational context as well.

3.6 Tests of the Theory

In this section we present comparisons of models produced by the TYCHO code incorporating the new convective boundary conditions with observations in three different evolutionary regimes. This theoretical description provides useful physical insight into envelope convection and light element nucleosynthesis, cluster ages and gross stellar properties including core convection, and complex convection and advanced nucleosynthesis in evolved stars. No parameter optimization was used to improve the fit of any models. Two solar models (one with element diffusion and one without) were also run as a control, and all surface observables (R, T_{eff}, L, X_i) are in acceptable agreement with Bahcall, Pinsonneault, & Basu (2001). Errors in the luminosity and $X(^4He)$ are consistent with the absence of helium and heavy element settling in the non-diffusion version of TYCHO. A detailed comparison with helioseismological constraints on the interior was not performed. However, the model is in qualitative agreement with suggestions that the extent of *penetrative* convection does not extend much beyond that predicted by conventional models, while compositional mixing must go significantly further (Bahcall, Pinsonneault, & Basu, 2001). The size of the penetrative convective envelope ($0.727R_{\odot}$, consistent with the no-diffusion model of Bahcall, Pinsonneault, & Basu (2001) and $0.712R_{\odot}$, consistent with the diffusion model),

is similar in TYCHO models with and without the extra mixing. The slow compositional mixing extends well beyond the standard convective zone ($\sim 5 \times 10^9$ cm) when the new theory is employed.

3.6.1 Li and Be in the Hyades and Pleiades

The burning of lithium and beryllium in pre-main sequence stars provides a sensitive probe of convective mixing. Lithium is burned at temperatures above 2.5×10^6 K, which can be reached at the base of convection zones in lower mass stars. A “lithium edge” where the abundance begins to decline from an approximately constant value is produced at low effective temperatures since the depth of convection increases with decreasing stellar mass. The location and steepness of this edge serves to test whether convection in stellar models reaches as deeply as in real stars. A second dip in the lithium abundance is seen in F stars ($T_{eff} \sim 6500 - 7000$ K), which requires additional physics, most likely rotation (Thorburn et al., 1993; Charbonnel & Talon, 1999; Piau & Turck-Chièze, 2002; Boesgaard & King, 2002; Pinsonneault et al., 2002; Talon, Kumar, & Zahn, 2002). García López & Spruit (1991) present a gravity wave-excited mixing treatment which is somewhat consistent with the observational data for the lithium gap. However, they do not extend the results down to the lithium edge, so a direct comparison with our work is difficult. Recent observations have provided similar data for beryllium, which burns at 3.5×10^6 K and thus provides an additional, related constraint. From a theoretical standpoint, Be depletions are as simple to estimate as those from Li. Unfortunately, the atomic transitions of beryllium are located just below the UV atmospheric cutoff, where ground-based observations of stars with T_{eff} much below 5500 K is difficult. More importantly, at low T_{eff} a line of magnesium begins to come in strongly almost on top of the beryllium line, rendering accurate equivalent width measurements problematic (Thorburn

et al., 1993; Piau & Turck-Chièze, 2002; Boesgaard & King, 2002). The location of the beryllium edge is therefore not known.

Figure 3.2 (top) shows calculated surface lithium abundances for stars of Hyades composition ($[\text{Fe}/\text{H}] = +0.13 \pm 0.02$). Values are taken at the age of the best fit isochrone for the cluster determined using photometric data from de Bruijne et al. (2001) and compared with the observed points from Boesgaard & King (2002). The age of the cluster in our models is between 650 and 700 Myr, consistent with the age from conventional overshooting models in de Bruijne et al. (2001). In our simulations, the drop-off in lithium with T_{eff} is much too shallow without the extra slow mixing. Implementing the mixing brings our theoretical values in line with observations. The lithium dip in F stars is not reproduced, which is unsurprising as rotation is not included in these models. We find rather too much depletion of lithium in the models in the range between the F dip and the depletion edge. We suspect this, too, is a hallmark of rotational mixing, as in some regimes mixing appears to actually be *damped* by rotation (Piau & Turck-Chièze, 2002; Kippenhahn & Weigert, 1990; Chandrasekhar, S., 1961). A full calculation of the wave spectrum should also improve the calculation in this regime. The bottom panel of Figure 3.2 shows the same data for beryllium. We find no significant depletion. This is consistent with observations to the lowest observed T_{eff} , and indicates that our mixing is not excessive. Interestingly, we do not see any depletion of beryllium at lower effective temperatures. At the age of the Hyades the lowest mass stars have not finished contracting onto the main sequence and have not established the deep convective envelopes necessary to deplete the beryllium. Space-based observations and data on older clusters could aid in detecting beryllium depletion. The coincidence in effective temperature between the Li and Be dips indicates that this is a sensitive test of the depth of the convective

zone. The dip itself may serve as a test of rotation, while the depletion edge tests non-rotational mixing.

Simultaneously being able to reproduce Li depletions for clusters of different ages is problematic for many theories of mixing (Piau & Turck-Chièze, 2002). In order to test that our description gives a reasonable time dependence for Li depletion, we modeled the Li edge in the Pleiades. Figure 3.3 shows the observed points from Soderblom et al. (1993) and models with the additional mixing. Our models were for our best fit turn-off age of 120 Myr (see Section 7.2). The models produce somewhat too much depletion at the lowest T_{eff} , but overall the predicted depletion matches the observations well. The models do not include molecular hydrogen contributions to the EOS, which becomes significant at the masses corresponding to the lowest effective temperatures. More work is required to sort out EOS and opacity effects from the mixing algorithm in this regime.

3.6.2 Comparison With Li Depletion Ages

The age of the Pleiades has variously been quoted as 75 to 150 Myr, with most studies using a value between 75 – 100 Myr. Recent determinations of the age using the lithium depletion edge in brown dwarfs place the age at 125 Myr (Stauffer et al., 1998). Similar uncertainties exist for other young clusters. Li depletion ages have been determined for two other clusters, α Per and IC 2391, with ages of 90 ± 10 and 53 ± 5 Myr, respectively (Stauffer et al., 1999; Barrado y Navascués, Stauffer, & Patten, 1999). Both ages are approximately 50% longer than those derived from conventional main sequence fitting. Without an independent calibration, it is equally possible that the Li depletion ages are wrong and turnoff ages are correct. The depletion ages are, however, consistent with models with parametrized overshooting calibrated by other methods. In the absence of further

observational constraints we will take the depletion ages to be a reliable measure. We determine the age of the clusters by fitting the main sequence turnoff with the extra mixing included.

Models were run for masses from 3.0 to $6.0 M_{\odot}$ in increments of $0.1 M_{\odot}$. The models were run at solar metallicity, which is within the error bars for the observations (Boesgaard & Friel, 1990; Randich et al., 2001). The L and T_{eff} conversions from observational data are taken from Mamajek (2002). Figure 3.4 shows our isochrones for the Pleiades (top), α Persei (center), and IC 2391 (bottom) at 120, 75, and 55 Myr, along with observed values corrected for differential reddening across the clusters. The error bars on the observations are sufficiently large that further refinement of the age was not attempted. The turnoff ages with the extra mixing are 120 Myr for the Pleiades, 75 Myr for α Per, and 55 Myr for IC 2391, consistent with the ages determined from lithium depletion in brown dwarfs.

One additional constraint is also reproduced. There is one white dwarf member of the Pleiades with a mass of $\sim 1 M_{\odot}$ (Wegner et al., 1991). Our models produce a white dwarf progenitor of $\sim 1 M_{\odot}$ at the age of the cluster from an initial mass of $\sim 5.5 M_{\odot}$.

3.6.3 Carbon Stars

The term “carbon star” is variously used to describe a menagerie of objects with surface abundances of carbon enhanced relative to oxygen. The group includes evolved stars on the AGB, subsets of white dwarfs and Wolf-Rayets, and cool dwarfs. Only the first category will be discussed here. The evolved stars further may show enhancements in s-process elements and lithium. Observations of ^{99}Tc , which has a half life of 2×10^5 years, indicates that the products of *in situ* nuclear processing are being mixed to the surface. The s-process elements and enhancements of lithium and ^{13}C require burning in a region enriched in

both protons and the products of triple α burning (Wallerstein & Knapp, 1998; Cameron & Fowler, 1971). This is difficult to reproduce with traditional stellar evolution codes, since the products of partial triple α burning are not in general mixed into hydrogen burning regions or further to the surface (Busso et al., 1999).

Making comparisons between models and observed carbon stars is difficult, as the class includes such a large variety of stars. The masses of carbon stars for low metallicity populations appear to range from ~ 0.8 to ~ 6 or $8 M_{\odot}$. Absolute bolometric magnitudes ranging from $M_{\text{bol}} = 0$ to -8 ($L/L_{\odot} \sim 10^2 - 10^5$), $T_{\text{eff}} \sim 2000 - 5000\text{K}$, and radii from approximately 2.4 - 2.7 AU (Wallerstein, 1973; Wallerstein & Knapp, 1998). Carbon stars appear to come in a range of metallicities, but the ratio of C to M stars increases greatly from the Galactic bulge to the Magellanic Clouds. There is a definite trend toward increasing efficiency of carbon star production at low metallicities (Blanco et al., 1980).

Implementing the present theoretical description of convective boundary conditions in TYCHO, we obtain carbon stars without further modification of the code. In light of the variety inherent in the class, this does not, by itself, demonstrate much about the effectiveness of the treatment, but when considered along with the success in a range of other regimes, is a promising sign. Exact isotope ratios are dependent not only on the boundary conditions, but also on the time dependent treatment of the compositional mixing inside the convective region itself. A subsequent paper will examine CNO and s-process nucleosynthesis for a range of masses and compositions.

We find that a $6 M_{\odot}$ star at $z = 0.001$ produces a star with surface carbon in excess of oxygen at the beginning of the thermal pulse AGB. The luminosity and T_{eff} are consistent with observed quantities for C-N stars. Carbon approaches but never exceeds oxygen for a solar metallicity model, as we might expect from the

observed bias toward low metallicity environments. Figure 3.5 shows the surface abundances of ${}^7\text{Li}$, ${}^{12}\text{C}$, ${}^{13}\text{C}$, ${}^{14}\text{N}$, and ${}^{16}\text{O}$ for the final 10^5 years of the model track. The star shows a pulse of elevated lithium and ${}^{13}\text{C}/{}^{12}\text{C}$ ratio at the beginning of the carbon star phase. This is consistent with the (again, wide range of) observed values for C-N stars, which show a bimodal distribution in carbon isotope ratios and enhanced lithium values. This may reflect an evolutionary trend (Wallerstein & Knapp, 1998).

3.7 Conclusions

We take a novel approach to the problem of mixing in stars by identifying phenomena which emerge in nonlocal, nonlinear, multi-dimensional hydro simulations. These simulations appear to successfully reproduce behavior on the large scale which transport most of the flux of energy and material. We then develop a theoretical description of this large scale behavior. This facilitates the transition from observed phenomenology to a predictive understanding which can be of use in the wider context of stellar evolution.

Several fundamental, if not surprising, results arise from implementing such a physical theory. First, the boundary between convectively stable and unstable regions cannot be treated as spherical or static, even in a one-dimensional approximation of the sort necessary for stellar evolution calculations. Hydrodynamic processes seen in multiple dimensions must be taken into account. Second, a careful treatment of the boundary conditions always results in extra mixing beyond the formal boundary. Third, a single physical process operates in both core and surface convective zones. Fourth, implementation of this theory in the stellar evolution code TYCHO contributes significantly to solving problems in several different regimes of stellar evolution. This is accomplished with only one pa-

parameter that does not fall directly out of the theoretical description, namely the dominant wavelength of the gravity waves driving the slow circulation in the radiative zone. Even this parameter is (a) a quantity with physical meaning, and (b) not allowed to vary, being fixed by data from numerical simulations. Finally, if this model continues to be as successful as it has thus far at explaining non-rotationally induced mixing, it will allow us to isolate the rotational contribution to stellar physics with a fair degree of confidence.

We reproduce the Li depletion edge in the Hyades and Pleiades. We find cluster ages for three young clusters consistent with ages determined from measurements of Li in brown dwarfs and for the Hyades as determined by main-sequence fitting with alpha-overshoot. The theory also generates reasonable carbon star models on the AGB. We expect that the physics and nucleosynthetic yields of supernovae and gamma ray bursts may be sensitive to the rotational properties of the star, core sizes, and final composition profiles at core collapse. It is essential to produce accurate initial models in order to generate realistic models of the explosion. This requires a physical, rather than simply phenomenological, characterization of the hydrodynamic mixing and rotation in stars. These factors also influence chemical enrichment from AGB stars and thermonuclear supernovae. These results may significantly improve our understanding of these processes, which impact issues as disparate as cluster ages, and thus timescales observed for disk evolution in pre-Main Sequence stars, to the nucleosynthetic history of the universe.

We stress that this result is merely a first step toward completely and predictively characterizing the mixing in stars. Numerical simulations have already illuminated physical processes which have changed our understanding of stellar astrophysics. Experiments with higher resolution, more complete physics, and

a wider variety of geometries and thermodynamic conditions appropriate to the range encountered in stars are vital, as they may well display yet more complex phenomena. Several other processes remain to be integrated into a complete picture of stellar mixing. This treatment does not take into account the effect of magnetic fields, which provide an upwardly biased buoyancy force and, when overlapping the convective boundary, coupling between stable and unstable fluids. Coupling between rotation and convective fluid motions must also be considered. Finally, changes to the nuclear burning and convection resulting from the ingestion of fresh fuel into a convective core or shell must be more carefully explored. We are confident, however, that the careful treatment of stellar hydrodynamics in both convective and radiative regions, plays an essential role in understanding the important problem of mixing in stars.

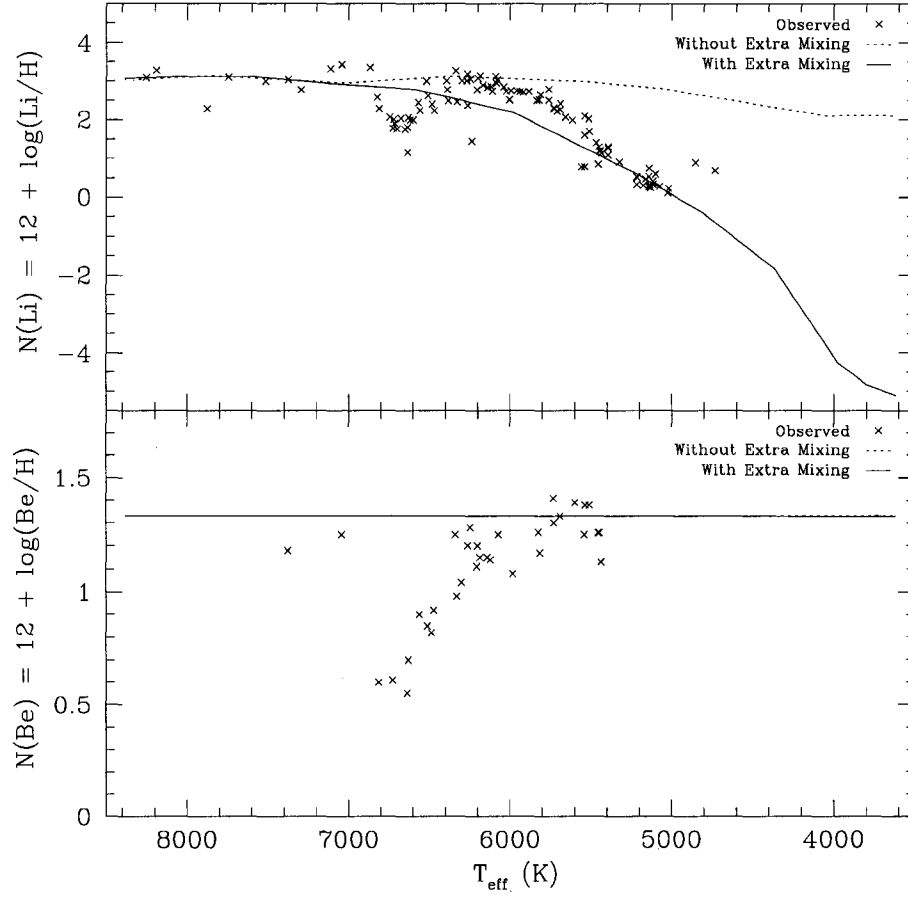


Figure 3.2: Observed Li (top) and Be (bottom) abundances from Thorburn et al. (1993); Boesgaard & King (2002) (crosses) along with calculated values with extra mixing (solid line) and without (dotted line). The model values with mixing follow the observed points closely at the depletion edge; those without under-predict the depletion significantly. We suspect that the dips at $T_{eff} \sim 6500 - 7000 K$ are due to rotation (Thorburn et al., 1993; Charbonnel & Talon, 1999; Piau & Turck-Chièze, 2002; Boesgaard & King, 2002; Talon, Kumar, & Zahn, 2002), indicating that we may be able to separate out effects of rotation and hydrodynamic mixing processes. Note that the dips appear at approximately the same effective temperature.

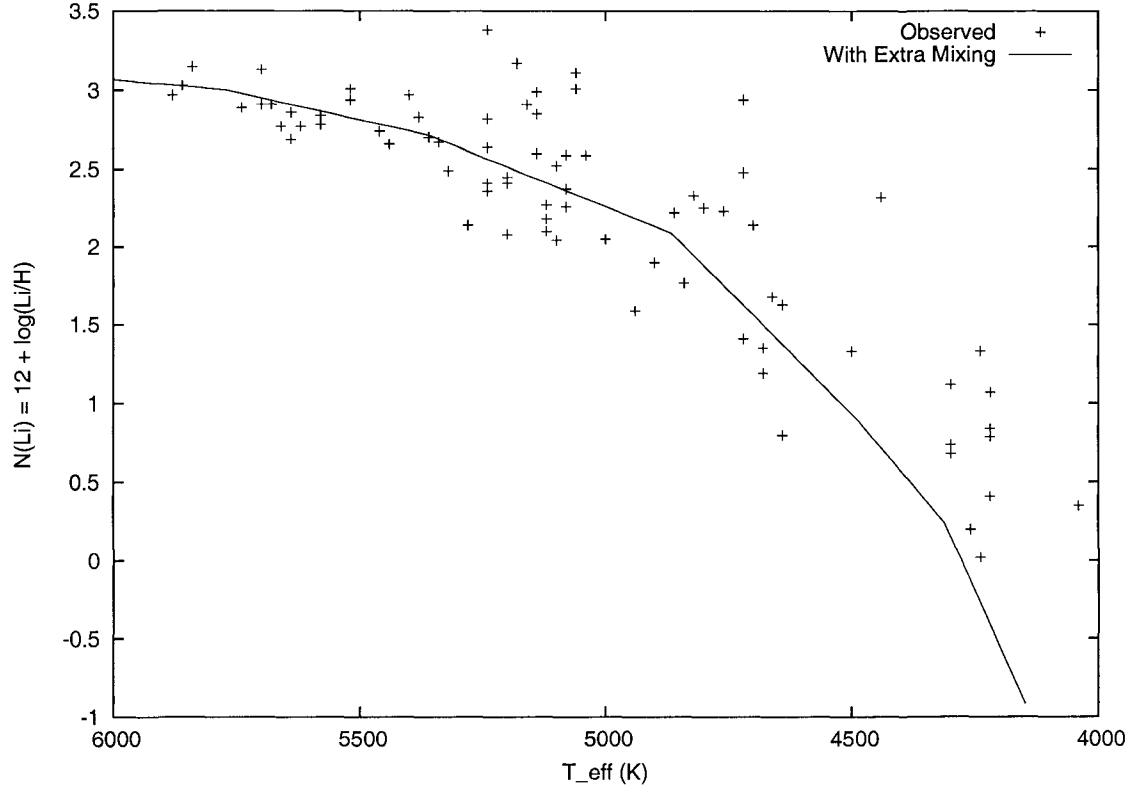


Figure 3.3: Observed Pleiades surface Li abundances (crosses) from Soderblom et al. (1993) plotted with models (solid line) for an age of 120 Myr. The predicted depletions match the observations well except at the lowest T_{eff} . This may be due to an inadequacy in the mixing model or inaccuracies in the low entropy equation of state.

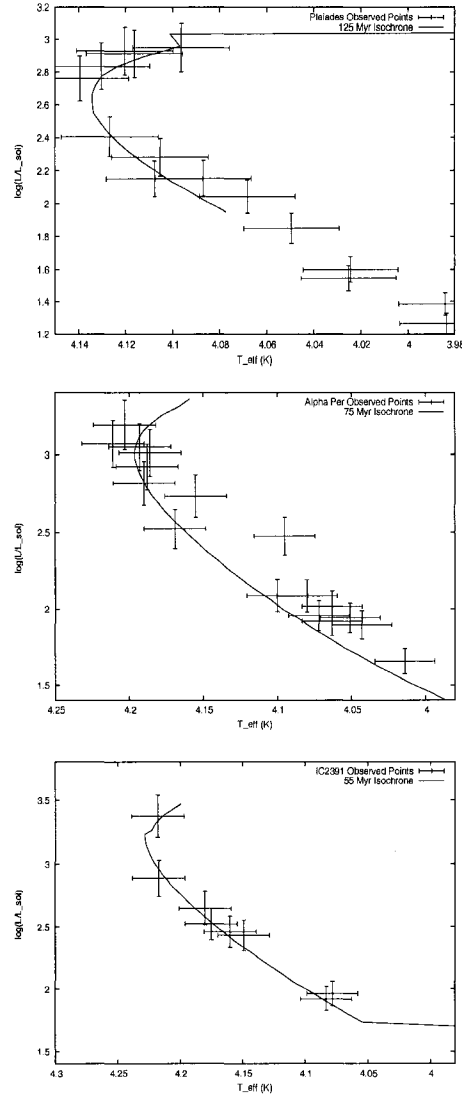


Figure 3.4: Observed luminosity and effective temperature for the turnoff stars of the Pleiades (top), α Persei (center), and IC 2391 (bottom) from Mamajek (2002). Crosses are observed stars and lines represent 120, 75, and 55 Myr isochrones from TYCHO, respectively. The error bars are representative, and do not properly take into account systematic errors. The isochrones are a reasonable fit at the lithium depletion ages of the clusters without recourse to parameter optimization.

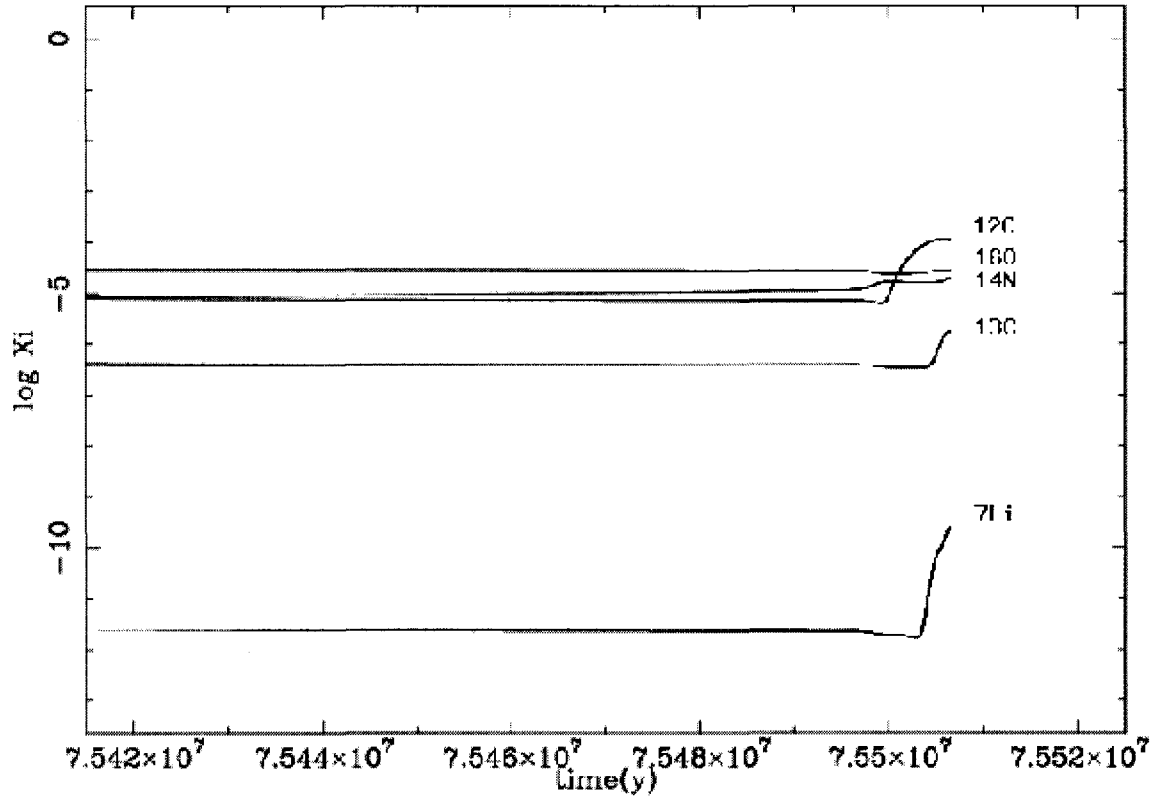


Figure 3.5: Surface abundances of ^7Li , ^{12}C , ^{13}C , ^{14}N , and ^{16}O for the final 10^5 years of a $z = 0.001$ $6 M_{\odot}$ model evolutionary track, corresponding to the beginning of the thermal pulse AGB. The carbon abundance has exceeded oxygen at the surface and is accompanied by a pulse of ^7Li and ^{13}C .

CHAPTER 4

OBSERVATIONAL TESTS AND PREDICTIVE STELLAR EVOLUTION II: NON-STANDARD MODELS

4.1 Introduction

Stellar evolution has become a successful tool for elucidating the processes at work in individual stars. New instrumentation and a wealth of new data has resulted in increased emphasis in astronomy on the evolution of galaxies over cosmic history. Obviously the stellar content of a galaxy plays a central role in its evolution. In order to understand this process, we require theoretical stellar evolution to be predictive, in the sense of being able to accurately describe the contribution of luminosity, kinetic energy, and nucleosynthetic products from a star of a specific initial mass and composition at any and all points in its life. This process must be able to be carried out self consistently for stars from the hydrogen burning limit to the highest possible masses, so that stellar outcomes can be reliably linked to an initial mass function (IMF). This is not possible with schemes which are adjusted to match astronomical observations. Without an underlying physical theory, the calibration cannot be reliably extrapolated to regimes without extensive and independent observational data. Also, multiple physical effects can contribute in opposite or orthogonal senses to the star's structure. As an example, determinations of metallicity of binaries are often made by fitting model tracks of varying composition to observed points and finding the best fit. However, an underestimate of the mixing tends to drive the models in the same direction as increased metallicity. So a model with incomplete mixing physics

and solar composition could be as good a formal fit to specific observations as a model with more complete physics and supersolar metallicity.

The two primary areas which strongly affect the evolution and have uncertain physics are mixing and mass loss. The evolution is also sensitive to the opacity of the stellar material, but the opacities used in evolution codes are largely uniform, utilizing the OPAL values of Iglesias & Rogers (1996) for high temperatures and Alexander & Ferguson (1994) for low temperatures. The observational errors in determining stellar compositions are the major limitation on further testing contribution of opacities to stellar models. Even the metallicity of the sun varies from $z=0.019$ (Grevesse & Sauval, 1998) to $z=0.015$ (Lodders, 2003), depending upon the precise physical assumptions and dimensionality of the codes being used to fit the measured line profiles. Most other test cases, such as most double-lined eclipsing binaries, *have no published metallicity determinations using high resolution spectroscopy*. Equations of state (EOS's) are not uniform across stellar evolution codes. While the effects of the EOS are perhaps more subtle, they can still be important, particularly for low mass stars and pre- and post-main sequence evolution.

In (Young, Mamajek, Arnett, & Liebert, 2001), we presented baseline results from stellar models calculated using only physics common to current widely used stellar evolution codes. These models were tested against a subset of double-lined eclipsing binaries (Andersen, 1991; Ribas et al., 2000; Latham et al., 1996; Lastennet & Valls-Gabaud, 2002; Hillenbrand & White, 2004). (Young et al., 2003) discussed hydrodynamic mixing within the radiative regions of stars and presented several observational tests of the mechanism. This paper presents a re-analysis of the eclipsing binary sample and solar models, with more realistic mixing physics as well as additional minor improvements to the code. Section

2 summarizes the additional physics and improvements to the code. Solar models are examined in Section 3. The eclipsing binary sample is presented in Section 4. Section 5 contains discussion and conclusions. The implications for post-main sequence evolution will be presented in a subsequent paper.

4.2 The TYCHO Code

The TYCHO code is a 1D stellar evolution and hydrodynamics code written in structured FORTRAN77 with online graphics using PGPLOT. The code is as described in Young, Mamajek, Arnett, & Liebert (2001). We have made substantial additions and improvements. The code is now functional for stars from the hydrogen burning limit to arbitrarily high masses, and for metallicities of $z = 0$ to the limit of the OPAL opacity tables.

The opacities used are from Iglesias & Rogers (1996) at high temperatures and Alexander & Ferguson (1994) for low temperatures. The OPAL tables have been extended to low entropies, and are formally adequate for calculating stellar interiors down to the hydrogen burning limit. In reality, a number of contributions, particularly from molecular species, are not included. Stellar models computed with these tables are reliable to perhaps $0.5 M_{\odot}$.

TYCHO uses an adaptable set of nuclear reaction networks, which are constructed automatically from rate tables given a list of desired nuclei. In these calculations a 176 element network complete through the iron peak was used at $T > 10^7$ K, and a 15 element network for light element depletion at lower temperatures. Rates for the full network are from Rauscher & Thielemann (2000). Caughlan & Fowler (1988) rates are used in the light element network.

Mass loss capabilities of the code have been extended. At $T_{eff} > 7.5 \times 10^3$ K, the theoretical approach of Kudritzki et al. (1989) is used. At lower T_{eff} routines

based upon the empirical prescription of Dupree & Reimers (1987) or Blöcker (1995) are available. Low temperature mass loss was not important in any of the cases studied here, and the Reimers and Blöcker algorithms converge in the limit of low luminosity. A treatment of radiatively driven mass loss in Wolf-Rayet stars based upon the work of Lamers & Nugis (2003) is also included in the code. It does not come into play for these models and will be discussed in a separate paper.

The equation of state has been expanded from the modified Timmes & Swesty (2000) EOS in Young, Mamajek, Arnett, & Liebert (2001) to include a more generalized treatment of the coulomb properties of the plasma. The formation and dissociation of molecular hydrogen and its effect upon the equation of state are also included in a Helmholtz free energy formulation. The OPAL project has extended its EOS determinations to lower entropies. The improved TYCHO equation of state agrees with the OPAL EOS to better than 1% for most conditions. There remains a difficult region ($10^{-1} \leq \rho \leq 10^1 \text{ g cm}^3$ and $T \leq 10^{5.5} \text{ K}$) in which the plasma is a strongly interacting coulomb system, and in which the difference exceeds 4%. This region is relevant for low mass stars ($M < 0.5 M_{\odot}$).

TYCHO uses a modified version of Ledoux convection which avoids the problem of instantaneous mixing in convective regions with nuclear burning during short timesteps. Simple Eddington-Sweet rotational mixing (Tassoul, 2000) is implemented in the code. All models were run with an improved version of the inertial wave driven mixing described in Young et al. (2003). The new algorithm determines a characteristic wavelength for the waves from the Brünt-Vaisälä condition (Hansen & Kawaler, 1994; Cox, 1980). This new formulation is sensitive to composition gradients which affect the propagation of g-modes which drive mixing. Gravitational settling and differential diffusion of nuclear species according

to Thoul, Bahcall, & Loeb (1994) is also included. The Thoul, Bahcall, & Loeb (1994) treatment of diffusion is generalizeable to an arbitrary number of nuclear species, though that work examines only H, He, O, and Fe. We calculate diffusion coefficients separately for the species important to the OPAL type 2 opacity tables (H, He, C, and O) and on average for iron peak and Ne like elements. Michaud et al. (2004) examine the effect of settling on the approximately solar age and metallicity clusters M67 and NGC 188, using 19 elements. They find that the largest effects on stellar structure result from elements with a significant contribution to the opacity, as we assume in our treatment. In light of these results our intermediate simplification appears adequate for stellar structure calculations.

Numerous minor improvements have been made which improve convergence and stability of the code, and allow it to perform adequately at the small timesteps typical of neutrino-cooling dominated burning stages (C burning and later) as well as the slow hydrogen burning stages. The code is publicly available and open source. The current version (TYCHO-7.0) is being made available, along with an extensive suite of analysis tools, at <http://pegasus.as.arizona.edu/~darnett>.

4.3 Solar Models

As the best observed star in the sky, the sun is an obligatory test case for any comprehensive stellar evolution code. The helioseismological measurements of sound speed and depth of the convective zone give us an insight into the interior structure not available for any other star. In this section we test solar models from TYCHO, but with a somewhat novel aim. We hope that TYCHO will function as a predictive tool for building stellar populations. Therefore, instead of finding a best fit to objects as they are observed now, with variable initial conditions, the code must be able to predict a unique (and accurate) path through stellar param-

eter space over time for a particular initial mass and composition. Conversely, we would also like to connect any given observed star to a unique initial condition. We would wish to do this for the complete range of stellar masses. As such we are more interested in the comparison of our models with the sun assuming only an initial solar mass and composition and our best treatment of the physics, and not how precisely we can fit the sun by optimizing our models. A $1 M_{\odot}$ star on the main sequence is probably the easiest type of star to model, being relatively insensitive to the effects of mixing and mass loss. Solar models give us an estimate of the minimum uncertainty in our predictions of stellar parameters.

We examine four models, s0, s1, s2, and s3 which differ in the completeness of mixing physics included. Model s0 includes gravitational settling and diffusion (Thoul, Bahcall, & Loeb, 1994) and inertial wave-driven mixing (Young et al., 2003). Model s1 includes only wave-driven mixing and s2 only gravitational settling and diffusion. Model s3 uses only Ledoux convection and ignores other mixing physics. We also calculate one model with physics identical to s0, but with Lodders (2003) values for solar abundances. There is one glaring free parameter which must of necessity remain in this 1-D code. We choose a mixing length parameter of $\alpha = 2.1$. This is in the same range as values deduced from solar standard models ($\alpha = 2.05$) (Basu, Pinsonneault, & Bahcall, 2000) and multidimensional simulations of the solar convective zone with hydrodynamics and radiative transfer ($\alpha = 2.13$) (Robinson et al., 2004). Smaller values of the mixing length parameter result in larger radii for the 1-D models. Table 4.1 gives values for gross observables (R, T_{eff}, L), rms difference in predicted and observed sound speed, depth of convection zone, photospheric He and Li values, and central temperature for each model. Table 4.2 gives neutrino fluxes for the models and a selection of models from Bahcall & Pinsonneault (2004). We have not per-

Table 4.1. Characteristics of Solar Models with Varied Mixing Physics

Model	R/R_{\odot}	$\log T_e$	$\log L/L_{\odot}$	rms δc_s (%)	R_{conv}/R	X_{He}	$\log \epsilon(^7Li)$	T_c
s0	0.993	3.765	3.80×10^{-3}	0.56	0.714	0.242	1.14	1.560×10^7
s1	0.972	3.770	7.65×10^{-3}	0.90	0.729	0.279	1.78	1.564×10^7
s2	0.985	3.767	5.93×10^{-3}	0.50	0.718	0.240	3.05	1.562×10^7
s3	0.971	3.770	6.85×10^{-3}	0.97	0.729	0.279	3.11	1.563×10^7
l0	0.944	3.777	9.21×10^{-3}	2.24	0.672	0.252	-4.89	1.558×10^7
solar ^a	0.0	3.762	0.11	0.714	0.244	1.1	1.569×10^7	

^aSolar values from standard solar model of Bahcall, Pinsonneault, & Basu (2001) except $\log \epsilon(^7Li)$ from Boothroyd & Sackmann (2003)

formed an inversion of the helioseismological data through our model to obtain expected sound speeds for our models. The values to which we compared are those calculated by Bahcall, Pinsonneault, & Basu (2001). Performing this direct comparison we find rms errors in sound speed of $\sim 0.5\%$ for our best models. Most of this discrepancy can be attributed to our error in the solar radius. (Bahcall, Pinsonneault, & Basu (2001) find a 0.15% rms error for a model with a 0.04% difference in radius from their standard value.)

The values in Table 4.1 illustrate some of the subtleties involved in distinguishing between models. If we accept a constraint on the mixing length from simulations or helioseismology, all variants of the model predict gross observables to within 3%. The models with more complete mixing physics show a slightly better agreement, but the variation is less than the uncertainty in the exact nature of the convection. The minimum uncertainty in our predictions must be taken to be larger than 3%, because the error is dominated by a fictitious parameter. Varying the mixing length by 0.1 results in roughly a 1% change in the radius. Simulations of red giant atmospheres (Asida, 2000) and observations of

Table 4.2. Neutrino Fluxes for Solar Models with Varied Mixing Physics

Model	pp $10^{10}\text{cm}^2\text{s}^{-1}$	pep $10^8\text{cm}^2\text{s}^{-1}$	hep $10^3\text{cm}^2\text{s}^{-1}$	Be^7 $10^9\text{cm}^2\text{s}^{-1}$	B^8 $10^6\text{cm}^2\text{s}^{-1}$	N^{13} $10^8\text{cm}^2\text{s}^{-1}$	O^{15} $10^8\text{cm}^2\text{s}^{-1}$	F^{17} $10^6\text{cm}^2\text{s}^{-1}$
s0	5.95	1.42	7.91	4.83	5.51	4.08	3.49	4.59
s1	5.97	1.42	7.84	4.86	5.59	4.12	3.53	4.65
s2	5.96	1.42	7.84	4.81	5.44	4.04	3.45	4.54
s3	5.97	1.42	7.85	4.84	5.51	4.09	3.49	4.58
BP04 ^a	5.94	1.40	7.88	4.86	5.79	5.71	5.03	5.91
BP04+	5.99	1.42	8.04	4.65	5.02	4.06	3.54	3.97
Comp	6.00	1.42	9.44	4.56	4.62	3.88	3.36	3.77
N^{14}	5.98	1.42	7.93	4.86	5.74	3.23	2.54	5.85

^aNeutrino fluxes from standard model and models with various improvements in physics from Bahcall & Pinsonneault (2004)

pre-main sequence (pre-MS) binaries (Hillenbrand & White, 2004; Stassun et al., 2004) indicate that stars with low surface gravities and larger convective cell sizes and/or Mach numbers and turbulent pressures have different convective physics than main sequence stars of the same luminosity. In a 1D description of convection, this manifests as a change in the mixing length to values of roughly 1.5 for red giants and possibly pre-MS stars. Without constraints on the nature of convection the minimum predictive uncertainty is roughly 7% for a $1M_{\odot}$ star of solar age. Varying the abundance from Grevesse & Sauval (1998) to Lodders (2003) introduces a further uncertainty of $\sim 5\%$ in surface observables, and a much larger variance for helioseismological and abundance tests.

Using helioseismology and detailed chemical abundances, we can begin to discriminate between models. Unsurprisingly, model s3, with mixing limited to Ledoux convection, is ruled out immediately. Model s1, with radiative region mixing but no heavy element diffusion, is also eliminated by the size of the con-

vective zone and surface helium abundance. Clearly gravitational settling and diffusion are necessary to fit the observed sun. The only observable difference between the remaining diffusion-only and more realistic mixing models lies in the predicted photospheric Li abundance. This is exactly what is to be expected, since helioseismology tells us that, while mixing must be present in the radiative regions to account for abundances, it cannot have a large *structural* effect.

Michaud et al. (2004) confirm this result for the solar age and metallicity clusters M67 and NGC 188. They find that models with little or no “overshooting” are consistent with the observed color-magnitude diagrams of the clusters. Our theory of mixing naturally predicts little structural effect on solar-type stars and only a small increase in core size for stars which star with small convective cores. We do see a significant effect on the sun during the pre-MS, when the transient convective core established during partial CN burning is at its largest.

With no mixing (save settling) outside the convection zone, model s2 greatly under-predicts the depletion of Li at the solar photosphere. The model with complete mixing gives an abundance much closer to the observed value of $\log \epsilon(^7\text{Li}) = 1.1 \pm 0.1$ (Boothroyd & Sackmann, 2003), though this, too is sensitive to the mixing length at the factor of 2 to 4 level. The role of rotation coupled to oscillations in driving mixing has been discussed extensively by many investigators ((i.e. Chaboyer, Demarque, & Pinsonneault, 1995; Pinsonneault et al., 2002)). The work of Charbonnel & Talon (1999); Talon, Kumar, & Zahn (2002) suggests that mixing is damped in rotating stars on the red side of the Li dip, corresponding to early G stars. If the pre-MS sun was a slow rotator, it may be a limiting case where angular momentum transport produces a minimal modification in the stellar g-mode oscillation spectrum and mixing is at a maximum. This provides a possible explanation for the strong depletion of Li in the sun relative to some field G stars,

and for the wide observed range of depletions, but the problem is beyond the scope of this paper.

The values for neutrino fluxes in Table 4.2 all fall within the range of variation found by Bahcall & Pinsonneault (2004) for variant models with improved physics. A selection of the Bahcall & Pinsonneault (2004) models illustrating the range of variation between the models are given in Table 2.2. The neutrinos do not provide a constraint on the models at this level, but do confirm that none of the physics included in the models is in conflict with the observations.

The solar models highlight some of the problems in assessing the predictive power of stellar evolution codes. The models presented here would be indistinguishable for a G2 star outside the solar system. The errors in the gross observables could be compensated for by a change in the mixing length without including the necessary physics of He and heavy element diffusion and non-convective mixing. Helioseismology would not be available to falsify such a model based upon convective zone depth or sound speeds. Abundance determinations from high resolution spectroscopy are not always available. One may argue whether it is then important to have complete physics. Figure 4.1 illustrates the potential traps that lie in validating code with a narrow selection of observations. At the solar age models *s0* and *s2* (both with diffusion) are nearly identical, as are *s1* and *s3* (both without). The effects of diffusion clearly dominate in determining the sun's position in the HR diagram. On the pre-MS during partial CN burning in the transient convective core, the case is very different. Models *s0* and *s1* (inertial wave-driven mixing) are nearly identical, as are *s2* and *s3* (convective mixing only). The shape of the pre-MS is determined primarily by the change in convective core size resulting from including more complete mixing physics. Diffusion has had insufficient time to make much difference. In short, the evolutionary his-

tory is not unique. A model which fits the present day sun perfectly may be substantially inaccurate for other evolutionary stages (or equivalently mass ranges or compositions) where different physics come into play. Calibrations based upon any one type of data set should not be extended into other regimes unless based upon a valid physical theory.

4.4 Eclipsing Binaries

The double-lined eclipsing spectroscopic binaries in Andersen (1991) provide us with a sample of stars from $1M_{\odot} < M < 23M_{\odot}$ with precisely determined masses and radii. A subset of these stars also have measured apsidal motions, which provide some information on the interior density profiles and core sizes of the stars. We use the same sample as Young, Mamajek, Arnett, & Liebert (2001) so that a direct comparison of the same code with and without missing physics can be made. We use the most recent values available for observed quantities (observed quantities and references can be found in Table 4.3.)

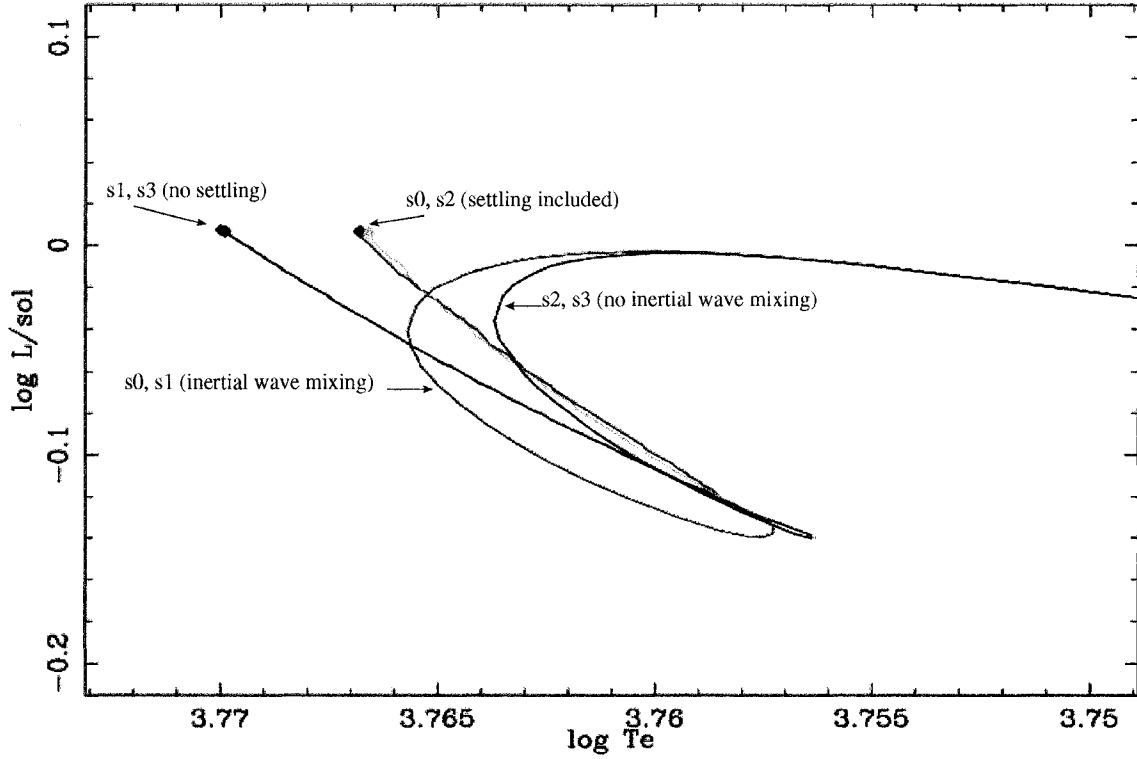


Figure 4.1: Evolutionary tracks for $1 M_{\odot}$ stars with four variations on mixing physics. Model s0 includes gravitational settling/heavy element diffusion and inertial wave-driven mixing in radiative regions. Model s1 contains only wave mixing. Model s2 includes only settling/diffusion. Model s3 has no mixing outside of convective regions. Models with hydrodynamic mixing in radiative regions (s0 and s1) are indistinguishable on the pre-MS, when the shape of the track is controlled primarily by the size of the small convective core that exists during partial CN burning. Diffusion has insufficient time to work on the pre-MS and does not affect the tracks. On the main sequence, after the convective core disappears, the shape of the track is determined by the presence (s0 & s2) or absence (s1 & s3) of diffusion and settling.

Table 4.3. Observed parameters for selected binary systems.^a

System	P(d)	Star	Spect.	Mass/ M_{\odot}	Radius/ R_{\odot}	$\log g(\text{cm/s}^2)$	$\log T_e(\text{K})$	$\log L/L_{\odot}$
EM Car	3.41	A	O8V	22.3 ± 0.3^b	9.34 ± 0.17	3.864 ± 0.017^b	4.531 ± 0.026	5.02 ± 0.10
HD97484	...	B	O8V	20.3 ± 0.3^b	8.33 ± 0.14	3.905 ± 0.016^b	4.531 ± 0.026	4.92 ± 0.10
V478 Cyg	2.88	A	O9.5V	16.67 ± 0.45	7.423 ± 0.079	3.919 ± 0.015	4.484 ± 0.015	4.63 ± 0.06
HD193611	...	B	O9.5V	16.31 ± 0.35	7.423 ± 0.079	3.909 ± 0.013	4.485 ± 0.015	4.63 ± 0.06
CW Cep	2.73	A	B0.5V	12.9 ± 0.1^c	5.685 ± 0.130	4.039 ± 0.024^c	4.449 ± 0.011^d	4.26 ± 0.06^e
HD218066	...	B	B0.5V	11.9 ± 0.1^c	5.177 ± 0.129	4.086 ± 0.024^c	4.439 ± 0.011^d	4.14 ± 0.07^e
QX Car	4.48	A	B2V	9.267 ± 0.122	4.289 ± 0.091	4.140 ± 0.020	4.395 ± 0.009^d	3.80 ± 0.04^e
HD86118	...	B	B2V	8.480 ± 0.122	4.051 ± 0.091	4.151 ± 0.021	4.376 ± 0.010^d	3.67 ± 0.04^e
CV Vel	6.89	A	B2.5V	6.100 ± 0.044	4.087 ± 0.036	4.000 ± 0.008	4.254 ± 0.012^d	3.19 ± 0.05
HD77464	...	B	B2.5V	5.996 ± 0.035	3.948 ± 0.036	4.023 ± 0.008	4.251 ± 0.012^d	3.15 ± 0.05
U Oph	1.68	A	B5V	5.198 ± 0.113	3.438 ± 0.044	4.081 ± 0.015	4.211 ± 0.015^d	2.87 ± 0.08^e
HD156247	...	B	B6V	4.683 ± 0.090	3.005 ± 0.055	4.153 ± 0.018	4.188 ± 0.015^d	2.66 ± 0.08^e
ζ Phe	1.67	A	B6V	3.930 ± 0.045	2.851 ± 0.015	4.122 ± 0.009	4.149 ± 0.010^d	2.46 ± 0.04^e
HD6882	...	B	B8V	2.551 ± 0.026	1.853 ± 0.023	4.309 ± 0.012	4.072 ± 0.007^d	1.78 ± 0.04^e
IQ Per	1.74	A	B8V	3.521 ± 0.067	2.446 ± 0.026	4.208 ± 0.019	4.111 ± 0.008^d	2.17 ± 0.03^e
HD24909	...	B	A6V	1.737 ± 0.031	1.503 ± 0.017	4.323 ± 0.013	3.906 ± 0.008^d	0.93 ± 0.04^e
PV Cas	1.75	A	B9.5V	2.815 ± 0.050^d	2.297 ± 0.035^d	4.165 ± 0.016^d	4.032 ± 0.010^d	1.80 ± 0.04^e
HD240208	...	B	B9.5V	2.756 ± 0.054^d	2.257 ± 0.035^d	4.171 ± 0.016^d	4.027 ± 0.010^d	1.77 ± 0.04^e
AI Hya	8.29	A	F2m	2.145 ± 0.038	3.914 ± 0.031	3.584 ± 0.011	3.851 ± 0.009^d	1.54 ± 0.02^e
+0° 2259	...	B	F0V	1.978 ± 0.036	2.766 ± 0.017	3.850 ± 0.010	3.869 ± 0.009^d	1.31 ± 0.02^e
VV Pyx	4.60	A	A1V	2.101 ± 0.022	2.167 ± 0.020	4.089 ± 0.009	3.979 ± 0.009^d	1.54 ± 0.04
HD71581	...	B	A1V	2.099 ± 0.019	2.167 ± 0.020	4.088 ± 0.009	3.979 ± 0.009^d	1.54 ± 0.04
RS Cha	1.67	A	A8V	1.858 ± 0.016	2.137 ± 0.055	4.047 ± 0.023	3.883 ± 0.010^d	1.14 ± 0.05^e
HD75747	...	B	A8V	1.821 ± 0.018	2.338 ± 0.055	3.961 ± 0.021	3.859 ± 0.010^d	1.13 ± 0.05^e
EK Cep	4.43	A	A1.5V	2.029 ± 0.023	1.579 ± 0.007	4.349 ± 0.010	3.954 ± 0.010	1.17 ± 0.04
HD206821	...	B	G5Vp	1.124 ± 0.012	1.320 ± 0.015	4.25 ± 0.010	3.756 ± 0.015	0.19 ± 0.07
MY Cyg	4.01	A	F0m	1.811 ± 0.030	2.193 ± 0.050	4.007 ± 0.021	3.850 ± 0.010^d	1.03 ± 0.04^e
HD193637	...	B	F0m	1.786 ± 0.025	2.193 ± 0.050	4.014 ± 0.021	3.846 ± 0.010^d	1.02 ± 0.04^e

Table 4.3—Continued

System	P(d)	Star	Spect.	Mass/ M_\odot	Radius/ R_\odot	$\log g(\text{cm/s}^2)$	$\log T_e(\text{K})$	$\log L/L_\odot$
PV Pup	1.66	A	A8V	1.565 ± 0.011	1.542 ± 0.018	4.257 ± 0.010	3.870 ± 0.01^g	0.81 ± 0.08^e
HD62863	...	B	A8V	1.554 ± 0.013	1.499 ± 0.018	4.278 ± 0.011	3.870 ± 0.01^g	0.79 ± 0.08^e
DM Vir ^f	4.67	A	F7V	1.454 ± 0.008	1.763 ± 0.017	4.108 ± 0.009	3.813 ± 0.007	0.67 ± 0.03^h
HD123423 ^f	...	B	F7V	1.448 ± 0.008	1.763 ± 0.017	4.106 ± 0.009	3.813 ± 0.020	0.67 ± 0.03^h
V1143 Cyg	7.64	A	F5V	1.391 ± 0.016	1.346 ± 0.023	4.323 ± 0.016	3.820 ± 0.007^d	0.49 ± 0.03^e
HD185912	...	B	F5V	1.347 ± 0.013	1.323 ± 0.023	4.324 ± 0.016	3.816 ± 0.007^d	0.46 ± 0.03^e
UX Men	4.18	A	F8V	1.238 ± 0.006	1.347 ± 0.013	4.272 ± 0.009	3.789 ± 0.007^g	0.38 ± 0.03^e
HD37513	...	B	F8V	1.198 ± 0.007	1.274 ± 0.013	4.306 ± 0.009	3.781 ± 0.007^g	0.32 ± 0.03^e

^aDetailed references and discussion may be found in (Andersen, 1991).

^bStickland, Lloyd, & Corcoran (1994).

^cStickland, Koch & Pfeiffer (1992).

^dRibas et al. (2000).

^eAdjusted here for new T_{eff} and R determinations.

^fLatham et al. (1996).

^gLastennet & Valls-Gabaud (2002).

^hHillenbrand & White (2004).

As in Young, Mamajek, Arnett, & Liebert (2001), we calculate a χ^2 -like quantity for each binary pair, defined by

$$\begin{aligned}
\chi^2 = & ((\log L(m_A, t) - \log L_A)/\sigma_L(A))^2 \\
& + ((\log L(m_B, t) - \log L_B)/\sigma_L(B))^2 \\
& + ((\log R(m_A, t) - \log R_A)/\sigma_R(A))^2 \\
& + ((\log R(m_B, t) - \log R_B)/\sigma_R(B))^2,
\end{aligned} \tag{4.1}$$

where A and B denote the primary and the secondary star, respectively. Here L_A

and R_A are the observationally determined luminosity and radius of the primary, with σ_{L_A} and σ_{R_A} being the observational errors in $\log L_A$ and in $\log R_A$. We convert the observational data for the radii to logarithmic form for consistency. Correspondingly, $L(m_A, t)$ and $R(m_A, t)$ are the luminosity and radius of the model. This χ^2 was evaluated by computing two evolutionary sequences, one for a star of mass m_A and one for m_B . A χ^2 was calculated at consistent times through the entire sequence ($t_A = t_B$ to a fraction of a time step, which was a relative error of a few percent at worst). The smallest χ^2 value determined which pair of models was optimum for that binary. Note that if the trajectories of both A and B graze the error boxes at the same time, $\chi^2 \approx 4$. (With 4 degrees of freedom, the reduced χ^2 would then be 1.) We use radius instead of effective temperature in our fitting algorithm because the more precise values for R make the χ^2 more discriminating. These error parameters along with the corresponding uncertainties from the observations are presented in Table 4.4.

Table 4.4. Results for selected binary systems.

System	Star	Mass	$\log R/R_{\odot}$	$\log T_e$	$\log L$	$\log \text{Age (yr)}$	z	χ^2
EM Car	A	22.30	0.969	4.526	4.996	6.075	0.0189	0.16
HD97484	B	20.30	0.926	4.523	4.898	6.076		
V478 Cyg	A	16.71	0.881	4.476	4.618	6.310	0.0189	0.93
HD193611	B	16.31	0.865	4.474	4.580	6.312		
CW Cep	A	12.90	0.764	4.437	4.228	6.404	0.0189	0.98
HD218066	B	11.90	0.722	4.424	4.093	6.406		
QX Car	A	9.267	0.640	4.372	3.721	6.531	0.0189	0.30
HD86118	B	8.480	0.602	4.354	3.576	6.563		
CV Vel	A	6.100	0.609	4.255	3.193	7.295	0.0189	0.08
HD77464	B	5.996	0.602	4.251	3.159	7.299		
U Oph	A	5.198	0.535	4.221	2.906	7.379	0.0189	0.03
HD156247	B	4.683	0.484	4.197	2.708	7.380		
ζ Phe	A	3.930	0.455	4.157	2.490	7.703	0.013	4.03
HD6882	B	2.551	0.261	4.055	1.693	7.728		
IQ Per	A	3.521	0.382	4.124	2.211	7.547	0.0189	3.07
HD24909	B	1.737	0.180	3.913	0.965	7.547		
PV Cas	A	2.827	0.348	4.037	1.797	6.490	0.0189	1.00
HD240208	B	2.768	0.357	4.027	1.772	6.491		
AI Hya	A	2.145	0.602	3.834	1.492	8.556	0.023	4.12
+0° 2259	B	1.978	0.434	3.877	1.329	8.558		
VV Pyx	A	2.101	0.339	3.981	1.555	8.610	0.007	0.33
HD71581	B	2.099	0.339	3.980	1.553	8.612		
RS Cha	A	1.858	0.317	3.903	1.198	6.866	0.0189	2.78
HD75747	B	1.821	0.358	3.880	1.189	6.867		
EK Cep	A	2.029	0.209	3.968	1.242	7.357	0.0189	5.13
HD206821	B	1.124	0.108	3.749	0.165	7.357		
MY Cyg	A	1.811	0.337	3.867	1.095	8.649	0.023	3.79
HD193637	B	1.786	0.327	3.865	1.066	9.651		

Table 4.4—Continued

System	Star	Mass	$\log R/R_{\odot}$	$\log T_e$	$\log L$	$\log \text{Age (yr)}$	z	χ^2
PV Pup	A	1.565	0.184	3.872	0.810	8.520	0.0189	0.23
HD62863	B	1.554	0.180	3.871	0.795	8.527		
DM Vir	A	1.460	0.249	3.816	0.714	9.149	0.023	0.41
HD123423	B	1.454	0.243	3.817	0.706	9.149		
V1143 Cyg	A	1.391	0.128	3.826	0.515	8.739	0.0189	1.48
HD185912	B	1.347	0.109	3.819	0.446	8.754		
UX Men	A	1.238	0.134	3.795	0.400	9.542	0.021	1.56
HD37513	B	1.198	0.096	3.795	0.323	9.544		

As before, we note that a χ^2 statistic assumes that the observational errors have a Gaussian distribution about the mean (Press et al., 1992). This is not necessarily true, as the systematic shifts in measured quantities due to new analyses can be much larger than the formal error bars (Ribas et al., 2000; Stickland, Koch & Pfeiffer, 1992; Stickland, Lloyd, & Corcoran, 1994). Also, the quoted luminosity depends on the radius and effective temperature, and is thus not entirely independent. These systematic errors are the true limit to our power to discriminate between models, and emphasize the need for independent observational tests and numerical simulations to identify relevant physics.

Probably the greatest observational limitation we face is the lack of abundance determinations for these stars. The only binary in our sample with a spectroscopic abundance determination is UX Men ($z=0.019$) (Andersen, Clausen, Magain, 1989). A few other systems have some sort of metallicity indication in the literature. Ribas et al. (2000) derive a metallicity of $z=0.013$ from fits to evolutionary tracks for the ever troublesome ζ Phe. Synthetic BaSeL photometry of VV Pyx suggests a metallicity of $z < 0.007$, but the fits are not good (Lastennet et al., 1999). Latham et

al. (1996) and Lastennet & Valls-Gabaud (2002) argue for a metal content similar to the Hyades in DM Vir ($z=0.23$). MY Cyg A&B and AI Hya A are all peculiar metal line stars. We (somewhat arbitrarily) also assign these systems a Hyades composition. AI Hya has a measured $z = 0.07$, but this is probably a surface enhancement and does not reflect the global composition of the star (Ribas et al., 2000). Other systems either have no metallicity determinations or are sufficiently near solar composition that models of solar composition fall within the observational errors.

4.4.1 Global Properties of the Errors

The χ^2 values for each binary pair with and without complete mixing physics are plotted in Figure 4.2. An arrow shows the shift in χ^2 from baseline models to models with the full suite of physics. Fifteen of the binaries have excellent fits ($\chi^2 < 4$). Only three systems are marginal (ζ Phe, $\chi^2 = 4.10$; AI Hya, $\chi^2 = 4.12$; EK Cep, $\chi^2 = 5.97$). These systems will be discussed individually later. In all cases where the previous fits were marginal to poor, the χ^2 improved. All massive binaries ($M_A, M_B > 4M_\odot$) with good fits also improved. Results were mixed for lower mass stars with good fits. In both of the latter groups, both complete and incomplete models fall within the observational errors, so there is little to distinguish between models for individual binaries. The threshold for rejection of a model with $\nu = 4$ degrees of freedom with an $\alpha = 5\%$ chance of rejecting a true hypothesis is $\chi^2 = 9.488$, so even the marginal fits do not give us a strong hold on remaining errors in our models. We must examine systematic discrepancies or wait for tighter observational error bars.

Figure 4.3 shows goodness of fit vectors with the HR diagram for all stars in the sample, with incomplete models on the left and complete models on the right. The observed points with error bars are plotted with an arrow indicating

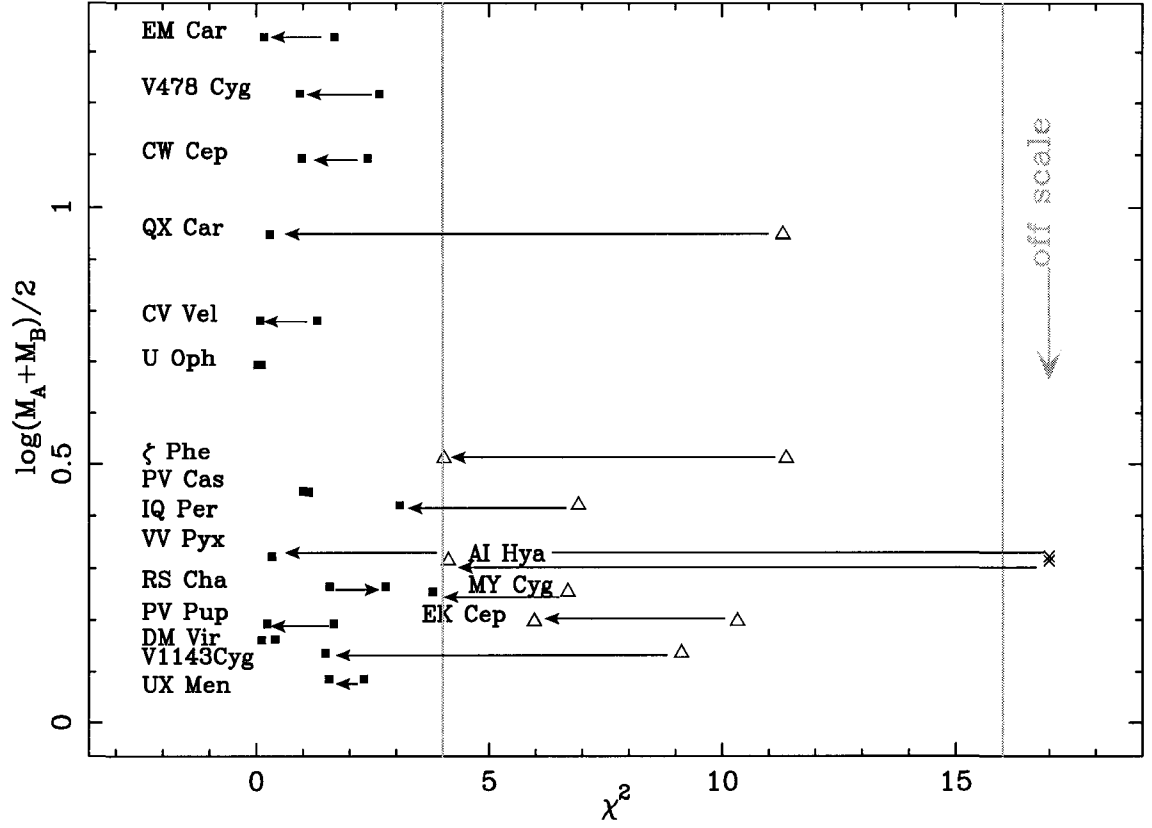


Figure 4.2: χ^2 values for optimum models of binaries, versus mean mass of the binary. Arrows are drawn from Young, Mamajek, Arnett, & Liebert (2001) values to values for current models with more complete physics. The improvement is dramatic. The vertical line at $\chi^2 = 4$ indicates a fit in which the models are just within the observational errors for both stars.

distance and direction to the best fit model point. We can now begin to discriminate between models even for formally excellent fits. The most striking feature of the figure is the behavior of the massive stars ($M > 4M_\odot$). The incomplete models are systematically underluminous. This suggests three possibilities: (1) the massive stars are all low metallicity; (2) the observational luminosity and/or mass determinations are systematically low; (3) the stars have larger convective cores than standard models predict. Option (1) is unlikely for nearby massive

stars with ages of less than 10^8 years, but cannot be absolutely ruled out without spectroscopic abundance determinations. Option 2 is possible, but again unlikely for a sample of 6 widely separated binaries. (Both EM Car and CW Cep have had their masses revised *downward* by Stickland, Koch & Pfeiffer (1992).) Option 3 seems the most likely, and is consistent with other evidence of mixing in stars beyond the standard model. Indeed, the trend of underluminous models virtually disappears when realistic mixing is included. It may be argued that the standard model is hydrodynamically inconsistent, as indicated by the instantaneous deceleration required at convective boundaries, and by detailed analysis of realistic high resolution 3-D hydrodynamic simulations, problems which our mixing algorithm addresses.

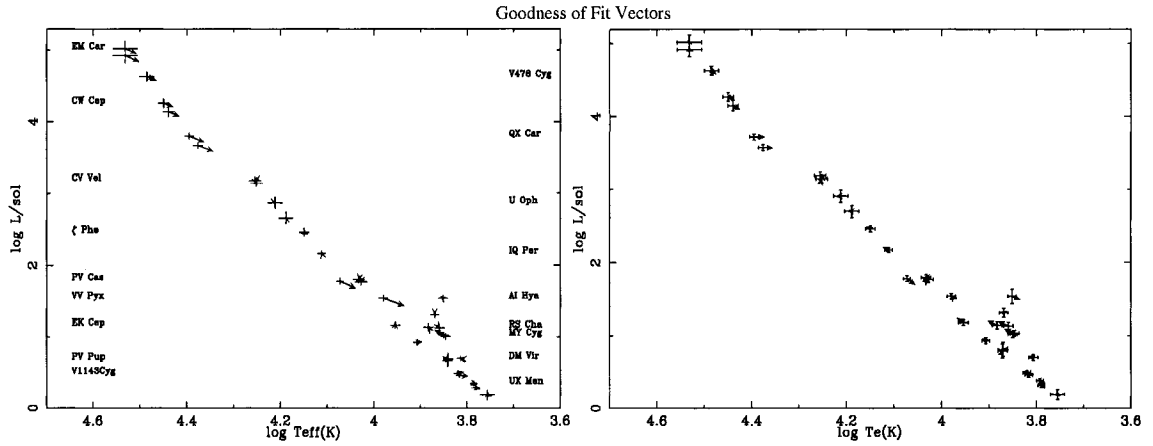


Figure 4.3: Goodness of fit vectors for each member of binary sample, with observational error bars. Results from Young, Mamajek, Arnett, & Liebert (2001) are on the left; present results on the right.

The salubrious effect of realistic mixing is confirmed by the apsidal motion tests. Models with incomplete mixing have systematically high predicted apsidal motions in the four most massive systems. This indicates that the models

are not sufficiently centrally condensed. (See Young, Mamajek, Arnett, & Liebert (2001) for a complete discussion of our previous results and methodology.) The current models with realistic mixing physics have larger convective cores and are therefore more centrally condensed. Table 4.5 summarizes the apsidal motion results for our binaries. Figure 4.4 shows the dimensionless rate of apsidal motion, $(P/U)_{CL} = (P/U)_{OBS} - (P/U)_{GR}$, which would be due to classical apsidal motion, plotted versus log of half the total binary mass (where *CL* denotes classical and *GR* general relativistic parts, and *OBS* the observed motion). P is the orbital period and U the apsidal period. The observational data (corrected for general relativity) are shown as diamonds, with vertical error bars. All of the massive star models now fall within the error bars for the measured apsidal motion with the exception of QX Car, which differs by roughly two and a half sigma (insofar as sigma is a meaningful expression of these errors). QX Car does not differ from the measured point by a larger absolute amount than the other binaries; it simply has much tighter error bars. Either the observational uncertainties are underestimated or, equally likely, the models are still missing some physics. We have reanalyzed all of the binaries from EM Car to IQ Per. The lower mass binaries all have quoted apsidal motions smaller than the predicted general relativistic term. We find it more likely that there are errors in measuring an apsidal motion with periods of centuries than in weak-field general relativity.

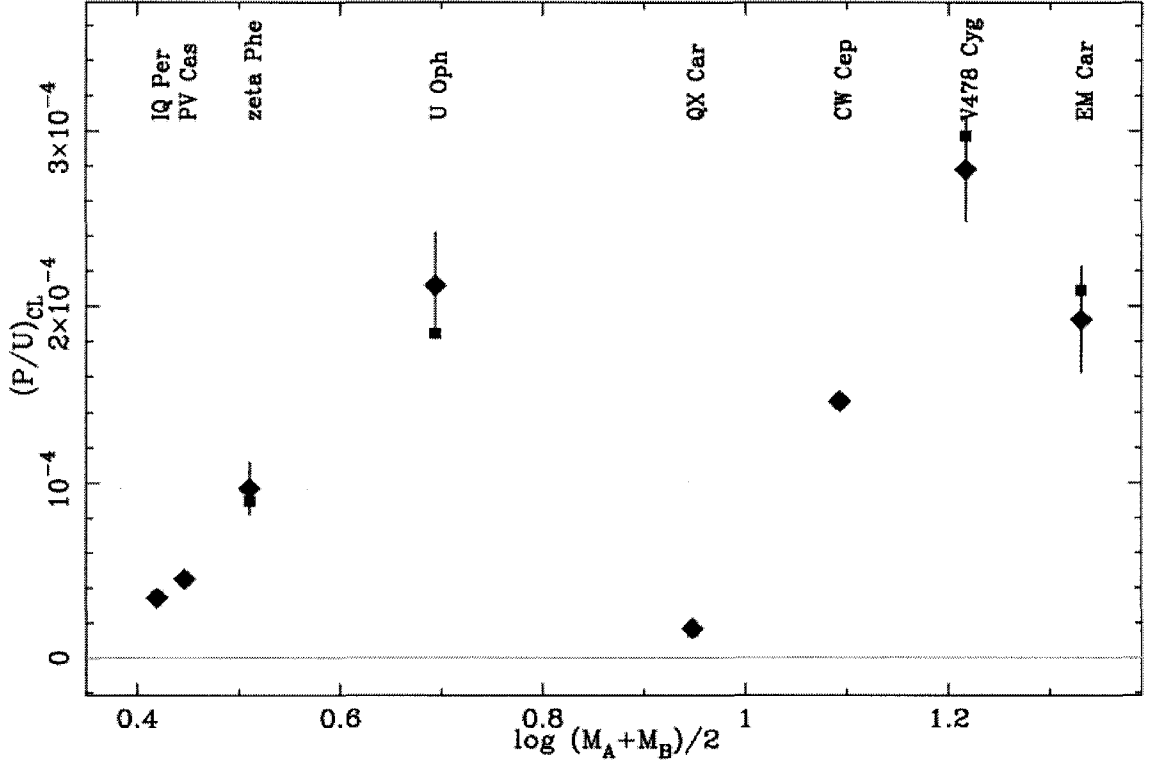


Figure 4.4: Classical apsidal motion versus mean mass, for our binaries with measured apsidal motion. $(P/U)_{CL} = (P/U)_{OBS} - (P/U)_{GR}$ is assumed. Diamonds are measured values with error bars, and squares are model predictions. In several cases the error bars and predictions both fall inside the diamonds.

4.4.2 Individual Systems of Interest

4.4.2.1 ζ Phe

This system is perennially troublesome to stellar modelers (i.e. Ribas et al., 2000). It is difficult to fit both components with the same metallicity. We adopt $z = 0.013$, following Ribas et al. (2000) and achieve a marginal fit ($\chi^2 = 4.026$). The secondary star is more luminous than the models when a good fit is achieved for the primary. If the observations are correctly interpreted, then the secondary model requires either a lower metallicity or enhanced mixing.

Table 4.5. Apsidal comparisons for selected binary systems.

System	Star	Mass	$-\log k_i$	$(k_2 R^5)^a$	P/U_{CL}^b	P/U_{GR}^b	P/U_{CL+GR}^b	P/U_{OBS}^b
EM Car	A	22.3	1.920	347.0	2.091	0.275	2.37	2.2 ± 0.3
	B	20.3	1.935	267.5				
V478 Cyg	A	16.67	1.935	160.6	2.97	0.223	3.19	3.0 ± 0.3
	B	16.31	1.917	140.0				
CW Cep	A	12.90	1.878	49.50	1.46	0.178	1.63	1.640 ± 0.014
	B	11.90	1.894	32.11				
QX Car	A	9.267	1.898	13.97	0.156	0.170	0.326	0.340 ± 0.006
	B	8.480	1.936	10.58				
U Oph	A	5.198	2.124	2.687	1.85	0.0827	1.93	2.2 ± 0.3
	B	4.683	2.111	1.571				
ζ Phe	A	3.930	2.308	1.025	0.894	0.0624	0.956	1.03 ± 0.15
	B	2.551	2.333	0.2018				
IQ Per	A	3.521	2.278	0.4478	0.335	0.0553	0.410	0.40 ± 0.03
	B	1.737	2.416	0.0401				
PV Cas	A	2.815	2.149	0.2012	0.414	0.0572	0.499	0.510 ± 0.011
	B	2.756	2.221	0.2375				

^aRadii R in solar units.^bMultiply tabular value by 10^{-4} .

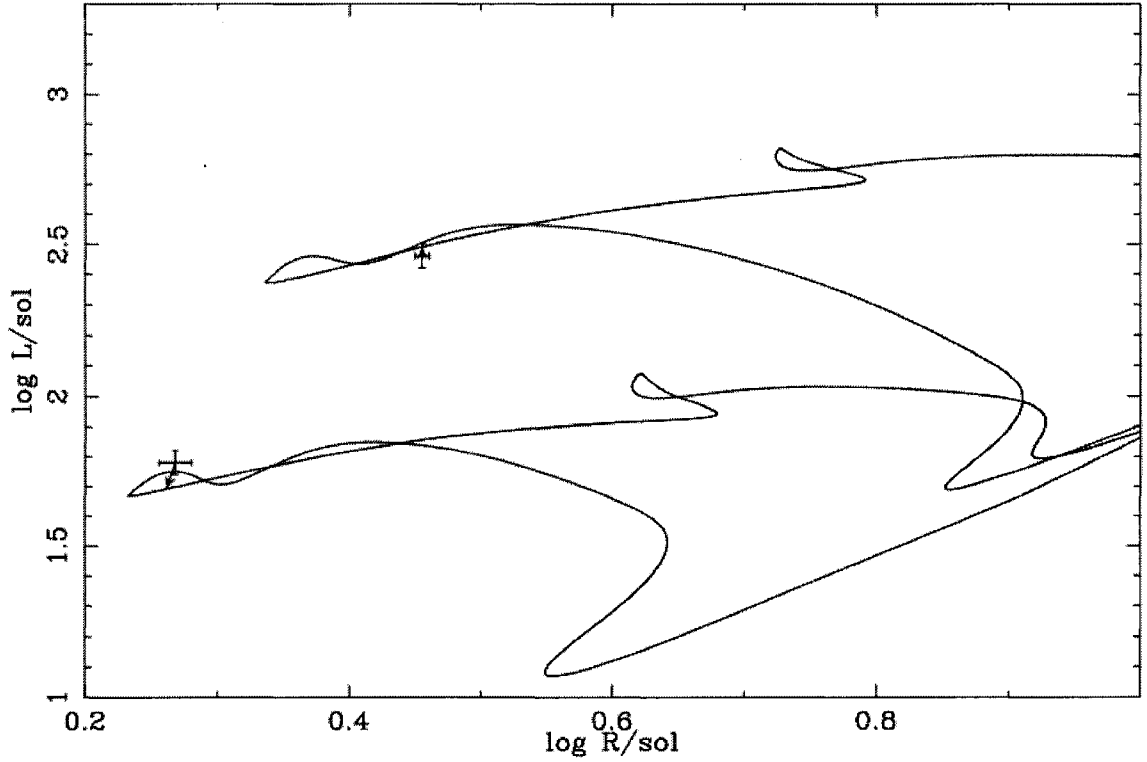


Figure 4.5: Evolutionary tracks ($z = 0.013$) and observed points with errors for ζ Phe. Note that the secondary star is more luminous than the models when the primary is well fit.

4.4.2.2 AI Hya

AI Hya is identified as a peculiar metal line star (spectral class F2m). Its metallicity is measured as $z = 0.07$ (Ribas et al., 2000), but this is probably due to a surface enhancement. Still, the stars are probably metal rich relative to solar. Without a precise determination of the interior composition we choose to use a Hyades composition ($z = 0.023$) as being in the reasonable range of nearby metal rich compositions. In keeping with our effort to test the predictability of our code, we do not try to optimize the fit by further varying the composition. This system is particularly interesting in that increased metallicity alone cannot reconcile tracks

with only convective mixing with the observations. The primary of the system lies farther redward in the HR diagram than the terminal age main sequence (Young, Mamajek, Arnett, & Liebert, 2001). The lifetime on the Hertzsprung gap for a $2 M_{\odot}$ star is short. It is possible to catch a star in that stage, but unlikely, as $\tau_{\text{gap}}/\tau_{\text{MS}} < 2\%$. More realistic mixing gives a larger convective core, extending the track redward so that a fit on the main sequence is easily achievable.

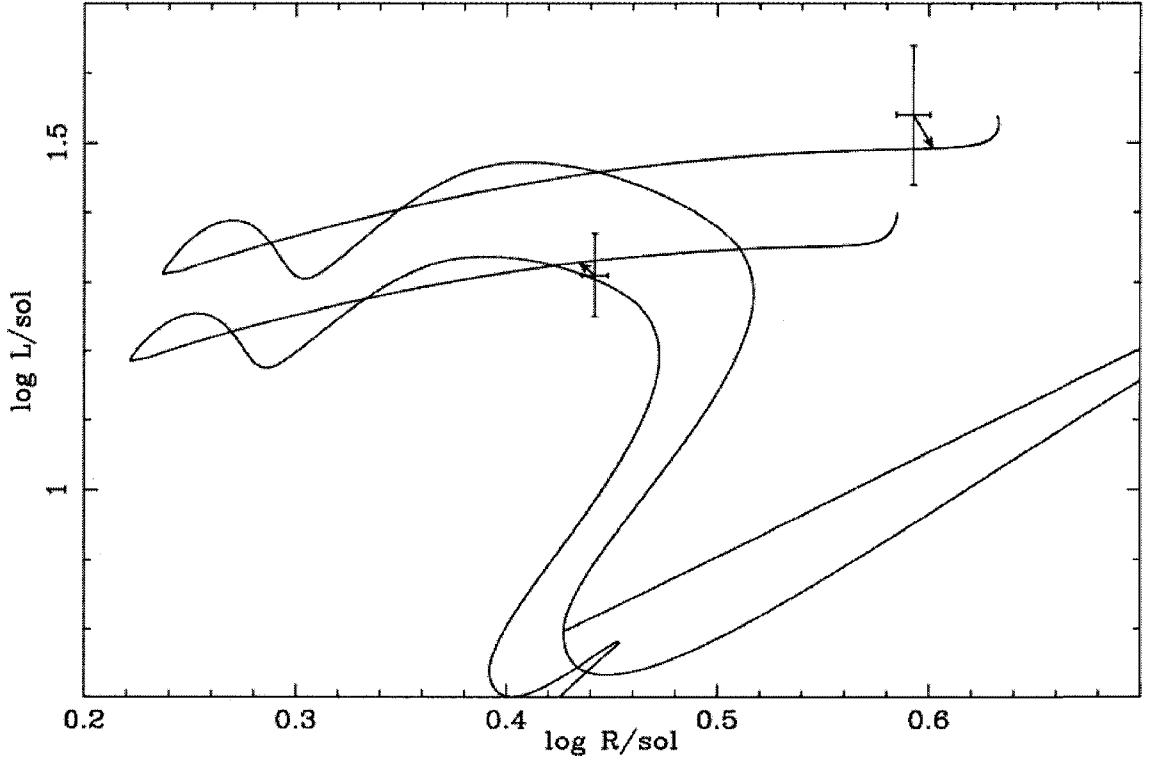


Figure 4.6: Evolutionary tracks ($z = 0.023$) and observed points with errors for AI Hya. Realistic mixing allows an acceptable fit to this previously difficult pair.

4.4.2.3 EK Cep

EK Cep and RS Cha are both pre-MS systems (Popper, 1987; Mamajek, Lawson, & Feigelson, 2000). The fit to RS Cha is formally a good one ($\chi^2 = 2.776$), and we do not attempt to optimize within the observational errors. EK Cep, however,

achieves only a marginal fit ($\chi^2 = 5.973$), because the radius of the secondary star is larger than that of the models during the first rise of the CN burning bump. (Other early pre-MS models show similar behavior, so we suspect this is systematic. A larger sample will be discussed in a forthcoming paper.) This is a robust behavior, in the sense that most things we could do to the models do not push them in the right direction. The non-convective mixing physics does not have a substantial effect, and increased metallicity would change the luminosity too much to result in a good fit. We can only find good agreement by reducing the mixing length parameter to $\alpha = 1.6$. This suggests a change in the nature of the convection, but since α does not represent a physical entity, it does not tell us what that change is. We may speculate that since the star is trying to transport an amount of energy to a surface with a larger radius than a main sequence star of similar luminosity, the convective Mach numbers must be higher. The high Mach number convection contributes a proportionally greater term to the stress tensor than main sequence convection and manifests as a radially directed pressure term, which would result in a larger radius for hydrostatic equilibrium. Besides this term, there are plasma effects, non-hydrogenic molecular contributions to the EOS, molecular and grain opacities, and subtleties of atmosphere models which must be taken into account which may contribute to the resolution of the problem. In short, we can identify a deficiency in our physics, and probably localize it to the physics of convection, but we do not have good predictive accuracy in this evolutionary stage. We quote the χ^2 for our usual value of $\alpha = 2.1$, and not the improved fit for $\alpha = 1.6$, since this is not a predictable change. We plan 3-D simulations of convection in pre-MS and MS stars, which we hope will characterize the difference in the convection in a physical way.

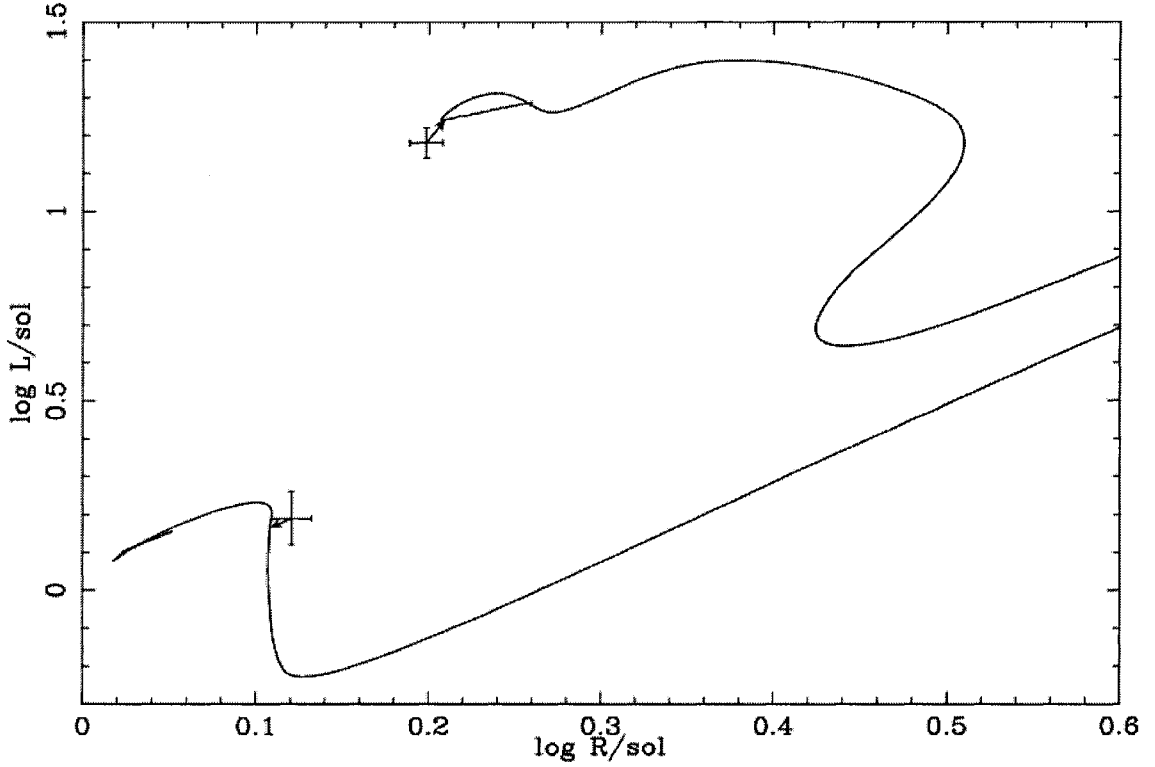


Figure 4.7: Evolutionary tracks ($z = 0.019$) and observed points with errors for EK Cep. The models for the secondary star were run with a reduced mixing length parameter of $\alpha = 1.6$ in order to increase the model radius to that of the observations. This indicates a change in the nature of the convection.

4.4.2.4 TZ For

TZ For was not in our original binary sample, but is a sufficiently interesting system that we examine it briefly here. The secondary is a subgiant in the Hertzsprung gap (Pols et al., 1997b) with a spectroscopically determined metallicity of $z = 0.024 \pm 0.007$. Lastennet & Valls-Gabaud (2002) attempt to fit the secondary with several stellar evolution codes, but are unsuccessful without changing the mass of the model by 5σ or using a composition not in agreement with the observations.

Changing the size of the convective core on the main sequence necessarily changes the path the star takes across the Hertzsprung gap. We find that with realistic mixing, our models match the hotter component of TZ For reasonably well, and the cooler component exceptionally well. The models for the subgiant are slightly overluminous. We find a $\chi^2 = 0.77$ for the binary at $t = 5.3 \times 10^8$ yr. Virtually all of this discrepancy comes from the subgiant.

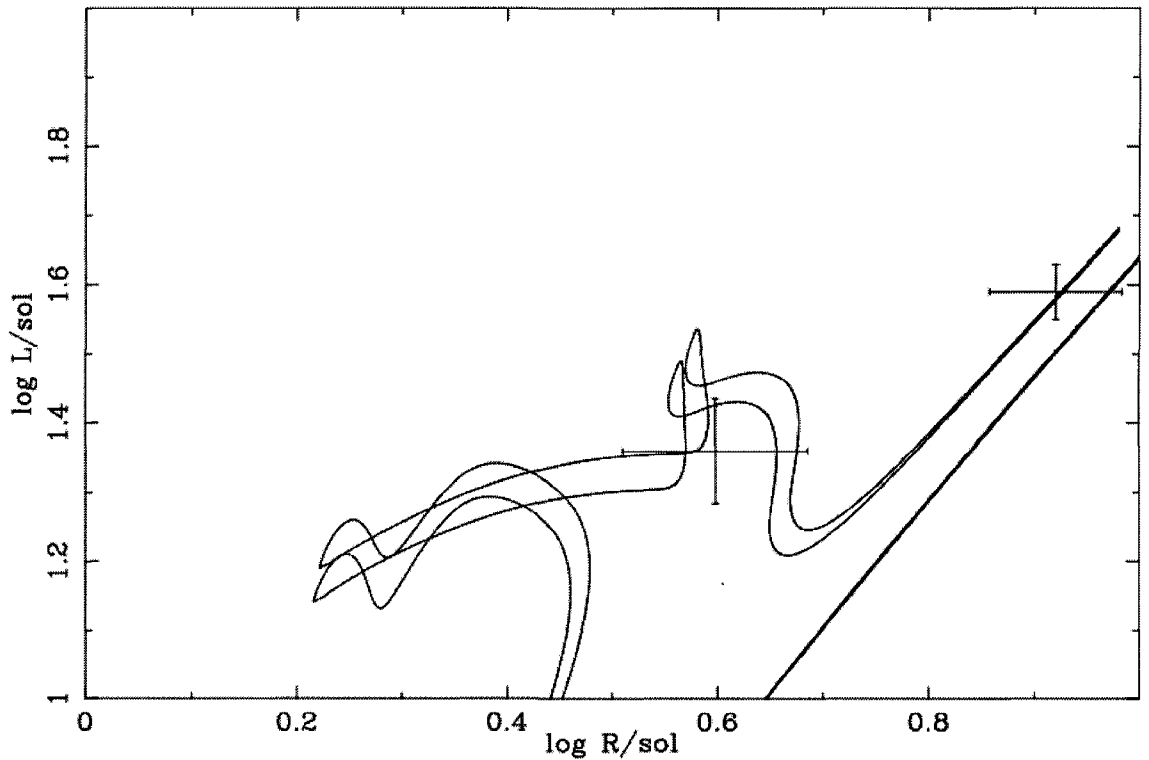


Figure 4.8: Evolutionary tracks ($z = 0.024$) and observed points with errors for TZ For. The models are slightly overluminous with respect to the observed hot component, but much improved over standard models.

4.5 Conclusions

In this paper we test the predictive power of the TYCHO stellar evolution code against a set of classical observational tests. With an improved version of the realistic mixing physics presented in Young et al. (2003), we find excellent agreement with solar models and the sample of double-lined eclipsing binaries from Young, Mamajek, Arnett, & Liebert (2001). By avoiding optimization of our models with composition changes or parameterized extra mixing, we also identify several issues which are important to future development of stellar modeling.

From the solar models we find that our predictive accuracy is limited to of order 5-10% by (1) inadequacy in our description of convection, manifested by an uncertainty in the fictitious mixing length parameter, and (2) by uncertainties in abundances. If the nature of the convection is fixed by numerical simulations of full 3-D convection, the uncertainty is reduced to that arising from the abundance determinations. The good agreement of the neutrino fluxes with those of the standard model indicate that the influence of the mixing length description is an atmospheric effect. (This is of course untrue for stars with convective cores.) The rest of our (more or less parameter-free) physics provides a good description of the interior of the sun.

One of the most striking features of the solar models underlines a fundamental problem of stellar evolution. The two models that match observed solar quantities best have virtually identical tracks on the main sequence, which are shaped primarily by the inclusion of gravitational settling and diffusion of heavy elements. The models diverge significantly, however, on the pre-MS, where the influence of hydrodynamic mixing in radiative regions dominates the evolutionary pathway while the transient convective core is at its maximum extent. (Our theoretical treatment naturally predicts a smaller effect on the HR diagram for stars

with smaller convective cores. This is consistent with the results of Michaud et al. (2004), which find minimal overshooting for the stars near the convective/radiative boundary in M67, a result which contradicts simple parameterized overshooting.) In at least some cases, a good fit to observations can be achieved without including physics which may be very important to the overall evolution. This is adequate for describing the state of an individual star, but presents a serious problem for characterizing the behavior of a star or population over time.

The eclipsing binaries provide a test of our physics, particularly the more complete mixing, over a wide range of stellar masses. The systematic problems with massive star models which were identified in Young, Mamajek, Arnett, & Liebert (2001) are ameliorated by the new treatment. The models are no longer underluminous, and the central condensations as measured by apsidal motions are no longer too small. Both of these improvements arise from larger convective core sizes resulting from the improved mixing. Simultaneously, the fits for almost all of the lower mass stars improve as well. The one case where the error formally increases only varies within the observational errors. All of the poor or marginal fits in Young, Mamajek, Arnett, & Liebert (2001) improve dramatically. Some of the improvement in these lower mass models arises from the use of high or low metallicities when warranted by the observations, but the composition alone cannot account for all of the error in the earlier models. AI Hya is a particularly fine example, for the higher mass star lies redward of the TAMS in models with incomplete mixing physics, a situation which metallicity cannot help. The more realistic mixing is necessary for good agreement. We do not optimize our models by varying composition. It is changed only when an abundance estimate appears in the literature.

Further insight into potential pitfalls can be found in the binary sample. An

increase in metallicity moves the tracks in the opposite sense of more complete mixing. It is possible to achieve an equally good fit with low metallicity and incomplete mixing or higher metallicity and more realistic physics. The practice of making stellar abundance determinations by fitting evolutionary tracks is dangerous unless the physics in the code is very well tested independently. *It is vital that accurate spectroscopic abundance determinations be made for stars used as test cases of stellar evolution, particularly eclipsing binaries.*

The pre-MS systems identify an area where our physics is still inadequate. Our predictive accuracy for these systems is not satisfactory. We must make an *ad hoc* adjustment to the mixing length in order to get large enough model radii. This tells us that our description of convection is insufficiently physical. Further multidimensional simulations of envelope convection in low surface gravity stars is necessary to resolve this problem.

When coupled with the observational tests of light element depletion and turnoff ages in young clusters in Young et al. (2003) we explore the performance of TYCHO on stars with both convective and radiative cores and convective envelopes of various sizes on the pre-MS and main sequence. All of these tests are performed with the same physics. No changes are made to the mixing or composition in order to improve our agreement with the observations. We find a strong increase in the predictive (as opposed to calibrated) accuracy throughout this range of conditions. These tests are of course a small sub-set of problems in stellar astrophysics, but we have increasing confidence in extending the approach to problems in other areas of stellar evolution. We successfully create models which cross the Cepheid instability strip, even in the lower part of the Cepheid luminosity range. In the future we plan to examine the impact of this new approach on AGB nucleosynthesis, nucleosynthesis in very low metallicity

and evolved massive stars, and the evolution of extremely massive stars which become luminous blue variables and SNIb/c progenitors.

CHAPTER 5

A MODEL FOR THE FORMATION OF HIGH DENSITY CLUMPS IN PROTO-PLANETARY NEBULAE

5.1 Observational Motivation

Mass loss from Asymptotic Giant Branch (AGB) stars is a major avenue by which heavy elements enter the interstellar medium (Kwok, 2000). In addition to the initial phase of mass loss on the AGB, a second episode is thought to occur in the post-AGB stage which is characterized by high velocity winds that collide with the remnant envelope. This wind-wind interaction is thought to generate drastic departures from spherical symmetry in the remnant shell (i.e. bi-polar), as well as very hot gas, as traced by vibrationally-excited lines of H_2 (Sahai et al., 1998a; Cox et al., 2000; Herpin et al., 2002).

Recently, Highberger et al. (2003) detected NaCl and NaCN in the post-AGB star CRL 2688 in an optically thin extended shell of radius $\sim 10\text{--}12''$ (a few $\times 10^{17}$ cm at ~ 1 kpc). This result is surprising, as it corresponds to a much larger physical radius than is observed in the AGB star IRC+10216 (Guélin, Lucas, & Neri, 1997). The NaCl lines in CRL 2688 do not show the high-velocity tails characteristic of post-AGB mass ejection. Instead, the cusp-shaped line profiles of NaCl, observed with the IRAM 30m telescope, indicate an extended, shell-like distribution for NaCl coincident with the low velocity AGB remnant wind. A similar interpretation holds for NaCN. The observed transitions of NaCl and NaCN in CRL 2688 require densities of $n(\text{H}_2) \sim 5 \times 10^6 \text{ cm}^{-3}$ to $n(\text{H}_2) \sim 10^8 \text{ cm}^{-3}$ for $T_K \sim 50$ K to be excited. These values are inconsistent with an undisturbed

AGB remnant wind (Highberger et al., 2003).

We propose that clumping of material near the interface between the slow AGB wind and the fast post-AGB wind can reach the requisite densities for excitation of the observed transitions of NaCl and NaCN. This clumping is driven by a thermal instability arising in a hydrodynamic shock. In this letter we present two dimensional proof-of-principle calculations which show that the clumping process occurs and is robust for conservative estimates of proto-planetary nebula (PPN) conditions, and that the clumping can produce the requisite densities.

5.2 Theory of Clumping

Modeling of the interaction of winds in post-AGB stars and PPN by using one-dimensional spherically symmetric shocks precludes inclusion of physics relevant to the morphology and conditions in the interaction region. In particular, the assumption of spherical symmetry prevents material from fragmenting into small clumps which can have significantly enhanced density and a more radially extended distribution than a simple shock.

The inclusion of radiative cooling in the gas physics gives the possibility of a thermal instability. In this scenario, the clumps are pressure-confined. Cooling is usually non-linear with density (i.e., following Osterbrock (1989), $\Lambda \propto \rho^2$ for free-free emission or collisionally excited line radiation). Small density anisotropies amplified by a shock or shock precursor cool much more efficiently than the surrounding medium and are no longer in pressure equilibrium.

The size of the clumps is set approximately where the sound travel timescale is commensurate with the cooling timescale. Density variations across larger scales will not have time to be smoothed out before the cooling-driven instability sets in. Such clumps, if they exist, are unresolved in PPN. Similar clumps have, however,

been observed in fully fledged planetary nebulae, particularly the Helix Nebula. The size of the clumps in this object are of order 10^{15} cm with a mass of approximately $10^{-5} M_{\odot}$ (O'Dell & Handron, 1996).

5.3 Models of Clumping

5.3.1 Physical Assumptions

The simulations were produced with a version of the PROMETHEUS PPM hydrodynamics code optimized for stellar wind/CSM interactions (Mueller, Fryxell, & Arnett, 1991; Martin & Arnett, 1995). All calculations were performed in two dimensions on a spherical grid. A 300×140 grid was used for testing different cooling curves and CSM and wind conditions. The calculations for the most reasonable combination of parameters were repeated with 529×426 and 1000×806 grids.

The equation of state is the ideal gas law with ionization from electron collisions and the ambient radiation field and with recombination. Two sets of cooling curves were used. Both sets include free-free emission from Osterbrock (1989) and high temperature cooling from Kafatos (1973). The second set of curves has additional cooling for collisionally excited line radiation and fine structure recombination lines (Osterbrock, 1989) and rotational transitions of CO (Hollenbach & McKee, 1979). The collisionally excited line radiation and fine structure line curves are simple analytic functions which were designed to have the qualitatively correct functional form, and are normalized to the peak values of the curves in Osterbrock (1989). No attempt was made to reproduce the detailed physics of the cooling, merely to reproduce the correct order of magnitude values. The results are largely insensitive to the form of the cooling curve, so long as cooling is present, so we did not attempt to improve our curves. In some circumstances

there is a numerical instability in PPM codes related to cooling (Sutherland et al., 2003), however examination of our resolved simulations indicates we are not in this regime.

Since these simulations were motivated by the detection of NaCl in CRL 2688, we will briefly review the physical conditions in this object. Conditions in the circumstellar envelope have been determined from rotational line studies of CO. The inner “superwind” corresponds to a mass loss rate of $\dot{M} \sim 10^{-3} M_{\odot} \text{ yr}^{-1}$ (Young et al., 1992) and a velocity of $v \sim 60 - 200 \text{ km s}^{-1}$ (Herpin et al., 2002). The surrounding circumstellar material (CSM), produced by AGB mass loss, has $n(\text{H}_2) \sim 5 \times 10^5 \text{ cm}^{-3}$, $T \sim 50 \text{ K}$, and $v \sim 20 \text{ km s}^{-1}$ (Herpin et al., 2002). Shock zones form in the region where the fast wind interacts with the surrounding material. Emission from CO and H_2 has been seen in this shocked region, located $\sim 6-7''$ from the central star and distributed in a clover-leaf shaped distribution (Sahai et al., 1998a; Cox et al., 1997, 2000). In the optical and IR CRL 2688 shows a distinct bipolar morphology like many other PPN and PN (e.g. Sahai et al., 1998a).

We chose to use a somewhat more conservative (with regard to the clumping instability) set of conditions for the CSM and fast wind. For the CSM we used $n(\text{H}_2) \sim 1 \times 10^5 \text{ cm}^{-3}$ and $T_K \sim 50 \text{ K}$. The CSM was given an enhanced equatorial density that increases with polar angle as $\sin^{64}\theta$ and a maximum enhancement in the density of 50% (Martin & Arnett, 1995; Press et al., 1995). (This geometry was chosen since a large fraction of PN and CRL 2688 in particular are bipolar in shape, but the results turn out to be relatively insensitive to asymmetries at this level.) For the inner fast wind we used a mass loss history produced by the stellar evolution code TYCHO (Young, Mamajek, Arnett, & Liebert, 2001; Young et al., 2003). The median values produced by this mass loss history were

$\dot{M} \sim 2 \times 10^{-4} M_{\odot} \text{ yr}^{-1}$ and a differential velocity between the components of $v \sim 30 \text{ km s}^{-1}$. Because of the short timescales in question, these values were approximately constant over the duration of the simulation. Higher densities (or mass loss rates) in either component tend to promote clumping. The degree of clumping was relatively insensitive to the difference in velocity of the components up to $v \sim 80 \text{ km s}^{-1}$, though the radius of onset of clumping was larger since the expansion timescale was reduced relative to the cooling timescale. Above 80 km s^{-1} the temperatures in the shock exceeded 10^4 K , which is higher than the observed vibrational temperature of the shocked gas in CRL 2688. (From their measurements of H_2 , Cox et al. (1997) find $T_{\text{vib}} \sim 3000 \text{ K}$.) The inner boundary of the simulation was set at $5 \times 10^{16} \text{ cm}$.

A few further caveats must be kept in mind. First, the simulations are two dimensional. This means that collapse into clumps is constrained to two dimensions; in the third the material forms annuli around the axis of symmetry. In a real system the material can collapse in three dimensions, resulting in larger density enhancements, more efficient fingering (since material is being displaced along a small-cross section plume rather than an entire annulus), and a more complex morphology. (Fingering here refers to the common behavior of finger-like protrusions developing at an unstable interface.) Secondly, the wind and CSM are plasmas, so they can and probably do support magnetic fields, the effects of which are considerably more difficult to predict *a priori*. Third, the morphology of a real proto-planetary nebula is considerably more complex than the smoothly varying distribution examined here. The presence of molecular outflows, jets, multiple AGB wind components and large scale density perturbations will change the distribution and morphology of clumps. In fact, multiple molecular outflows have been observed in CRL 2688 (Cox et al., 2000).

5.3.2 Results

We find that for the conditions described in section 3.1, the highest density in the simulation increases at the beginning of the simulation as the shock establishes itself, then decreases for a time before reaching a minimum as cooling takes over from spherical divergence as the primary process controlling the density evolution. The density thereafter increases in the clumps until the shock front moves off the grid.

The maximum densities and the radii at which they are achieved emphasize the importance of grid resolution to this simulation. As discussed in §2, the physical size of the clumps should be quite small. The size of the clumps, and correspondingly their maximum density, is limited by the grid in the low and medium resolution simulations. The ratio of maximum densities achieved in two underresolved simulations scale as the square of the increase in radial resolution between the simulations. The onset of clumping occurs much earlier for higher resolution, as well. This scaling no longer holds between the medium and high resolution simulations. The maximum densities and radius of onset of clumping do not differ by more than 10% at any point, indicating that the medium resolution simulation is slightly under-resolved or barely resolved and the high resolution over-resolved.

In the medium resolution simulations, a maximum density of $n = 3.4 \times 10^6 \text{ cm}^{-3}$ occurs at $r \sim 1.5 \times 10^{17} \text{ cm}$, and clumping is already developing. The density drops to $n = 2.8 \times 10^6 \text{ cm}^{-3}$ at $r \sim 2.5 \times 10^{17} \text{ cm}$ and returns to near its peak value by $r \sim 3.5 \times 10^{17} \text{ cm}$ at the end of the simulation. In the high resolution simulation, a local maximum density of $n = 3.7 \times 10^6 \text{ cm}^{-3}$ is reached at $r \sim 1.5 \times 10^{17} \text{ cm}$. The following minimum of $n = 3.0 \times 10^6 \text{ cm}^{-3}$ occurs at $r \sim 2.6 \times 10^{17} \text{ cm}$ and density rises to $n = 3.9 \times 10^6 \text{ cm}^{-3}$ by the end of the

simulation, at which point it is still increasing.

In both cases the timescale for the full development of clumping is a few hundred years, which is approximately the timescale for the interaction of the fast wind with the CSM in CRL 2688 according to H_2 observations (Sahai et al., 1998a). If we define clumps as a plateau of locally maximum density in the simulation, the physical sizes at $r \sim 1.5 \times 10^{17}$ cm range around $\geq 0.5 \times 10^{15}$ cm, with masses of approximately $\geq 0.5 \times 10^{-5} M_{\odot}$. (The resolution of the grid at this radius is 1.8×10^{15} cm.) The density falls off to near the ambient over a similar distance. The clumps also have long “tails” at lower density due to the fingering of the instability. Figure 5.1 shows the fully developed clumping in the high resolution simulation. The white line shows the position of the shock.

In order to ensure the size of the clumps is not a numerical artifact, we ran simulations with 1% random gaussian density fluctuations or a sinusoidal 10% density perturbation with an angular frequency of $20/2\pi \text{ sr}^{-1}$. These perturbations should overwhelm roundoff error at cell boundaries as seeds for the instability and start fingering on much larger scales if the natural physical scale of the clumps is larger than the grid size. No difference is seen in clump sizes with and without the perturbations. To confirm that the clumping is driven by a thermal instability, we performed a control simulation with no cooling. Figure 5.2 compares simulations with and without cooling. Without cooling no instability develops, even at large radii. (The vortex at the bottom of the no cooling case is a result of an interaction between the boundary conditions and the equatorial density enhancement and does not appear in spherically symmetric simulations.) Both panels are on the same density scale. The inner radius of the onset of clumping is a more difficult problem. It can potentially be varied widely simply by assuming different geometries for the circumstellar medium and conditions in the

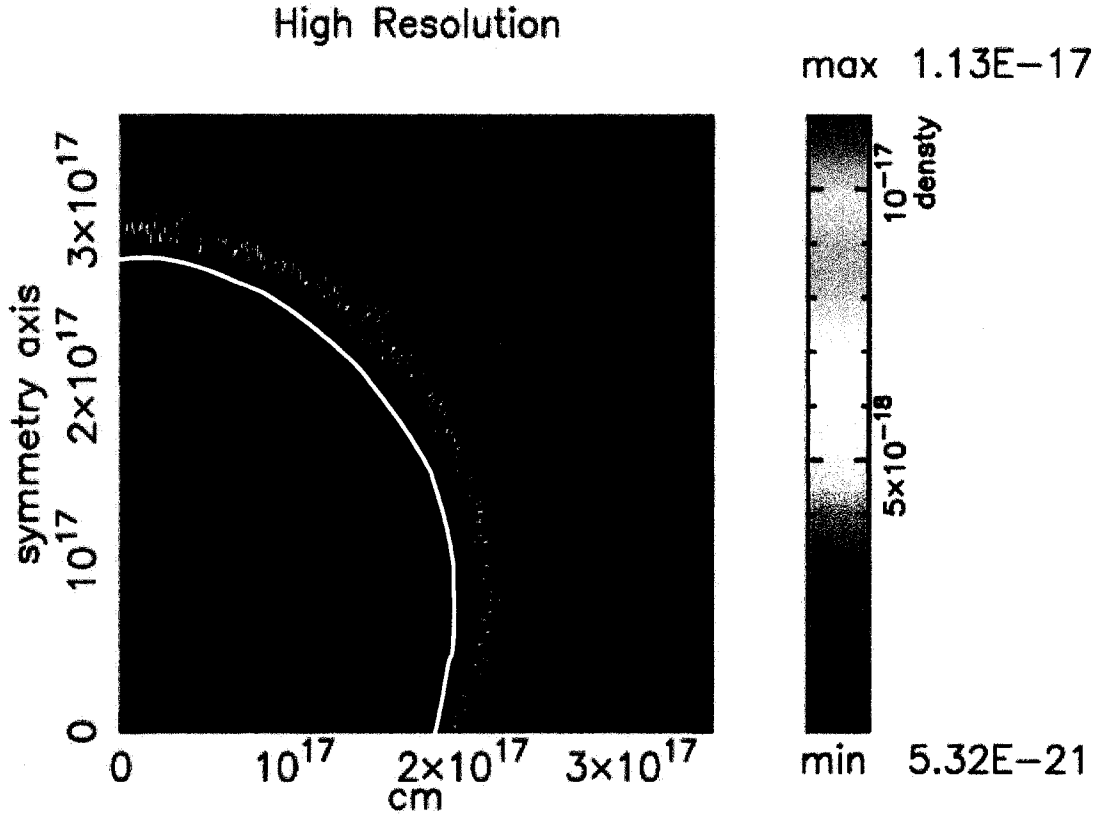


Figure 5.1: Density profile for fully developed clumping for the high resolution simulation. Densities are in g cm^{-3} . The shock is shown in white. The maximum number density achieved is $n = 3.9 \times 10^6 \text{ cm}^{-3}$. Clumping is driven by thermal instabilities seeded by a hydrodynamic precursor. The physical conditions assumed for the simulation are described in section 3.1. The small dark circle is the inner boundary. The low level, declining density enhancement just outside the inner boundary is the fast wind flowing out from the star.

CSM and fast wind at the beginning of the PPN phase. The clumps themselves, once formed, have a lifetime long compared to the simulations, and may well move out to significantly larger distances. At larger radii, even if the clumps are present, their covering factor will be sufficiently small that beam dilution from

a single dish will make them once again unobservable. We must be careful in interpreting the extent of the clumps from observations. Their true distribution may be larger. We have demonstrated that the clumping can happen, but other physics besides that of clump formation may determine the *observed* scale.

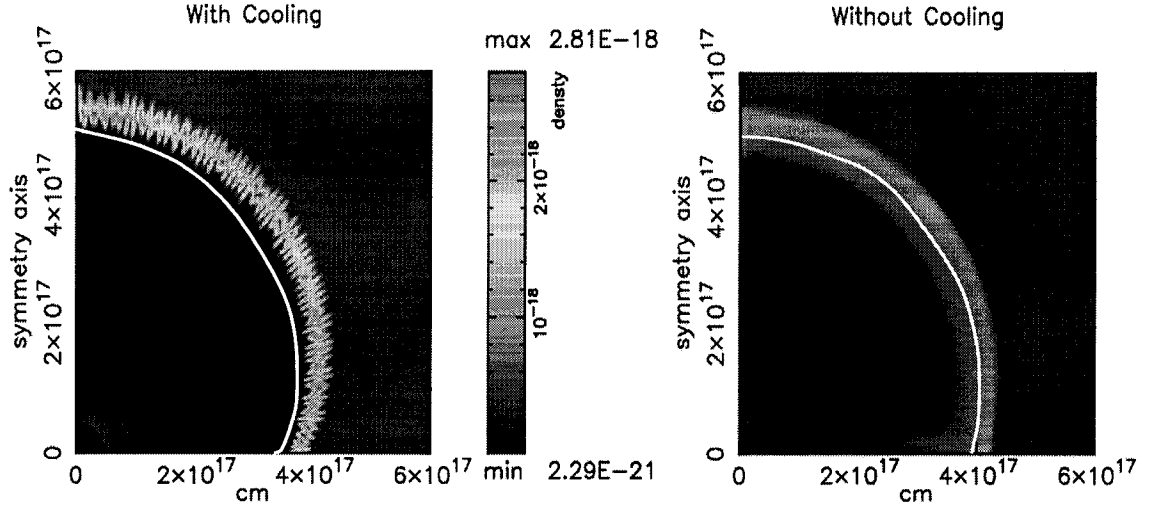


Figure 5.2: Comparison of density profiles at similar shock radii for cases with (left) and without (right) cooling. Without cooling the thermal instability does not develop, and the density profile remains smooth. (The plume at the bottom of the right hand panel is a result of interaction of the boundary conditions with the equatorial density enhancement. It does not appear in spherically symmetric simulations.) The position of the shock in each case is indicated by the white curve. The density enhancement in the case with cooling is caused by a thermal instability driven by a hydrodynamic precursor ahead of the shock. In the case without cooling the density enhancement is smaller and is only due to the shock jump conditions.

The densities reached in the high resolution simulations exceed the densities needed for excitation of the $J = 7 \rightarrow 6$ transition of NaCl ($n = 3.4 \times 10^6 \text{ cm}^{-3}$ at

50 K), but are a factor of several short of what is needed for higher transitions. This is not problematic, and perhaps even desirable, for two main reasons. First, the conditions in the CSM and fast wind are conservative. Higher mass loss rates translate to increased clumping. Second, the simulation is only in 2D, which only allows fragmentation and compression of the clumps along two axes. Were these annuli allowed to fragment in the third dimension the densities would be enhanced further.

The structure of the shock is also worthy of note. The main shock (characterized by a change in the sign of $\nabla \cdot \mathbf{V}$ from expansion to compression and a temperature of $T \sim \text{a few} \times 10^3$ K) is interior to the clumping. The main shock is preceded by a hydrodynamic precursor. The C abundance of the fast wind was set to a factor of 10^3 lower than that of the CSM to provide a tracer of the Lagrangian motion of the material. Figure 5.3 shows the C abundance for the low resolution simulation at the same timestep as the density plot. The C poor material has clearly moved ahead of the main shock and shows a fingering pattern identical to that seen in the density. Other mechanisms for the precursor are ruled out independently. The code does not contain the physics for a magnetic or cosmic ray precursor, and the temperatures in the shock are too low to produce a photoionization precursor. It is interesting to note that the measured radii of the NaCl and NaCN emission and the shock front as measured by H_2 are $\sim 10\text{--}12''$ and $\sim 6\text{--}7''$, respectively (Highberger et al., 2003; Sahai et al., 1998a; Cox et al., 1997). This difference seems to indicate that the high densities occur *outside* the strong shock, as we see in these simulations.

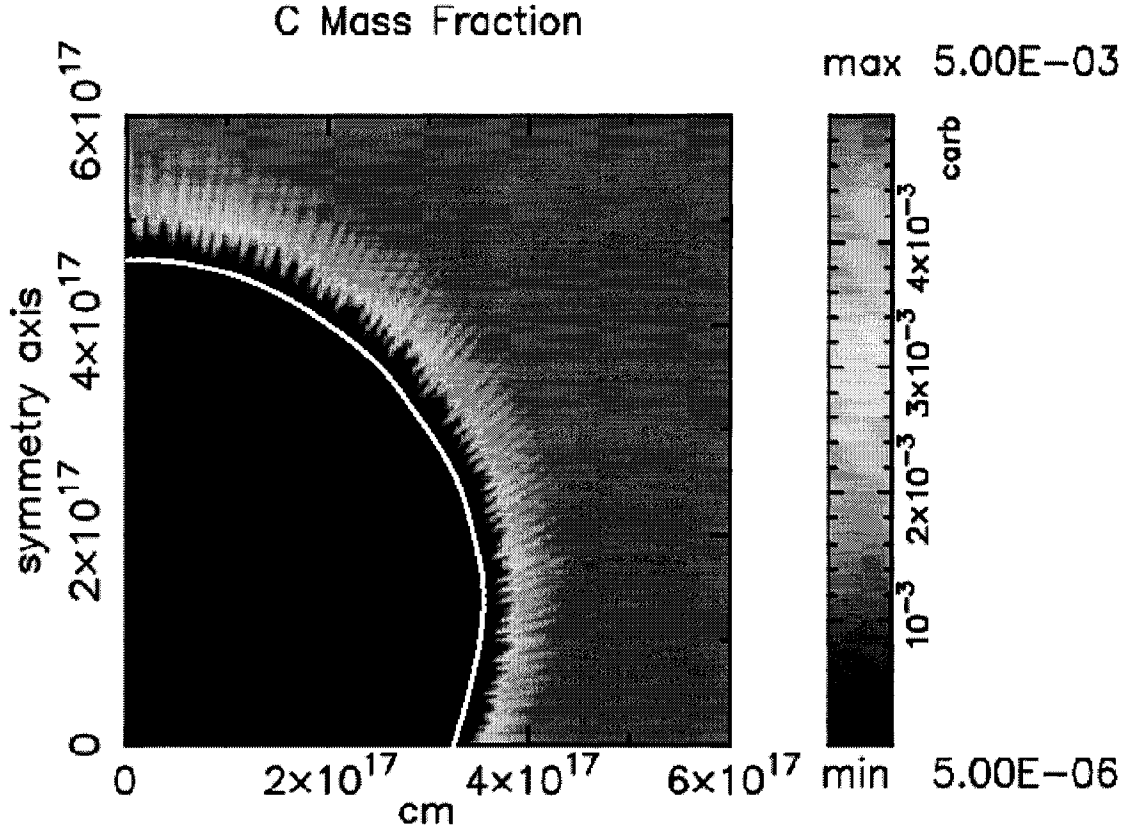


Figure 5.3: Carbon mass fraction of the material. The C abundance of the fast wind is set to 10^{-3} of the CSM to provide a Lagrangian tracer. The position of the shock is indicated in white. The changed C abundance ahead of the shock betrays the presence of a hydrodynamic precursor which is driving the thermal instability. The fingering in the C abundance closely matches that of the density profile.

5.4 Discussion

New molecular observations of NaCl and NaCN in the proto-planetary nebula CRL 2688 imply extreme densities in a shell at large radii from the central star. We investigate the behavior of a thermally unstable shock produced by a fast super-wind impacting CSM from previous stages of mass loss with a two dimensional

hydrodynamics code. When even simple cooling is included, the hydrodynamics initiates a thermal instability in a shock precursor which leads to the formation of high density clumps. These clumps can achieve the requisite densities at large radii from the star. The clumping mechanism is robust, occurring even for conservative estimates of PPN conditions. These results serve as a proof of concept for the importance of including clumping in models of post-AGB and PPN systems and underscore the necessity of modeling the hydrodynamics of such systems in multiple dimensions.

Observations in the optical/IR may offer insight into this model. The clump sizes we see in simulations are similar to those observed for cometary globules in the Helix Nebula (O'Dell & Handron, 1996). This does not necessarily imply that the clumps which we posit for PPN are the precursors of PN clumps. However, the composition and the cooling curves should be nearly the same for both cases. If the cometary globules are the product of a thermal/hydrodynamic instability, which is plausible but not certain (Huggins et al., 2002), then their characteristic size should be similar to what we predict for clumps in our simulations. We have recently demonstrated the feasibility of such observations from the ground. Figure 5.4 is an image of the planetary nebula IC 2149 taken with the ARIES near-IR camera on the 6.5m MMT using adaptive optics. The image is a false-color composite of three narrow band images at 2.088, 2.118, and 2.17 μm (blue, green, and red, respectively). The spatial resolution of the image is $\sim 0.08''$. At this resolution the clumps should be resolvable at distances of < 300 pc.

Ideally we would like to identify the structures in CRL 2688 associated with the molecular emission. The most likely scenario is that the sodium molecules are associated with material traced by vibrationally-excited H_2 , which exhibits a clumpy, clover-leaf-shaped distribution (Cox et al., 2000). The emission suggests

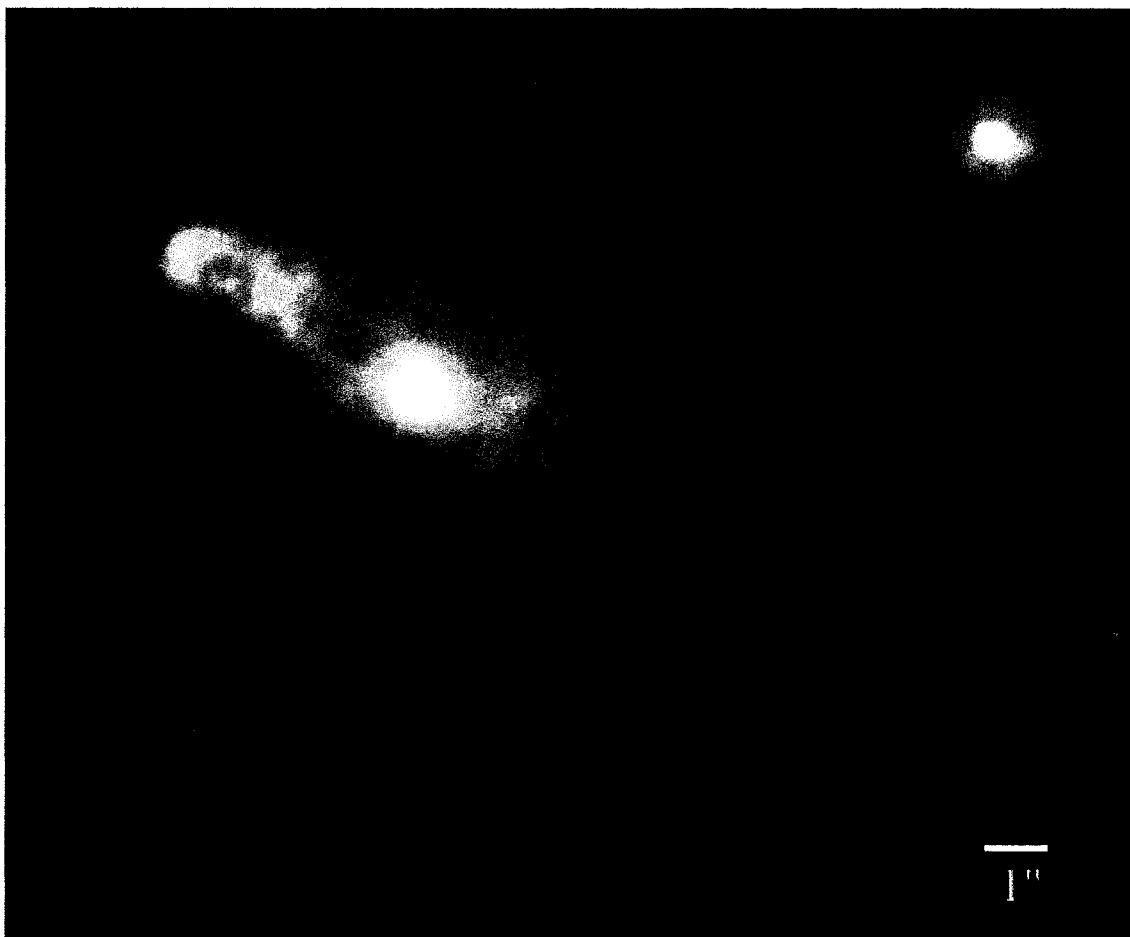


Figure 5.4: The planetary nebula IC 2149, imaged by the ARIES near-infrared imager and adaptive secondary on the 6.5m MMT. The image is a false color composite of three narrow band filters at 2.088, 2.118, and 2.17 μm , (blue, green, and red, respectively). The central star has been allowed to saturate in order to bring out details in the surrounding nebula, which is several thousand times fainter. The inset is a narrow band continuum image of the central bright region magnified by a factor of two. The contrast has been adjusted so that details in the inner dusty shell around the central star can be seen.

that this is shocked gas from a wind-wind interaction. It is from this region that we take our initial conditions. The inferred shock temperatures are consistent

with our model, and the geometries can be accommodated by assuming a more structured CSM and fast wind. Our models indicate that the clumping behavior is robust for the physical conditions associated with the shock. The simulations indicate that the Na molecule emission should be in a precursor to the shock. Just outside the H_2 is the most likely location for the NaCl and NaCN emission if the clumping mechanism is indeed responsible for creating the requisite conditions for excitation. This agrees very well with the observational evidence available for the location of the Na molecules. The measured radii of the NaCl and NaCN emission and the H_2 are $\sim 10\text{--}12''$ and $\sim 6\text{--}7''$, respectively (Highberger et al., 2003; Sahai et al., 1998a; Cox et al., 1997)

CHAPTER 6

CONCLUSION

In order to understand the ephemeral final stages of stellar lifetimes and predict the properties of large ensembles of stars and their impact on the history of galaxies, we require a description of stellar evolution which is based as much as possible upon physics, and not observational calibration of parameters, since in general we cannot guarantee that the calibrations apply in other situations. In spite of the computational difficulty of the problem, it is possible to make considerable progress toward this goal.

A systematic examination allows us to identify in general terms the areas of physics which are deficient. We find that the primary problem lies in the physics of compositional mixing in stellar interiors. Analytic descriptions of convection alone predict too little mixing in stars. (Mass loss is also not well understood. It plays a large role in the evolution of massive stars ($> 30 - 40M_{\odot}$), but is beyond the scope of the present discussion.)

Missing physics can be identified in multi-D numerical hydrodynamics or plasma dynamics experiments. By examining such simulations of stellar convection, we have identified an important mechanism for mixing in the radiative regions of stars. Having developed a physical theory to describe this behavior, we incorporate an approximation of the physics into the stellar evolution code TYCHO. We test the predictions of the code against a wide variety of observations and find good agreement in all cases. The agreement is based upon physical theories and achieved without resort to calibration of parameters against obser-

uations.

The obvious result of this work is the importance of including realistic hydrodynamic mixing. That mixing is a problem comes as no surprise. Numerous groups have identified this inadequacy in standard stellar models. This theory has the advantage of being physically based and tested with some rigor. It is therefore *predictive* to a greater extent than most treatments, and extensible to situations with few observational constraints. Some of the most interesting results arise when considering the intersection of the theory and observations in this context.

We first find an estimate of the predictive accuracy of a stellar evolution code with the most complete physics presently available in the field. The sun is probably the easiest star to model since it is minimally affected by mixing and mass loss, which are our greatest areas of uncertainty in stellar physics. We can therefore take our estimate for the amount variation we can introduce by our remaining free parameters as our minimum uncertainty in predicting the structure of a star of a given age with a given initial mass and composition. Most other cases are likely to be worse, being more sensitive to mixing and mass loss. From the solar models we find that our predictive accuracy is limited to of order 5-10% by (1) inadequacy in our description of convection, manifested by an uncertainty in the fictitious mixing length parameter, and (2) by uncertainties in abundances. If the nature of the convection is fixed by numerical simulations of full 3-D convection, the uncertainty from (1) is reduced to $< 1\%$, and we are limited by the abundance determinations. On the other hand, the good agreement of the neutrinos for all of our models indicate that the variation in surface observables between models is a surface effect of the convective envelope, and the interior structure is fairly well modeled. Of course, the sun has a radiative core, and this insensitivity will

not hold for more massive stars or lower mass ones with very deep convective envelopes.

The solar models also provide an example of a most insidious problem. Gravitational settling and differential diffusion of heavy elements clearly controls the position of the model tracks along the main sequence. Models with and without hydrodynamic mixing in the radiative regions are virtually identical, as long as they include diffusion. On the pre-MS, however, the path through the HR diagram is controlled by the hydrodynamic mixing. Diffusion has not had time to operate, and the presence of a transient convective core during partial CN burning makes the mixing important. The two tracks which both achieve a good fit at the solar age diverge significantly at other stages in the evolution. It is possible to find a good formal fit to the observations without including physics which may be very important during other stages of the star's life. Evolutionary tracks which converge at a single point are not necessarily unique. This is adequate for describing the state of an individual star, but presents a serious problem for characterizing the behavior of a star or population over time. It is vital to test a theory or code with the widest possible range of observations and terrestrial experiments in order to confirm that the included physics are complete.

The eclipsing binary sample reveals other subtleties. An increase in metallicity moves the tracks in the opposite sense of more complete mixing. It is possible to achieve an equally good fit with low metallicity and incomplete mixing or higher metallicity and more realistic physics. Making stellar abundance determinations by fitting evolutionary tracks is probably unreliable unless the physics in the code is very well tested independently. Many of the systems used as classical tests of stellar evolution, particularly the eclipsing binaries, do not have precise abundance determinations. The amount of variation that can be created in models by

varying the composition can potentially obscure a multitude of shortcomings in the included physics. It is essential that accurate spectroscopic abundance determinations be made for stars used as test cases of stellar evolution.

While we get very good results for most of our tests, the pre-MS binaries identify inadequacies in our current models. Taking the physics-based, as opposed to calibration approach, we can identify the cause of the problem. We must make an *ad hoc* adjustment to the mixing length in order to get large enough model radii. This points to an insufficiently physical description of convection and suggests what phenomena to examine for a solution. This insight can guide multidimensional numerical simulations of envelope convection in low surface gravity stars. Such simulations should (hopefully) allow us to characterize the physics well enough to make the models predict the observations.

Tests of the code against light element depletion and turnoff ages in young clusters, solar models, and eclipsing binaries over a wide range of masses, all using the same physics, get good results. Preliminary models of Cepheid variable stars do cross the instability strip determined from numerical simulations and observations. We do not calibrate parameters or compositions unless observational abundance determinations are available. We find a strong increase in the predictive accuracy throughout this range of conditions. Though this represents just a fraction of the problems in stellar astrophysics, it indicates that we have a physically sound approach which we can extend to other areas of stellar evolution.

It is useful to consider the impact of the improved physics described herein on several interesting areas of stellar evolution. In most cases we can anticipate the general trends, but not the quantitative changes without further work.

- Low mass main sequence stars: Evolutionary tracks generated by standard

models cannot be shifted by a constant amount in order to adjust for the effects of more complete physics. At all masses evolutionary tracks tend to be shifted redward by the inclusion of gravitational settling and mixing beyond convective zones. The minimum mass at which a convective core persists during the MS will be reduced. As a result, the minimum luminosity at which a “kink” appears in a turnoff will be reduced. Since the establishment of a convective core and the transition to CNO burning tends to significantly reduce stellar lifetimes, the age of isochrones near the minimum mass will also be reduced. Overall, for stars near or below the transition to convective cores, main sequence lifetimes will decrease by a small amount, and derived stellar masses will decrease.

- High mass main sequence stars: The degree of mixing caused by hydrodynamic processes increases with mass. For stars with well established convective cores, evolutionary tracks will be shifted to higher luminosity at a given mass and have a much greater redward extent. The increased core sizes provide more fuel to the core, extending stellar lifetimes. The result for turnoff ages relevant to OB associations is to increase the age substantially over standard models and reduce the turnoff mass. Overall, main sequence lifetimes will increase and derived stellar masses decrease.
- Evolved white dwarf progenitors: The red giant branch for stars which undergo the He flash should not change much, since the Schönberg-Chandrasekhar limit is determined by the composition and the physics of degenerate matter. The maximum mass of stars with cores small enough to undergo the flash, however, will decrease. Convective He burning cores will be larger by a small amount, leading to larger white dwarf sizes for a given progen-

itor mass. The minimum mass for a supernovae will also be affected, and will likely be around $8 M_{\odot}$. The most obvious difference in the evolved stars should be seen in the products of s-process nucleosynthesis. S-process elements are primarily produced during double shell burning, and their production and dredge-up are sensitive to mixing outside of convective regions.

- Evolved supernova progenitors: The final core masses, which determine the properties of the supernova explosion and nucleosynthetic yield, will be systematically larger than standard calculations predict. The final stages of burning also seed the inhomogeneities which determine the geometry of the explosion, and will have to be calculated in 3-D from realistic initial models. The results are also very dependent upon mass loss, which is incompletely addressed. In general, the divisions between SNII and SNIb/c and their subtypes, and between neutron star/black hole progenitors, will have to be revised.
- Very massive stars and starburst populations: Preliminary work suggests that stars of roughly $40 M_{\odot}$ or more have sufficiently large convective cores that they make very rapid excursions to the redward side of the HR diagram when their central hydrogen content has dropped below $\sim 20 - 30\%$. When the stars reach $\log T_{eff} \sim 3.8$ they undergo large eruptions driven by high radiative accelerations at the base of the envelope. These tracks are quite different from standard massive star models. Observationally, no starburst populations younger than several million years (as measured by standard models) are seen, nor any with stars more massive than 30 or $40 M_{\odot}$ (Rigby & Rieke, 2004). Red supergiants are also problematic. These early depar-

tures to the red, followed by self-obscuration in eruption-produced dust, may contribute to a solution to the problem.

I will conclude with an example which shows the dramatic effect that the improved physics in TYCHO has on late stellar evolution, and gives a taste of the many problems which are likely to be impacted by the new approach. Figure 6.1 shows abundance profiles for a $23 M_{\odot}$ star about to begin core Si burning. The size of the core in large part determines the behavior of the ensuing supernova and the nucleosynthetic yield of the explosion.

The case with more complete mixing physics (top) has a much larger oxygen core than the model with only standard physics ($\sim 8M_{\odot}$ vs. $\sim 4M_{\odot}$). (Part of this core growth is the result of a breathing-mode instability during core He burning, in which fresh fuel ingested into the burning region causes rapid growth in core size of approximately 50%. A final O core of $\sim 6M_{\odot}$ is more realistic. An improved treatment of compositional mixing in the nuclear burning region itself should reduce this effect. Also note that an incomplete set of weak nuclear reactions was used in these models, hence the presence of ^{56}Ni in the core. This does not affect the core sizes.) The remainder of the difference in core size is due to the improved treatment of mixing in radiative regions. This result implies that core sizes for a given mass of star may be tens of percent larger than predicted by standard models. Let us assume that a supernova progenitor has a core the same mass as standard models would predict for a star 30% larger. For a simple Salpeter IMF ($\frac{dN}{dM} \propto M^{-2.35}$), we find that these progenitors (and thus their input into the ISM) are roughly twice as common as we would assume from standard models. This change could have a significant impact on chemical evolution models for galaxies. The next phase of this project will involve calculating libraries of yields for complete IMFs and quantifying the disparity with earlier models.

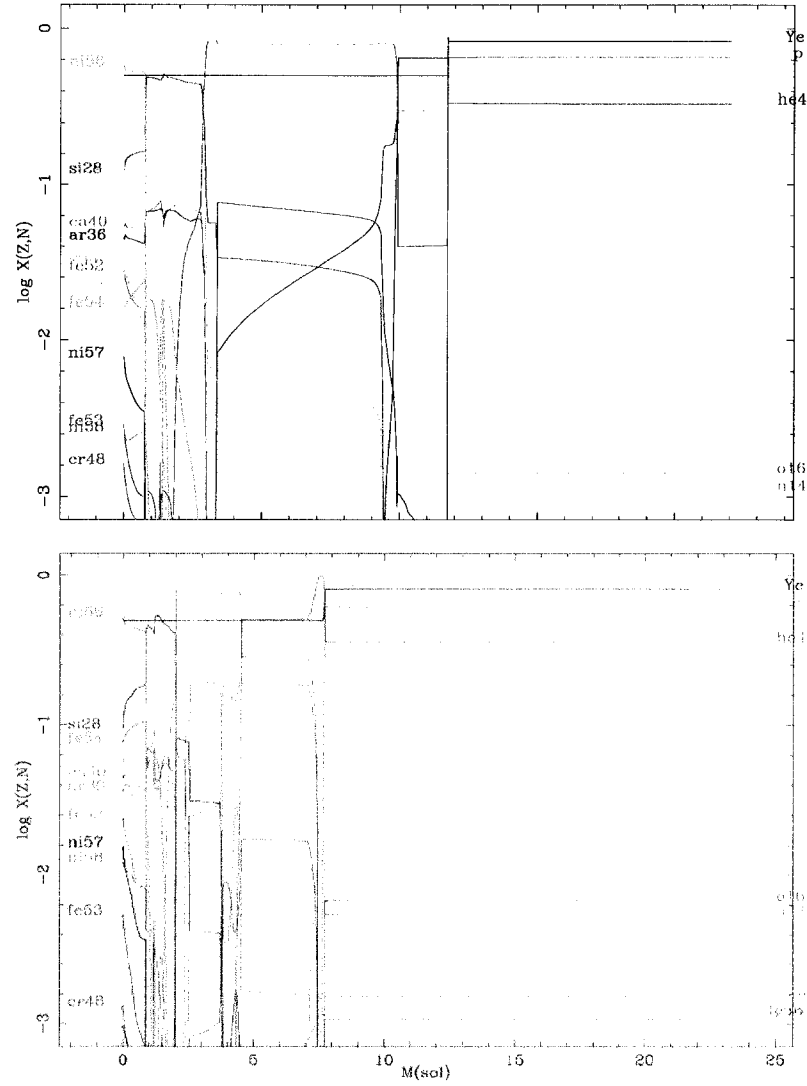


Figure 6.1: Abundance profiles for a $23 M_{\odot}$ star at the beginning of Si burning for models with realistic mixing physics (top) and without (bottom). Note the much larger size of the oxygen core in the case with mixing ($\sim 8M_{\odot}$ vs. $\sim 4M_{\odot}$). Some of this increase is attributable to a breathing-mode type instability during He core burning, but a large fraction of the difference in core size is a direct result of adding more complete mixing. (Note that an incomplete set of weak nuclear reactions was used in these models, hence the presence of ^{56}Ni in the core. This does not affect the core sizes.)

REFERENCES

- Alexander, D. R. & Ferguson, J. W. 1994, *ApJ*, 437, 879
- Anders, E. & Grevesse, N. 1989, *Geochim. Cosmochim. Acta* 53, 197
- Andersen, J., Clausen, J. V., & Magain, P. 1989, *A&A*, 211, 346
- Andersen, J., Nordström, B., & Clausen, J. V., 1990, *ApJL*, 363, 33
- Andersen, J. 1991, *A&A Rev.*, 3, 91
- Angulo, C., 1999, *Nuclear Phys. A* 656, 3
- Arnett, D. 1996, *Supernovae and Nucleosynthesis*, Princeton University Press.
- Asida, S.M., & Arnett, D. 2000 *ApJ*, 545, 435
- Asida, S., 1998, *ApJ*, 528, 896
- Asida, S. M. 2000, *ApJ*, 528, 896
- Bahcall, J. N. & Pinsonneault, M. H. 1998, private communication
- Basu, S., Pinsonneault, M. H., & Bahcall, J. N., 2000, *ApJ*, 529, 1084
- Bahcall, J. N., Pinsonneault, M. H., & Basu, S. 2001, *ApJ*, 555, 990
- Bahcall, J. N. & Pinsonneault, M. H. 2004, *Phys. Rev. Lett.*, 92, 121301
- Barrado y Navascués, D., Stauffer, J. R., & Patten, B. M. 1999, *ApJ*, 522, L53
- Bazàn, G., & Arnett, D. 1998, *ApJ*, 494, 316
- Blanco, V. M., Blanco, B. M., & McCarthy, M. F. 1980, *ApJ*, 242, 938

- Blöcker, T. 1995, *A&A*, 297, 727
- Bodenheimer, P., 1965 *ApJ*, 142, 451
- Boesgaard, A. M. & King, J. R. 2002, *ApJ*, 565, 587
- Boesgaard, A. M. & Friel, E. D. 1990, *ApJ*, 351, 467
- Boothroyd, A. I. & Sackmann, I.-J. 2003, *ApJ*, 583, 1004
- Bressan, A., Fagotto, F., Bertelli, G., & Chiosi, C., 1993, *A&AS*, 100, 647
- Brummell, N. H., Clune, T. L., & Toomre, J. 2002, *ApJ*, 570, 825
- Busso, M., Gallino, R., & Wasserburg, G. J. 1999, *ARA&A*, 37, 239
- Cameron, A. G. W. & Fowler, W. A. 1971, *ApJ*, 164, 111
- Canuto, V. M. & Mazzitelli, I., 1991, *ApJ*, 370, 295
- Canuto, V. M., & Mazzitelli, I., 1991, *ApJ*, 389, 724
- Canuto, V. M. 2000, *ApJ*, 571, L79
- Canuto, V. M. 2002, *A&A*, 384, 1119
- Caughlan, G., & Fowler, W. A., 1988, *Atomic and Nuclear Data Tables*, 40, 283
- Chaboyer, B. Demarque, P., & Pinsonneault, M. H. 1995, *ApJ*, 441, 865
- Chandrasekhar, S. 1961, *Hydrodynamic and Hydromagnetic Instability*, Oxford University Press, London
- Charbonnel, C., & Talon, S., 1999, *A&A*, 351, 635
- Christensen-Dalsgaard, J. 2000, private communication

- Christensen-Dalsgaard, J. 2002, *Rev Mod Phys*, 74, 1073
- Claret, A., 1995, *A&AS*, 109, 441
- Claret, A., 1997, *A&A*, 327, 11
- Claret, A., 1997, *A&AS*, 125, 439
- Claret, A., 1998, *A&A*, 330, 533
- Claret, A., 1999, *A&A*, 350, 56
- Claret, A., & Giménez, 1991, *A&A*, 249, 319
- Claret, A., & Giménez, 1993, *A&A*, 277, 487
- Claret, A., & Giménez, 1995, *A&AS*, 114, 549
- Claret, A., & Giménez, 1998, *A&AS*, 133, 123
- Claret, A., Giménez, & Martin, E. L., 1995, *A&A*, 302, 741
- Clayton, D. D. 1983, *Principles of Stellar Evolution and Nucleosynthesis*, University of Chicago Press, Chicago
- Cowling, T. G., 1941, *MNRAS*, 101, 367
- Cox, J. P., 1980, *Theory of Stellar Pulsations*, Princeton University Press, Princeton NJ
- Cox, P., Maillard, J.-P., Huggins, P. J., Forveille, T., Simons, D., Guilloteau, S., Rigaut, F., Bachiller, R., & Omont, A. 1997, *A&A*, 321, 907
- Cox, P., Lucas, R., Huggins, P. J., Forveille, T., Bachiller, R., Guilloteau, S., Maillard, J.-P., & Omont, A. 2000, *A&A*, 353, L25

- Däppen, W., & Nayfonov, A., 2000, *ApJS*, 127, 287
- Davidson, S. J., Nazir, K., et al., 2000, *J. Quant. Spec. Radiat. Transf.*, 65, 151
- de Bruijne, J. H. J., Hoogerwerf, R., & de Zeeuw, P. T. 2001, *A&A*, 367, 111
- de Jager, C., Nieuwenhuijzen, H., & van der Hucht, K. A. 1988, *A&A*, 173, 293
- Deliyannis, C. P., Boesgaard, A. M., Stephens, A., King, J. R., & Vogt, S. S. 1998, *ApJ*, 498, L147
- de Zeeuw, T., Hoogerwerf, R., de Bruijne, J. H. J., Brown, A. G. a., & Blaauw, A., 1999, *AJ*, 117, 354
- Dimotakis, P. E. 2001, *APS*, DPP LM2.004
- Dominguez, I., Chieffi, A., Limongi, M., & Straniero, O., 1999, *ApJ*, 524, 226
- Dupree, A. K. & Reimers, D. 1987, in *Exploring the Universe in the Ultraviolet with the IUE Satellite*, eds. Y. Kondo et al. (Dordrecht: Reidel), p.231
- Elliott, J. R., Miesch, M. S., & Toomre, J., 2000, *ApJ*, 533, 546
- Feigelson, E. D., & Montmerle, T., 1999, *ARA&A*, 37, 363
- Feuchtinger, M., Buchler, J. R., & Kolláth, Z. 200, *ApJ*, 544, 1056
- Fong, D., Meixner, M., & Shah, R. Y. 2003, *ApJ*, 582, L39
- Freytag, B., Ludwig, H.-G., & Steffan, M., 1996, —*aap*, 313, 497
- García López, R. J. & Spruit, H. C. 1991, *ApJ*, 377, 268
- Gimenez, A., Clausen, J. V., & Jensen, K. S., 1986, *A&A*, 159, 157
- Golreich, P., N. Murray, & Kumar, P., 1994, *ApJ*, 424, 466

- Grevesse, N. & Sauval, A. J., 1998, *Space Science Reviews*, 85, 161
- Guélin, M., Lucas, R., & Neri, R. 1997 in *CO: Twenty-five Years of Millimeter Wave Spectroscopy* eds. W. B. Latter et al. (Dordrecht: Kluwer), 359
- Guinan, E. F., Ribas, I., Fitzpatrick, E. L., Giménez, Jordi, C., McCook, G. P., & Popper, D. M., 2000, *ApJ*, 544, 404
- Hansen, C. J., & Kawaler, S. D., 1994, *Stellar Interiors*, Springer-Verlag
- Henry, L. G., Wilets, L., Böhm, K. H., LeLevier, Robert, & Levee, R. D., 1959, *ApJ*, 129, 628
- Herpin, F., Goicoechea, J. R., Pardo, J. R., & Cernicharo, J. 2002, *ApJ*, 577, 961
- Highberger, J. L., Thomson, K. J., Young, P. A., Arnett, D., & Ziurys, L. M. 2003, *ApJ*, 593, 393
- Hillenbrand, L. A. & White, R. J. 2004, *ApJ*, 604, 741
- Hollenbach, D. & McKee, C. F. 1979, *ApJS*, 41, 555
- Huggins, P. J., Forveille, T., Bachiller, R., Cox, P., Ageorges, N., & Walsh, J. R. 2002, *ApJ*, 573, L55
- Hurlburt, N. E., Toomre, J., & Massaguer, J. M., *ApJ*, 311, 563
- Iglesias, C., Wilson, B. G., et al., 1995 *ApJ*, 445, 855
- Iglesias, C. & Rogers, F. J. 1996, *ApJ*, 464, 943
- Kafatos, M. 1973, *ApJ*, 182, 433
- Kippenhahn, R. & Weigert, A. 1990, *Stellar Structure and Evolution*, Springer-Verlag

- Kudritzki, R. P., Pauldrach, A., Puls, J., Abbott, & D. C. 1989 A&A, 219, 205
- Kumar, P., & Quataert, E. J., 1997, ApJ, 475, L143
- Kurucz, R. L., 1991, in *Stellar Atmospheres: Beyond Classical Models*, NATO ASI Series C, vol. 341
- Kwok, S. 2000 in *The Origin and Evolution of Planetary Nebulae* (Cambridge: Cambridge University Press)
- Lamers, H. J. G. L. M. & Nugis, T. 2003 A&A, 395L, 1
- Landau, L. D. & Lifshitz, E. M. 1959, *Fluid Mechanics*, Pergamon Press, London
- Latennet, E. & Valls-Gabaud, D. 2002, A&A, 396, 551
- Lastennet, E., Lejeune, T., Westera, P., & Buser, R. 1999, A&A, 341, 857
- Latham, D. W., Nordström, B., Andersen, J., Torres, G., Stefanik, R. P., Thaller, M., & Bester, M. J. 1996, A&A, 314, 864
- Levi-Civita, T., 1937, Am. J. Math., 59, 225
- Lewin, W. H. G., van Paradijs, J., & van den Heuvel, P. J. 1995, *X-Ray Binaries*, Cambridge University Press, p.469
- Lodders, K., 2003, ApJ, 591, 1220
- Lyngå, G., 1987, *Catalogue of Open Cluster Data*, 5th. ed., Lund Observatory
- Maeder, A., 1975, A&A, 40, 303
- Maeder, A. & Meynet, G. 1989, A&A, 84, L89
- Mamajek, E. E., Lawson, W. A., & Feigelson, E. D., 1999, ApJ, 516, L77

- Mamajek, E. E., Lawson, W. A., & Feigelson, E. D., 2000, *ApJ*, 544, 356
- Mamajek, E. E., Lawson, W. A., & Feigelson, E. D. 2000, *AJ*, 112, 276
- Mamajek, E. E. 2002, private communication
- Martin, E. L., & Rebolo, R., 1993, *A&A*, 274, 274
- Martin, C. L. & Arnett, D. 1995, *ApJ*, 447, 378
- Meakin, C. 2004, private communication
- Melnick, A. M., & Efremov, Yu. N., 1995, *Proc. Astron. Zhurnal*, 21, 13
- Meynet, G. & Maeder, A., 2000, *A&A*, 361, 101
- Michaud, G., Richard, O., Richer, J., & Vandenberg, D. A. 2004, *ApJ*, 606, 452
- Mostovych, A. N., Chan, L. Y., et al., 1995, *Phys. Rev. Lett.*, 75, 1530
- Mueller, E., Fryxell, B., & Arnett, D. 1991, *A&A*, 251, 505
- Norberg, P., & Maeder, A., 2000, *A&A*, 359, 1025
- O'Dell, C. R. & Handron, K. D. 1996, *AJ*, 111, 1630
- Osterbrock, D. E. 1989 *Astrophysics of Gaseous Nebulae and Active Galactic Nuclei* (Sausalito: University Science Books), 53ff.
- Pachoulakis, I., Pfeiffer, R. J., Koch, R. H., & Strickland, D. J., 1996, *The Observatory*, 116, 89
- Perry, T. S., Davidson, S. J., et al., 1991, *Phys. Rev. Lett.*, 67, 3784
- Perry, T. S., Springer, P. T., et al., 1996, *Phys. Rev. E*, 54, 5617

- Petrova, A. V., 1995, *AZh*, 72, 937
- Petrova, A. V. & Orlov, V. V., 1999, *AJ*, 117, 587
- Piau, L. & Turck-Chièze, S. 2002, *ApJ*, 566, 419
- Pinsonneault, M. H., Steigman, G., Walker, T. P., & Narayanan, V. K. 2002, *ApJ*, 574, 398
- Pols, O. R., Tout, C. A., Eggleton, P. P., & Han, Z., 1997, *MNRAS*, 274, 964
- Pols, O. R., Tout, C. A., Schröder, K-P., Eggleton, P. P., & Manners, J., 1997, *MNRAS*, 289, 869
- Pols, O. R., Schröder, K-P., Hurley, J. R., Tout, C. A., & Eggleton, P. P., & Han, Z. 1998, *MNRAS*, 298, 525
- Popper, D. M., 1987, *AJ*, 93, 672
- Porter, D. H., & Woodward, P. R., 1994, *ApJS*, 93, 309
- Porter, D. H., & Woodward, P. R., 2000, *ApJS*, 127, 159
- Porter, D., Woodward, P., Toomre, J., & Brummel, N. H. 2001, www.lcse.umn.edu/MOVIES
- Press, W. H., Teukolsky, S. A., Vetterling, W. T., & Flannery, B. P., 1992, *Numerical Recipes in FORTRAN*, Second Edition, University Press: Cambridge
- Press, W. H., Teukolsky, S. A., Vetterling, W. T., & Flannery, B. P. 1995 *Numerical Recipes in C* (New York: Cambridge University Press), 28ff
- Quataert, E. J., Kumar, P., & On, Chi, 1996, *ApJ*, 463, 284

- Randich, S., Pallavicini, R., Meola, G., Stauffer, J. R., & Balachandran, S. C. 2001, *A&A*, 372, 862
- Rauscher, T., & Thielemann, K.-F., 2000, *Atomic Data Nuclear Data Tables*, 75, 1
- Reif, F. 1965, *Fundamentals of Statistical and Thermal Physics*, McGraw-Hill Book Co., N.Y.
- Remington, B. A., Arnett, D., Drake, R. P., & Takabe, H. 1999, *Science*, 284, 1488
- Ribas, I., Jordi, C., Torra, J., & Giménez, Á., 2000, *MNRAS*, 313, 99
- Rigby, J. R. & Rieke, G. H. 2004, *ApJ*, 606, 237
- Robinson, F. J., Demarque, P., Li, L. H., Sofia, S., Kim, Y.-C., Chan, K. L., & Guenther, D. B. 2004, *MNRAS*, 347, 1208
- Rogers, F. J., & Iglesias, C. A., 1992, *ApJS*, 79, 507
- Rosenthal, C. S., Christensen-Dalsgaard, J., Nordlund, A., Stein, R. F., & Trampedach, R., 1999, *A&A*, 351, 689
- Ruprecht, J., Balazs, B., & White, R. E., 1982, *Bull. Int. Centre Donnees Stellaires*, 22, 132
- Ruprecht, J., Balazs, B., & White, R. E., 1983, *Soviet Astronomy*, 27, 358
- Sahai, R., Hines, D. C., Kastner, J. H., Weintraub, D. A., Trauger, J. T., Rieke, M. J., Thompson, R. I., & Schneider, G. 1998a, *ApJ*, 492, L163
- Sahai, R. et al. 1998b, *ApJ*, 493, 301
- Saslaw, W. C. & Schwarzschild, M., 1965, *ApJ*, 142, 1468
- Schaller, G., Schaerer, D., Meynet, G., & Maeder, A., 1992, *A&AS*, 96, 269

- Schatzman, E., 1999, *Ap&SS*, 265, 97
- Schröder, K-P., Pols, O. R., & Eggleton, P. P., 1997, *MNRAS*, 285, 696
- Schwarzschild, M., 1957, *Structure and Evolution of the Stars*, Princeton University Press, Princeton, New Jersey, p. 146
- Shaviv, G. & Salpeter, E. E., 1973, *ApJ*, 184, 191
- Soderblom, D. R., Jones, B. F., Balachandran, S., Stauffer, J. R., Duncan, D. K., Fedele, S. B., & Hudon, J. D. 1993, *ApJ*, 106, 1059
- Spiegel, E. 1972, *ARA&A*, 10, 261
- Spitzer, L., 1962, *Physics of Fully Ionized Gases*, Interscience Publishers, NY
- Springer, P. T., Fields, D. J., et al., 1992, *Phys. Rev. Lett.*, 69, 3735
- Stassun, K. G. Stassun, Mathieu, R. D., Vaz, L. P. R. , Stroud, N., & Vrba, F. J. 2004, *ApJS*, 151, 357
- Stauffer, J. R., Schultz, G., & Kirkpatrick, J. D. 1998, *ApJ*, 499, L199
- Stauffer, J. R., Barrado y Navascués, D., Bouvier, J., Morrison, H. L., Harding, P., Luhman, K. L., Stanke, T., McCaughrean, M., Terndrup, D. M., Allen, L., & Assouad, P. 1999, *ApJ*, 527, 219
- Stickland, D. J., Koch, R. H., & Pfeiffer, R. J., 1992, *Obs.*, 112, 277
- Stickland, D. J., Lloyd, C., Corcoran, M. F., 1994, *Obs.*, 114, 284
- Sutherland, R. S., Bisset, D. K., & Bicknell, G. V. 2003, *ApJS*, 147, 187
- Talon, S., Kumar, P., & Zahn, J-P., 2002, *ApJ*, 574, L175

- Tassoul, J.-L. 2000, *Stellar Rotation*, Cambridge University Press, NY
- Thielemann, F.-K., Arnould, M., & Truran, J. W., 1988, in *Advances in Nuclear Astrophysics*, eds. E. Vangioni-Flam, et al, Editions Frontiers: Gif sur Yvette, and private communication from FKT
- Thorburn, J. A., Hobbs, L. M., Deliyannis, C. P., & Pinsonneault, M. H. 1993, *ApJ*, 415, 150
- Thoul, A. A., Bahcall, J. N., & Loeb, A. 1994, *ApJ*, 421, 828
- Timmes, F. & Arnett, D., 1999, *ApJS*, 125, 277
- Timmes, F. X. & Swesty, F. D. 2000, *ApJS*, 126, 501
- Voges, W., et al., 1999, *A&A*, 349, 389
- Voges, W., et al., 2000, *ROSAT All-Sky Survey Faint Source Catalog (RASS-FSC)*, Max-Planck-Institut für Extraterrestrische Physik, Garching
- Wallerstein, G. 1973, *ARA&A*, 11, 115
- Wallerstein, G. & Knapp, G. R. 1998, *ARA&A*, 36, 369
- Wasaburo, U., Kiguchi, M., & Kitamura, M. 1994, *PASJ*, 46, 613
- Weinberg, S., 1972, *Gravitation and Cosmology*, John Wiley & Sons, New York
- Wegner, G., Reid, I. N., & McMahan, R. K. Jr. 1991, *ApJ*, 376, 186
- Will, C. M., 1998, *The Confrontation between General Relativity and Experiment: A 1998 Update*; see also www.livingreviews.org/Articles/ for an upcoming review
- Young, P. A., Mamajek, E. E., Arnett, D., & Liebert, J. 2001, *ApJ*, 556, 230

Young, P. A., Knierman, K. A., Rigby, J. R., & Arnett, D. 2003, *ApJ*, 595, 1114

Young, K., Serabyn, G., Phillips, T. G., Knapp, G. R., Guesten, R., & Schulz, A.
1992, *ApJ*, 385, 265